

AD-A154 793

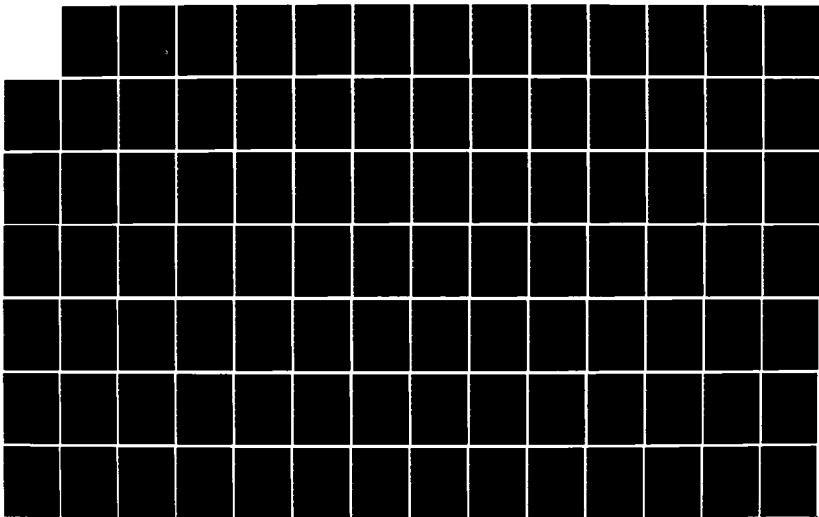
CALIBRATION AND USE OF CLUTTER DATA FOR SIMULATION(U)
WESTERN KENTUCKY UNIV BOWLING GREEN H S LONGHIRE 1985
N00014-84-C-2034

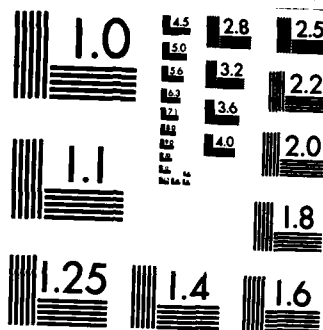
1/3

UNCLASSIFIED

F/G 17/5

NL





MICROCOPY RESOLUTION TEST CHART
NATIONAL BUREAU OF STANDARDS-1963-A

(2)

AD-A154 793

A Final Technical Report on
Calibration and Use of Clutter Data for Simulation
Contract with Naval Research Laboratory
Washington, D.C. 20375
Contract No. ~~N0014-84-C-2034~~
N00014-84-C-2034

Contractor
Western Kentucky University
Office of Sponsored Programs
Bowling Green, Kentucky 42101

Project Director
Dr. Martin S. Longmire
Department of Physics and Astronomy
Western Kentucky University
Bowling Green, KY 42101

Copies to: NRL 6550
NRL 6520
NRL 6502
NRL 6509
NRL 2415
NRL 2627
DTIC
ONR, Columbus, Ohio

DTIC
ELECTE
JUN 5 1985
A

Required forms for project close-out will be filed
with the Final Financial Report.

This document has been approved
for public release and sale; its
distribution is unlimited.

DTIC FILE COPY

85 04 30 078

A154 793

ADMINISTRATIVE OVERVIEW

This report is in three parts corresponding approximately to items of the contractual work statement.

→ ^(of this report) Part 1 describes calibration of the radiometer for the Background Measurements and Analysis Program (BMAP).

Part 2 ^(c) is an article with results bearing on two-dimensional signal processing. (It was published in ~~the 15 February 1985 issue of~~ Applied Optics ^{15 Feb 1985}.)

Part 3 consists of vignettes and supplemental text for two BMAP reviews and an Optical Sciences Division colloquium. → (top 2)



Accession For	
NTIS GRA&I	<input checked="" type="checkbox"/>
DTIC TAB	<input type="checkbox"/>
Unannounced	<input type="checkbox"/>
Justification	<i>Little on file</i>
By	
Distribution/	
Availability Codes	
Dist	Avail and/or Special
A-1	

PART 1
CALIBRATION OF BMAP RADIOMETER

CONTENTS

SECTION	TITLE	PAGE
1.1	PURPOSE AND SCOPE	2
1.2	APPARATUS	3
1.3	RESULTS, DISCUSSION, CONCLUSIONS, RECOMMENDATIONS	6
	.1 Attempted Calibration at Montauk Point	6
	.2 Survey of Radiometric Calibration	8
	.3 Selection of Blackbody Calibration Technique	13
	.4 BMAP Calibration Equation	13
	.5 Calibration Procedure	18
	.6 Laboratory Measurements	20
	.7 Field Measurements	22
	.8 Radiometric Calibrations Derived and Evaluated	23
	.9 Interpretation of Measured Radiances	25
1.4	REFERENCES	27
1.5	FIGURES	29
1.6	TABLES	53

1.1 PURPOSE AND SCOPE

(cont A p B)

→ The purpose of the Background Measurements and Analysis Program (BMAP) is to collect natural infrared background data for use in simulating the performance of Infrared Search and Tracks sets (IRSTs). Usually the objects sought by an IRST are effectively point sources; that is, their images are unresolved (no larger than a detector element). Thus, the point response of the BMAP sensor and electronics must be well characterized for the intended data use. The response to a bar source must also be determined in order to correct the data for a certain instrumental artifact described in section 1.2. And finally, the BMAP instruments should ^{also} be radiometrically calibrated so that simulated signals added to the background data can be related, at least approximately, to radiances of targets, as discussed briefly in references 1 and 2. *A*

The point- and bar-source calibrations guarantee that the data truly represent the spatial properties of the background. These calibrations are, therefore, more important than the radiometric calibration. Radiometrically uncalibrated data of good spatial fidelity can be used very effectively for comparative studies of signal processing options, as references 1 and 2 demonstrate. Contrariwise, radiometrically calibrated data of poor spatial fidelity may lead to wrong conclusions if used for simulations. Nonetheless, this report is concerned mainly with radiometric calibration because, overall, it is the most difficult of the three calibrations to implement, perform accurately and interpret. Both the point- and bar-source calibrations are easy to implement and perform accurately. The point-source results hardly require interpretation, although the apparatus may have to be adjusted to obtain the proper response. The bar-source results are hard to interpret and use for correcting the data, but R. A. Steinberg has solved the problem and reduced the procedure to routine.³ For these reasons, the point- and bar-source calibrations are mentioned in this report only to give a complete picture of the

calibration procedure. The discussion of calibration is preceded by a description of the apparatus, which gives information needed for understanding the calibration and using the background data.

1.2 APPARATUS

The functional parts of the apparatus are two optical sensors, their analog electronics, and a data acquisition system. This report is concerned mainly with the optical sensors and analog electronics, which make up the radiometer. Properties of the apparatus that affect calibration and use of the background data are given in Table 1 and Figures 1-9.

Figures 1 and 2 display the main parts of the optical sensors and convey an idea of the radiometer's size. The analog electronics are in the housing with the optical sensors. In essence, both telescopes are permanently focused on infinity; the longwave (LW) focus can be adjusted slightly to correct thermal defocusing, but the midwave (MW) optics are thermally compensated and have no adjustment. The photosensitive widths and heights of the detector arrays are shown larger than their actual scaled sizes in Figures 1 and 2 in order to make them visible. Figure 3 gives the sizes and layouts of the detectors to scale. The telescopes' blur circles (point-source images) are about $(1/3)$ milliradian in diameter, nearly matched to the widths of the detector elements. The scan mirror oscillates about its vertical axis sweeping images of the scene across the detectors. Typical point-source outputs are shown in Figure 4. The scan period is 0.5 seconds, and data are collected during a single subinterval of each period, so that the time between data frames is 0.5 seconds.

The scan mirror is driven by a triangular wave. The periods of the wave and mirror are identical; mirror displacement is directly proportional to wave strength. Consequently, increasing the wave amplitude increases mirror amplitude and scan rate. At present the mirror turns approximately ± 3 ($13/16$) degrees about its vertical axis sweeping the line of sight

left and right through a total azimuthal field of view of $7(5/8)$ degrees, twice the mirror amplitude. The spatial extent of the data interval is 2.8125 degrees, determined by a shaft encoder; the temporal extent is 100 milliseconds, determined independently as an electronic subdivision of the driving wave period. The scan rate must, therefore, be $\geq 28.125^\circ/\text{s}$ to keep the spatial extent of the data interval within its temporal bounds.

Figure 5 represents the radiometer's internal sources of reference radiation for one detector array; the arrangement for the other is the same. Cold and hot references are provided by motor-driven mirrors rotated through the field of view. The cold reference mirror reflects the detector's own radiation back to it. The hot reference mirror reflects radiation from an internal blackbody onto the detector. The cold reference mirror completely fills the field of view for about 2 milliseconds to allow time for electronic restoration of the output level. The hot reference mirror is shaped so that it completely fills the field of view only long enough for the detector to respond fully to the internal blackbody's radiation. The cold reference mirror passes very close to the detector, the hot reference mirror passes farther from it. With the cold reference mirror in place, the detector receives hardly any radiation except that emitted by itself and the mirror. With the hot reference mirror in place, the detector receives radiation from the internal blackbody and the radiometer's interior. When the detector views the scan mirror through the telescope, it receives radiation from the scene and stray radiation from outside and inside the radiometer.

Figure 6 presents block diagrams of the analog electronics. Each detector of an array has its own electronics like those shown. The amplifiers and cold clamps are the same for the two arrays, but the longwave detectors must be biased, requiring ac coupling to eliminate the bias voltages from the outputs. This potentially complicates the radiometric calibration, but since the time constants of the ac active filters are about 30 times the data interval, the effect

of ac coupling can be ignored with good accuracy. The analog outputs go to the data acquisition system where they are sampled, digitized, and recorded on magnetic tape.

The output format is displayed in Figure 7. At the start of the data interval, the cold reference mirror rotates into place, and the electronic cold clamp restores the output level to ground within less than 2.5% of the full scale value, 10 volts or 4096 arbitrary units. The output then rises, peaks and falls as the hot reference mirror passes through and out of the field of view. Afterward the detector has an unobstructed view of the scene for the remainder of the data interval.

Sampling of the analog outputs is controlled by the scan mirror through its shaft encoder which takes 2^{16} samples in 360° , i.e., 512 samples in each 2.8125° data interval. The last two samples may be in error, however, so each data frame contains 510 usable values. The cold reference occupies the first 10 values; the hot reference mirror is completely out of the field of view at the 140th sample; the remaining 370 samples are usable scene data covering 2.03° or 35.5 milliradians of azimuth.

The scan mirror and the reference mirrors are driven by waves derived from the same electronic source, an IRIG time code generator, but the phases of the reference-mirror drives are not locked to the scan-mirror motion. Consequently, the reference-mirror rotation can slip relative to the data interval, with resultant loss of the cold, or cold and hot references from the digital output. Failure of the data acquisition system can also result in loss of the references. The analog outputs always contain the references, but not always during the time of sampling and digitization.

The need for bar-source calibration results from peculiarities of the longwave detector-array and its electrical connections illustrated in Figure 8. The detectors in the two columns make contact with a common gold film deposited on the array chip. The ends of the gold

film are connected to circuit ground by two platinum wires with resistances of about 0.5 ohms each. The instantaneous summed current $\Sigma I_n(t)$ from the detectors returns to the gold common through the platinum wires. The resulting voltage across the wires subtracts from the output $E_n(t)$ of each detector, i.e.,

$$I_n(t) = C_n E_n(t) - D_n \Sigma I_n(t). \quad (1)$$

Figure 9 illustrates the effect of this resistive coupling on the output produced by a wide bar source. R. A. Steinberg has shown how to determine C_n and D_n from measurements of x and y in the figure.³ Note that equation (1) is valid, and the coupling constants are the same, for all waveforms. Use of the bar-source waveform for determining C_n and D_n is a matter of convenience. That is, the true waveform is known in this case so that the artifacts are easy to identify. In addition, the equations relating the coupling constants to x and y are rather simple, although they must be solved by numerical iteration. Once C_n and D_n have been found from the bar-source calibration, however, they can be used in equation (1) with measured outputs $I_n(t)$ from any source to find the true outputs $E_n(t)$ from that source. All longwave data are corrected in this way.

1.3 RESULTS, DISCUSSION, CONCLUSIONS, RECOMMENDATIONS

1.3.1 Attempted Calibration at Montauk Point

The initial attempt at radiometric calibration was made by the Naval Surface Weapons Center (NSWC), White Oak, during background measurements at Montauk Point, Long Island, in August 1983. The NSWC procedure was to scan a 45°C, one foot square blackbody placed 70 feet from the radiometer.

This procedure involves a number of difficulties as follows. Corrections must be made for atmospheric attenuation of the blackbody radiation. Since only one blackbody temperature was used, the offsets (reference radiation) of the detectors cannot be determined; only

the gains (responsivities) are approximately determinable. Since the radiometer's telescopes are focused on infinity, the blackbody images on the detectors were defocused (Fig. 10). The defocused images had cores of unknown, uniform radiance surrounded by borders of unknown, nonuniform radiance (Fig. 11). Since the telescopes lie above and below the radiometer's centerline, the images were displaced by parallax from the centers of the detector arrays (Figs. 11 and 12). Consequently, some detectors of each array were illuminated solely by the nonuniform borders of the images (Fig. 11). (In Fig. 11 the detectors are numbered as they have been since Montauk Point. Prior to and at Montauk Point they were numbered oppositely with 1 at low and 16 at high elevation. The figures of Part 3A utilize the old numbering system.)

In principle the radiances of the defocused images could be calculated and used to derive the detector gains. In practice this would be very difficult to do and would give results of highly questionable accuracy. It is recommended that the Montauk blackbody scans not be further analyzed to estimate detector gains because the potential returns are negligible compared to the effort involved. The radiometer's spatial response was well calibrated for the Montauk measurements, so that the background data are valuable without radiometric calibration, as explained in section 1.1.

Several possibilities were considered for changing the NSWV procedure to overcome the problems of defocusing and parallax. The obvious solution is to place the blackbody farther from the radiometer. However, blackbody size and distance must be increased proportionally to keep the entire detector array illuminated. The practical limit of blackbody size makes it impossible to increase the distance sufficiently. Defocusing can be reduced by stops (the pinhole-camera effect) or eliminated by additional lenses ("spectacles"), but then corrections must be made for the effects of these devices in order to obtain a calibration for the radiome-

ter. Obviously little is accomplished in this way. In short, no satisfactory means of improving the NSWC procedure has been found. It is recommended, therefore, that this procedure or variations of it not be used for radiometric calibration.

1.3.2 Survey of Radiometric Calibration

Experience with the NSWC calibration procedure lead to a review of the literature for the purpose of developing a different procedure. References 4-8 were the most useful sources consulted. Answers to three questions were sought:

What is a radiometric calibration?

How is it obtained?

What does it give when used to reduce background data?

The answers to these questions are not unique. They depend on the data usage, the instrument, the scene, and the field conditions.

As already noted, BMAP data are to be used for comparing and evaluating IRST designs by simulation of their performance. This use requires data in radiance units for simulating optical sensors with arbitrary apertures and instantaneous fields of view (IFOV). The BMAP radiometer should, therefore, be calibrated directly in radiance units. Calibrations in units of irradiance, intensity, or power would have to be converted to radiance units. This would require measurements of the radiometer's aperture and/or IFOV, which would involve additional effort and error.

A radiometer responds to radiation in a broad passband of wavelengths from λ_1 to λ_2 . The output depends on received power, the product of received radiance with the constant IFOV and aperture area. Thus, output can be expressed as a function of spectral radiance $L(\lambda)$ integrated over the passband. For data reduction, however, the inverse relation giving integrated radiance as a function of output v is wanted, i.e.,

$$R_0 \int_{\lambda_1}^{\lambda_2} r(\lambda) L(\lambda) d\lambda = f(\nu), \quad (2)$$

where $R_0 r(\lambda)$ is the radiometer's spectral response. R_0 is the instrument's responsivity at the arbitrary wavelength λ_0 where the response function $r(\lambda)$ is normalized to unity.

Radiometric calibration is the process of determining integrated radiance as a function of radiometer output from measurements of the outputs produced by a standard source. The radiance of the standard source should be varied over a range such that the outputs encompass the range of outputs produced by the unknown sources. Calibrations always depend on the radiometer's spectral response; measured radiances of unknown sources do also if equation (2) is used for calibration. However, the desired quantities are the integrated radiances of the unknowns without instrumental dependence. There are two ways of calibrating so that the measured radiances are independent of the radiometer's spectral response. Neither involves equation (2), and both require matching the spectrum of the standard to that of the unknown at some point along the line of sight.

The best of the two special calibrations gives a relation between radiometer output and integrated clutter radiance, i.e.,

$$\int_{\lambda_1}^{\lambda_2} L_c d\lambda = f_1(\nu), \quad (3)$$

where L_c is the clutter's spectral radiance. To determine this relation experimentally, it is necessary to use a standard source with the same spectrum as the clutter and to place the source beside the clutter so that the atmosphere affects source and clutter radiation identically. BMAP conditions forbid doing either because the scenes contain objects, including clouds, at different ranges with different spectra. Thus, the desired calibration is unattainable in BMAP because (1) the necessary standard sources are unavailable, and (2) they could not be deployed properly if they were available. (This type of calibration is best because the

measured clutter radiances do not depend on either the radiometer's spectral response or meteorologic conditions. The calibration depends on both but includes them in such a way that its use to reduce the background data makes the results independent of these conditions. It is not even necessary that the instrument's passband include the integration range wholly or partly; it is only necessary that radiation in the two wavebands be uniquely related.)

The second special calibration gives a relation between radiometer output and integrated scene radiance at the radiometer's entrance aperture, i.e.,

$$\int_{\lambda_1}^{\lambda_2} [\tau_a(d)L_c + L_a(d)]d\lambda = f_2(v), \quad (4)$$

where d is range to the clutter and (τ_a, L_a) are the spectral (transmittance, radiance) of the intervening atmosphere. A standard source with the same spectrum as the scene radiation at the entrance aperture is needed for this calibration. Such a source is unavailable for BMAP because the scene spectra at the entrance aperture are unknown and variable. (This type of calibration gives measured radiances independent of the radiometer's spectral response but not of meteorologic conditions. Matching the spectra of the standard and unknown sources always provides independence from spectral response but not from meteorologic conditions when the spectrum includes atmospheric effects.)

Since the spectra of the standard source and scene cannot be matched under BMAP conditions, it is necessary to use an arbitrary standard. The usual choice is a blackbody. The measured scene radiances then depend on both the radiometer's spectral response and meteorologic conditions, which must be recorded when the background data are collected. The BMAP radiometer's view port is a convenient fiducial point for radiance regardless of the blackbody's location. The calibration equation in this case is

$$R_0 \int_{\lambda_1}^{\lambda_2} r[\tau_a L_b + L_a]d\lambda = f_3(v), \quad (5)$$

bration should not be used outside its range. The same types of results for all midwave and longwave channels are given in Table 5 and 6, where the variances are the squared standard errors of estimate, and the 95% prediction limits are calculated at values of u for which the output v is about 25, 50, 75, and 100% of full scale.

Further measures of calibration quality can be obtained as follows. Assume ideal conditions, that is, errorless calibrations and measurements made with an extended source perfectly uniform in space and time. Then radiances calculated from the *dc* coupled midwave outputs should be identical across and along the channels at each and every sample number. Radiances calculated from the *ac* coupled longwave outputs should be identical across the channels at each sample number but should droop slightly with increasing sample number. This can be visualized with the aid of Figure 15 by imagining the quantity on the vertical axes to be radiance. Beyond the 140th sample and under ideal conditions, the midwave plots should be in a horizontal plane; the longwave plots should be in a plane sloping downward to the right, ignoring slight curvature of the droop. Furthermore, under ideal conditions, midwave (or longwave) radiances at the same sample number should be the same in all frames. Departures from ideal conditions cause differences in radiances at the same sample number both within and between frames.

What actually is observed in contrast to the ideal? Figures 20 and 21 show cross-channel-average radiance calculated at each sample number from data recorded with a near extended blackbody at 50.0°C. Figures 22 and 23 show the cross-channel standard deviations of the radiances at each sample number. Under ideal conditions, the midwave averages should be on a horizontal line; the longwave averages should be on a line sloping down to the right, again ignoring slight curvature of the droop; and the standard deviations should be zero. The departures from ideal behavior are small and apparently random except for a slight

1.3.8 Radiometric Calibrations Derived and Evaluated

The radiometric calibration on tape BF7 was reduced as follows. First, the radiometer outputs were processed to remove "transients," features which rise or fall more rapidly than the radiometer's point response allows. Next, resistive coupling artifacts (section 1.2) were removed from the longwave outputs. (These corrections are applied routinely to all data R. A. Steinberg originated both.) Then values of the response-weighted radiance integral $\langle rL_b \rangle$ were calculated for each external blackbody temperature in Table 3 using the response functions of Figures 16 and 17. Finally, equation (26) was fit by least squares to the fractional outputs u and integrated radiances $\langle rL_b \rangle$ to determine offsets A and gains B for all midwave and longwave channels. (Longwave data at a blackbody temperature of 30°C were not used because the outputs had no cold references.)

Results for one midwave and one longwave channel are presented in Figures 18 and 19. The equations fit the data so well that the plots fail to show differences between the two. These are revealed only by the statistical measures of the fits. The standard error of estimate is the standard deviation between the observed radiances and those calculated from the calibration equations. The sample correlation is the fraction of the relation between u and $\langle rL_b \rangle$ accounted for by the linear dependence. With reference to Figure 18, for example, the 95% confidence intervals and limits of prediction have the following meanings: The probability is 95% that the offset A lies in the range, $-0.251 \pm 3.4 \times 10^{-3} \text{ W/m}^2\text{-sr}$. If the output is one-quarter of full scale (f.s.), the probability is 95% that the true integrated radiance lies within $\pm 6.0 \times 10^{-3} \text{ W/m}^2\text{-sr}$ of the value given by the calibration equation. Of course these measures refer only to the precision of this one calibration, not to its reproducibility or accuracy. Notice that the limits of prediction are smallest at the center of the calibration range and increase with the magnitude of the departure from the center; this is one reason a cali-

gain or to subtract a constant voltage from the analog output. Reducing gain is inadvisable since the longwave clutter lies mainly in the top half of the present digital range, so that actually an increase of gain is desirable. Subtracting a strictly constant voltage from the analog output is awkward and difficult. The best solution is to use an A/D converter with a maximum greater than the present 4096, which also would allow an increase of gain.

1.3.7 Field Measurements

During the week of 10-14 September 1984, cloud background data were collected from a rooftop site at Raytheon Missile Systems Division overlooking Hanscom Air Force Base. After equipment setup on the first day, data were collected in good weather on the second to fourth days, but not on the fifth day when the weather was bad. A radiometric calibration was put at the end of each data tape according to the procedure for field calibration given in section 1.3.5.

Eight tapes were made in this way. The tapes and supporting documentation (notes, radiometer logs, meteorologic logs, and camera logs) are already in the sponsor's possession. Plots of selected data frames were made to spot check the tapes. The plots show massive failures of the data acquisition system with the result that only the seventh and eighth tapes are useful. Tables 3 and 4 summarize the radiometer logs for these tapes, showing the time required for the calibrations and how they are put on the tapes. Either the midwave or the longwave calibration takes less than five minutes. The two had to be made separately because the blackbody was not large enough to cover both telescopes. With a commercially available blackbody twice as high, the two calibrations could be made simultaneously in less than five minutes by recording the outputs in the A (alternating) mode. From the standpoint of the time required, the procedure employed is certainly practicable. It is even feasible to calibrate more often than once per tape should the calibrations be temporally or thermally erratic.

30°C. However, the resistive coupling artifacts in Figure 14 were not completely removed by coupling parameters derived about a year earlier from outputs of a wider single-bar source (Figure 9). Clearly the coupling parameters changed with time. Accordingly, new coupling parameters were determined from the more recent measurements, even though x and y of Figure 9 are not as easily measured from a narrow output. For this reason a wider bar target should be used in the future.

Radiometric calibrations made in the laboratory have not yet been reduced, although the detector outputs have been plotted and assessed. (The 196 plots have been given to the sponsor separately to avoid making this report too bulky. Figure 15 displays examples from the set.) The plots show that the cold reference level is sometimes missing, owing either to failure of the data acquisition system or to slippage between the data interval and the reference mirror rotation. For this reason, the entire midwave calibration at a radiometer temperature of 30°C, and certain frames of the calibrations at 25 and 35°C, may be unusable. In addition, stray radiation tends to distort or saturate the hot reference peak at high radiometer and standard source temperatures. For this reason, the midwave calibration with the radiometer at 40°C and the standard source at 50°C may be unusable. Despite these shortcomings prospects are good for successfully reducing most of the midwave calibrations. The opposite is true of the longwave calibrations. Those at radiometer temperatures of 25 and 30°C were made but not recorded because of operator error. At 35 and 40°C the cold reference is missing, and the hot reference is often saturated by stray radiation. Of all the longwave laboratory calibrations, only the one at a radiometer temperature of 20°C appears usable.

Saturation of the hot reference by stray radiation probably makes the longwave radiometer unusable above 30°C = 86°F. This serious limitation should be removed. Saturation occurs in the digital, not the analog output. Potential solutions are to reduce the amplifier

3. Near extended source scans
 - a. Place source over view port in contact with radiometer housing.
 - b. Record four frames of data from each detector array.
 - c. Do b with source at 10, 20, 30, 40, 50°C.
4. Do 1-4 with radiometer at 20, 25, 30, 35, 40°C.

The following simpler procedure is used in the field:

1. Point source scans
 - a. Center image from portable collimated source vertically on pixel.
 - b. Record four frames of data.
 - c. Do a-b for channels 2, 8, 15 of detector array.
 - d. Do a-c for both arrays.
2. No bar source scans.
3. Near extended source scans
 - a. Same procedure as in laboratory.
 - b. Record scans at end of each data tape.

1.3.6 Laboratory Measurements

The BMAP radiometer was calibrated in the laboratory at Raytheon Missile Systems Division, Bedford, Massachusetts on 23 August 1984 by the procedure in the previous section. The notes, logs, and digital tapes made at that time have been turned over to the sponsor.

Typical point-source outputs with the radiometer at 20.6°C are shown in Figure 4. Figure 14 is a representative bar-source output at the same radiometer temperature. The shapes and widths of these outputs indicate an acceptable spatial response for the radiometer at 20-

temperature. For that reason the responses must be calibrated in both the laboratory and the field. Laboratory calibrations are needed to provide baseline measures of the responses. In the laboratory, conditions can be controlled and reproduced; measurements can be made slowly with care and repeated to be sure they are correct. Then a simpler, faster calibration in the field is sufficient to verify the radiometer's response by comparison with the laboratory results.

The laboratory calibration setup is illustrated in Figure 13. Point and bar sources are placed at infinity, in effect, through use of a collimating mirror. The radiometer is put on a micrometer stage, allowing the point-source image to be centered carefully on each detector for determining the point responses. The bar source is high enough to illuminate all detectors of an array simultaneously. For radiometric calibration an extended blackbody source is placed over the radiometer's view port in contact with the instrument's housing. The radiometer's temperature is varied systematically to obtain the temperature dependence of the point, bar and radiometric responses. To investigate the temporal stability of the responses, all of these measurements are made at intervals of days, weeks or months.

The step-by-step procedure for laboratory calibration is as follows:

1. Point source scans
 - a. Center point-source image vertically on pixel.
 - b. Record four frames of data.
 - c. Do a-b for all channels of detector array.
 - d. Do a-c for both arrays.
2. Bar source scans
 - a. Center 50°C bar target vertically on detector array.
 - b. Record two frames of data from each array.

The radiometer output with the standard source in place (ignoring atmospheric radiance) is

$$v = \gamma \langle f'(\tau L_b + l) \rangle + (\gamma \langle f \rangle + \delta). \quad (23)$$

Subtracting equation (20) from equation (23), dividing the result by equation (22), and rearranging terms gives

$$u = \left[\frac{1}{\langle f'(l_h - l_0) \rangle} \right] \langle f' \tau L_b \rangle + \left[\frac{\langle f'(l - l_0) \rangle}{\langle f'(l_h - l_0) \rangle} \right], \quad (24)$$

where as before $u = (v - v_0)/(v_h - v_0)$ is the fractional output with respect to the hot and cold reference voltages. Solving equation (24) for $\langle f' \tau L_b \rangle$ gives the broadband calibration equation for the BMAP radiometer,

$$\langle f' \tau L_b \rangle = \langle f'(l_h - l_0) \rangle u - \langle f'(l - l_0) \rangle. \quad (25)$$

For convenience, equation (25) is written in terms of a response function r and broadband offset and gain parameters A and B .

$$\langle r L_b \rangle = A + B u \quad (26)$$

The response function includes the detector's response f' and all radiative losses τ in the atmosphere and optics between source and detector. Emission from the optics is included in the offset through the stray radiance l . The offset and gain include the response of the detector but not the electronics. With broadband radiation, expressing the output by the ratio u compensates the calibration parameters for electronics drift but not detector drift. Nonetheless, radiometer temperature probably will affect the broadband parameters as it does the monochromatic ones, i.e., gain probably will increase slowly and offset more rapidly with temperature.

1.3.5 Calibration Procedure

The spatial and radiometric responses of the BMAP radiometer may vary with time and

most of l_h , so the increase of $(l_h - l_0)$ with temperature should be slow. This will result in a slow increase of the gain $(l_h - l_0)/\tau$ with temperature. The difference $(l - l_0)$ will increase with temperature more rapidly than $(l_h - l_0)$, since l consists entirely of stray radiation from the radiometer's main optics and interior. The offset $(l - l_0)/\tau$ should, therefore, increase with temperature more rapidly than the gain.

B. Broadband Radiation

Integration over wavelength changes these results very little, as will now be demonstrated. For convenience, the integration will be performed over all wavelengths so that the limits are effectively set by the cut-offs of the spectra and responses. This avoids conceptual problems arising from the fact that scene radiation, standard radiation, internal reference radiation and stray radiation follow different optical paths and have different spectra at the detector. The results are the same as those obtained by integrating over the spectral passband and accounting separately for the differences in paths and spectra, provided the passband is chosen as described in section 1.3.2. For simplicity, the integration will be denoted by angular brackets, i.e.,

$$\langle g \rangle = \int_0^\infty g \cdot d\lambda.$$

From equation (12) the spectrally integrated radiometer output is

$$v = \gamma \langle f'l \rangle + (\gamma \langle f \rangle + \delta). \quad (19)$$

With the cold or hot reference mirror in place, the outputs are

$$v_0 = \gamma \langle f'l_0 \rangle + (\gamma \langle f \rangle + \delta), \quad (20)$$

$$v_h = \gamma \langle f'l_h \rangle + (\gamma \langle f \rangle + \delta). \quad (21)$$

The amplification factor, which now does not include the detector response f' , is given by

$$v_h - v_0 = \langle f'(l_h - l_0) \rangle \gamma. \quad (22)$$

for stray radiation and τ for losses of radiation between the source and detector. (Atmospheric radiance is ignored.) With the standard source in view, the voltage-radiance relation is

$$v = \gamma f'(\tau L_b + l) + (\gamma f + \delta) \quad (16a)$$

$$= \gamma f' \tau L_b + (\gamma f' l + \gamma f + \delta). \quad (16b)$$

Subtracting equation (13) from equation (16b) and dividing the result by equation (15) gives

$$u = \frac{v - v_0}{v_h - v_0} = \left(\frac{\tau}{l_h - l_0} \right) L_b + \left(\frac{l - l_0}{l_h - l_0} \right). \quad (17)$$

This relation expresses the radiometer's output as a fraction u of the output voltage with the hot reference mirror in place, all voltages being measured from the cold reference level v_0 . Solving equation (17) for L_b gives a monochromatic calibration equation for the BMAP radiometer.

$$L_b = \left(\frac{l_h - l_0}{\tau} \right) u - \left(\frac{l - l_0}{\tau} \right) \quad (18)$$

Equation (18) does not involve the responses of the detectors and electronics. These are accounted for in the variable u through v_0 and v_h , which are measured before each scan. Thus, the calibration is compensated for drifts of the detectors and electronics over times longer than the scan time.

The bracketed terms in equation (18) correspond to the radiometer gain and offset parameters. This allows the temperature dependence of the parameters to be predicted. The loss factor τ probably depends weakly on radiometer temperature. The radiance l_0 increases slowly as the temperature of the cold reference mirror increases. The difference $(l_h - l_0)$ will increase with temperature since l_h includes stray radiation from the internal reference optics and the radiometer's interior. However, radiation from the internal hot source accounts for

and add a voltage δ (Fig. 6), so that the voltage-radiance relation for the whole radiometer becomes

$$v = \gamma f' l + (\gamma f + \delta). \quad (12)$$

(Throughout this section, the same symbol v is used for all voltage outputs with the precise meaning indicated by context and subscripts.) The factors γ and δ are constant only if the electrical and thermal variables of the system are fixed. The added voltage δ is chosen so that the radiometer output is v_0 when the detector is completely covered by the cold reference mirror (Figs. 5 and 7). During the time of complete coverage, the radiance l_0 at the detector comes from emission by the mirror and reflection of the detector's own radiation back to it. Hardly any stray radiation reaches the detector during this time. The voltage-radiance relation with the cold reference mirror in place is

$$v_0 = \gamma f' l_0 + (\gamma f + \delta). \quad (13)$$

The hot reference mirror follows the cold reference mirror through the field of view. With the hot reference mirror in place, most of the radiance l_h at the detector comes from the internal hot source and the optics which transfer its radiation to the detector. However, stray radiation from the radiometer's interior also reaches to the detector at this time (Fig. 5). The peak hot reference voltage (Fig. 7) is

$$v_h = \gamma f' l_h + (\gamma f + \delta). \quad (14)$$

The difference between the hot and cold reference voltages gives a relation for the amplification factor $\gamma f'$.

$$v_h - v_0 = (l_h - l_0) \gamma f' \quad (15)$$

For calibration the radiometer's view port is covered by an extended blackbody of radiance L_b . Under these conditions the radiance at the detector is $(\tau L_b + l)$, where l accounts

actual use an equation which accounts for specific features of the BMAP radiometer is needed. That equation is obtained by analyzing the response of the detectors and electronics to scene, internal reference, and stray radiation. The analysis also indicates how the calibration parameters should depend on the radiometer temperature. Only the midwave radiometer's response is analyzed since, as already explained, the longwave radiometer responds in approximately the same way because of its very long electronic time constant. The response to monochromatic radiation will be derived first, then the analysis will be extended to broadband radiation. This will avoid obscuring the essential features of the response in the fog of integration over the spectral passband.

A. Monochromatic Response

Assume that the detector output voltage v is an analytic function of the optical (O), thermal (T), and electrical (E) variables of the instrument and environment, $v = H(O, T, E)$. If all variables except power p received by the detector are fixed, $v = h(p)$, and since power is the product of throughput ($\text{IFOV} \times \text{aperture area}$) with radiance I at the detector, $v = f(I)$. This relation can be expanded in a Maclaurin series.

$$v = f(0) + f'(0)I + \frac{1}{2}f''(0)I^2 + \dots \quad (10)$$

The coefficients of the series are functions of all the system variables except I and, therefore, are constants only if all variables except radiance at the detector are fixed. It will be assumed that the first two terms of the series adequately represent the voltage-radiance relation. Then

$$v = f + f'I, \quad (11)$$

where the point of series expansion has been omitted for simplicity.

The midwave detector output is dc coupled to electronics which amplify it by a factor γ

In summary, this section has (1) demonstrated that the BMAP radiometer should be calibrated with a blackbody radiance standard, (2) described the rational basis of such a calibration, and (3) explained the meaning of scene radiances determined with the calibration.

1.3.3 Selection of Blackbody Calibration Technique

The possible ways of calibrating a radiometer with a blackbody standard can be classified very simply: The source can be large or small, and it can be placed close to the radiometer or far from it (Table 2). The most important attributes of a calibration technique for BMAP usage are listed at the left of Table 2. Some of these derive from the fact that the technique must be usable in the field as well as the laboratory. A few comments will clarify the meaning of and need for the listed attributes. A technique which does not require focusing on the standard is best since the radiometer's telescopes provide little or no focusing. Corrections for atmospheric attenuation of the standard radiation can be avoided by placing the source close to the radiometer. Background radiation should not reach the detector during calibration. Radiation from the standard should pass through all parts of the aperture as the background radiation does when data are collected. The standard should be commercially available to avoid the time and expense of developing a special source. For use in the field, the calibration procedure must be fast and simple. The source must be easy to handle, control and position in the field of view, and it must illuminate the whole array to allow simultaneous recording of all detector outputs. Table 2 indicates advantage, neutrality, disadvantage, or uncertainty for the possible calibration techniques with respect to the listed attributes. Clearly, the near-extended-source technique is best for calibration of the BMAP radiometer.

1.3.4 BMAP Calibration Equation

Equation (6) of section 1.3.2 exhibits the calibration equation in general form, but for

where the parameters g and g' are determined from measurements of v and

$$\int_{\lambda_1}^{\lambda_2} r[\tau_a L_b + L_a] d\lambda = \int_0^{\infty} r[\tau_a L_b + L_a] d\lambda. \quad (9)$$

Now the limits of integration in equation (8) include all values of the integrand, and so equation (8) describes the radiometer's response to either standard or scene radiation with $L = [\tau_a L_b + L_a]$ or $L = [\tau_a(d) L_c + L_a(d)]$. That is not necessarily true of equation (6) because the calibration passband may exclude significant values of $r[\tau_a(d) L_c + L_a(d)]$ if the scene radiation is very strong outside the passband. In other words, if two sources produce the same radiometer output v ,

$$\int_0^{\infty} r L_1 d\lambda = \int_0^{\infty} r L_2 d\lambda$$

always, but

$$\int_{\lambda_1}^{\lambda_2} r L_1 d\lambda \neq \int_{\lambda_1}^{\lambda_2} r L_2 d\lambda$$

unless the limits of integration include all significant parts of both integrands. Generally the passband cannot be chosen to satisfy this condition because the scene spectra are unknown and variable. The alternative is to choose the passband for calibration to satisfy equation (9). In that case scene radiances calculated from equation (8) are values of

$$\int_0^{\infty} r[\tau_a(d) L_c + L_a(d)] d\lambda,$$

that is, response-weighted scene radiance at the view port integrated over all wavelengths.

With the spectral response written $R_0 r(\lambda)$, the response shape $r(\lambda)$ must be unity at wavelengths where the radiometer's responsivity is R_0 . The spectral response is normalized by selecting a wavelength λ_0 at which $r(\lambda_0)$ is made to equal one. The choice of λ_0 is arbitrary and determines values of both R_0 and $r(\lambda)$. Customarily λ_0 is chosen to be the wavelength at the peak of the spectral response. Both the spectral response and the measured radiances are then described as "peak normalized" or "normalized to unity at the peak."

where L_b is blackbody spectral radiance and (τ_a, L_a) are the spectral (transmittance, radiance) of the atmosphere between the blackbody and the view port. The bracketed term is spectral radiance at the view port during calibration, and the response function includes all radiative losses between the view port and the detector. (Any position between the view port and the blackbody could serve as the fiducial point with appropriate changes in the response and radiance terms.) Ordinarily equation (5) is divided by R_0 and only two or three terms in the series expansion of $g(v) = f_3(v)/R_0$ are retained, with the result

$$\int_{\lambda_1}^{\lambda_2} rLd\lambda = g(v) \\ = g(0) + g'(0)v + \frac{1}{2}g''(0)v^2 + \dots \quad (6)$$

The spectral radiance at the view port is denoted by L in equation (6) so that it can represent either standard or scene radiation in the ensuing discussion of passband determination and the meaning of measured scene radiance.

In practice the radiometer responds, however weakly, to radiation of all wavelengths. Limiting the integration in equation (6) to a finite passband is an approximation. The exact form of equation (6) is

$$\int_0^{\lambda_1} rLd\lambda + \int_{\lambda_1}^{\lambda_2} rLd\lambda + \int_{\lambda_2}^{\infty} rLd\lambda = g(v). \quad (7)$$

The first and third integrals must be negligible compared to the second for equation (6) to approximate the exact equation closely. This requires the passband to include all significant values and all long weak "tails" of the integrand rL . The limits λ_1 and λ_2 are chosen to satisfy this requirement during calibration; hence, the interval λ_1 to λ_2 should be called the "calibration passband." When the calibration satisfies the stated requirement, equation (6) can be written

$$\int_0^{\infty} rLd\lambda = g(0) + g'(0)v, \quad (8)$$

curvature of the longwave averages in the wrong direction. The greatest departure of the midwave averages from a horizontal line through them is about 0.06%. The greatest departure of the longwave averages from a smooth curve through them is about 0.03%, and the total droop is about 0.1%. The midwave and longwave standard deviations are about 0.1% and 0.2% of the respective average radiances. These results indicate high uniformity of the standard source over the scanned part of its surface. They also demonstrate excellent internal consistency of the calibrations; there are no large systematic errors between channels. The smallness of the droop justifies use of the midwave calibration equation (26) for the longwave calibration as well.

1.3.9 Interpretation of Measured Radiances

The passband limits, λ_1 and λ_2 , are chosen so that blackbody radiation outside the passband contributes insignificantly to the integral of response-weighted blackbody spectral radiance L_b , i.e.,

$$\int_0^{\infty} rL_b d\lambda = \int_{\lambda_1}^{\lambda_2} rL_b d\lambda. \quad (27)$$

The equation for the radiometer's response as determined by calibration using equation (26) is then

$$\int_0^{\infty} rL d\lambda = A + Bu, \quad (28)$$

where L is either blackbody or scene spectral radiance at the instrument's view port. The radiometer's response function r includes all radiative losses from the view port to the detector and is normalized to unity at the response peak (Figs. 16 and 17). With a cluttered scene in view

$$L = \tau_a(d)L_c + L_a(d), \quad (29)$$

where L_c is clutter spectral radiance, d is range to the clutter, and (τ_a, L_a) are the spectral

(transmittance, radiance) of the intervening atmosphere. Thus the measured scene radiances are values of

$$\int_0^\infty r[\tau_a(d)L_c + L_a(d)]d\lambda,$$

that is, response-weighted scene radiance at the view port integrated over all wavelengths.

The measured quantities are not those desired, which are the spectral or integrated clutter radiances. These can be derived from the measured quantities as follows. Write the scene spectral radiance in the form,

$$\tau_a(\lambda, d) L_c(\lambda) + L_a(\lambda, d) = L_0 s(\lambda), \quad (30)$$

where L_0 is a constant and $s(\lambda)$ is the scene spectrum at the view port. If both $r(\lambda)$ and $s(\lambda)$ are known, L_0 and the scene spectral radiance at the view port can be determined since

$$L_0 \int_0^\infty r s d\lambda = \int_0^\infty r[\tau_a(d)L_c + L_a(d)]d\lambda. \quad (31)$$

The definite integrals are simply numbers, those on the right hand side being the measured scene radiances. Now if range to the clutter and meteorologic conditions also are known, clutter spectral radiance can be calculated from equation (30) in the form,

$$L_c(\lambda) = [L_0 s(\lambda) - L_a(\lambda, d)]/\tau_a(\lambda, d), \quad (32)$$

using values of atmospheric radiance and transmittance given by a model such as Lowtran 6.

Presently scene radiances at the view port cannot be determined from the response-weighted BMAP radiances because scene spectra at the view port are not known. Clutter radiances cannot be determined for the same reason and also because ranges to the clutter are not known. In addition, the response functions of Figures 16 and 17 may be inadequate for determining scene spectral radiances; if the scene spectra are very strong outside the passbands, values of the responses which are insignificant in equation (27) may be needed to solve equation (31) for L_0 . This seems improbable under BMAP conditions, but the

possibility should be kept in mind. The quantities displayed in Figures 16 and 17 are called passbands and response functions for calibration, because they were determined specifically for calibrating the radiometer and may be unsuitable for other uses. It is recommended that scene spectra and ranges to the clutter be measured if possible, and that the response functions be determined more accurately outside the calibration passbands if necessary.

1.4 REFERENCES

1. M.S. Longmire, A.F. Milton, and E.H. Takken, "Simulation of mid-infrared clutter rejection. 1: One-dimensional LMS spatial filter and adaptive threshold algorithms," *Applied Optics* **21**, 3819 (1982).
2. M.S. Longmire, F.D. Bryant, J.D. Wilkey, and A.F. Milton, "Simulation of mid-infrared clutter rejection. 2: Threshold-sensor-size effects with LMS-filtered noise," *Applied Optics* **24**, 579 (1985).
3. R.A. Steinberg, "Elimination of Sensor Artifacts From Infrared Data," NRL Report 8861, Naval Research Laboratory, Washington, D.C., 1984.
4. C.L. Wyatt, *Radiometric Calibration: Theory and Methods* (Academic Press, New York, 1978).
5. W.L. Wolfe and G.J. Zissis (editors), *The Infrared Handbook* (U.S. Government Printing Office, Washington, D.C., 1978), Chapter 20.
6. F.E. Nicodemus and G.J. Zissis, "Methods of Radiometric Calibration," Report 4613-20-R, AD 289375, Infrared Laboratory, Institute of Science and Technology, University of Michigan, Ann Arbor, MI, October 1962.
7. G. Kelton et. al., "Infrared target and background radiometric measurements - concepts,

units, and techniques," Infrared Physics 3, 139 (1963). (This was originally published as the Report of the Working Group on Infrared Backgrounds (WGIRB), Report No. 2389-64-T, AD 275810, Institute of Science and Technology, University of Michigan, Ann Arbor, MI, January 1962.)

8. F.E. Nicodemus, "Normalization in radiometry," Applied Optics 12, 2960 (1973).

1.5 FIGURES

1. Radiometer Top View (1/2 Scale): Scan Mirror, Telescope, Detector
2. Radiometer Side View (1/2 Scale): Scan Mirror, Telescopes, Detectors
3. Detector-Array Geometry
4. Typical Point-Source Outputs
5. Radiometer Internal References
6. Midwave and Longwave Analog Electronics Diagrams
7. Output Format
8. Origins of Longwave Resistive-Coupling Effect
9. Longwave Bar-Source Outputs with Resistive-Coupling Artifacts
10. Blackbody Image Formation during Attempted Radiometric Calibration at Montauk Point
11. Inverted, Defocused, Parallaxic, Blackbody Image Crossing Midwave Detector at Montauk Point
12. Parallaxic Effects in Montauk Calibration Setup
13. Top View of Laboratory Calibration Setup
14. Longwave Output from a Multiple Narrow Bar Source
15. Typical Frames of Radiometric Calibration Data
16. Midwave Response Function for Calibration
17. Longwave Response Function for Calibration
18. Midwave Calibration, Channel 6, Tape BF7
19. Longwave Calibration, Channel 6, Tape BF7
20. Cross-Channel Averages of Midwave Radiances
21. Cross-Channel Averages of Longwave Radiances
22. Cross-Channel Standard Deviations of Midwave Radiances
23. Cross-Channel Standard Deviations of Longwave Radiances

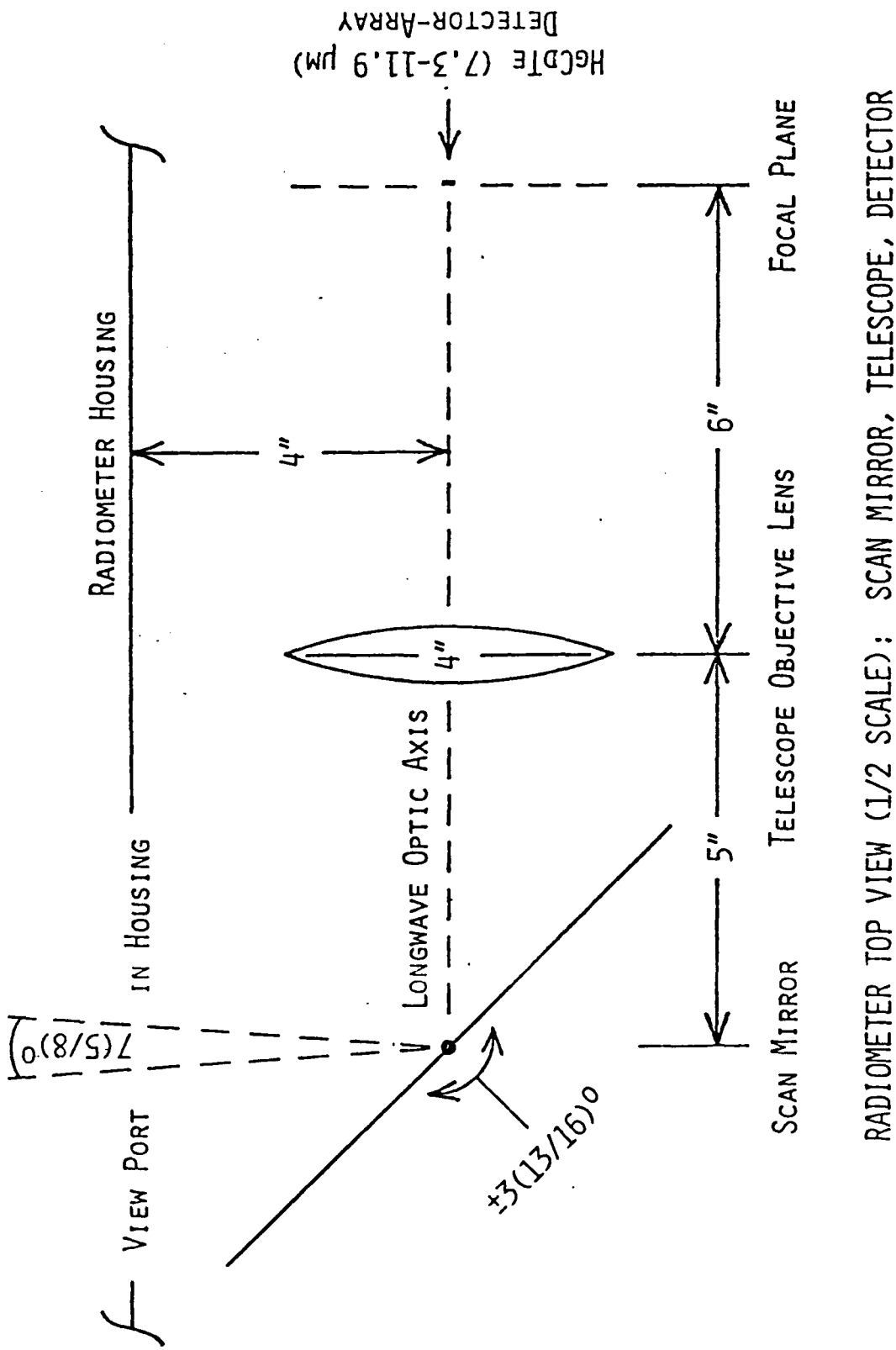


FIGURE 1

RADIOMETER TOP VIEW (1/2 SCALE): SCAN MIRROR, TELESCOPE, DETECTOR

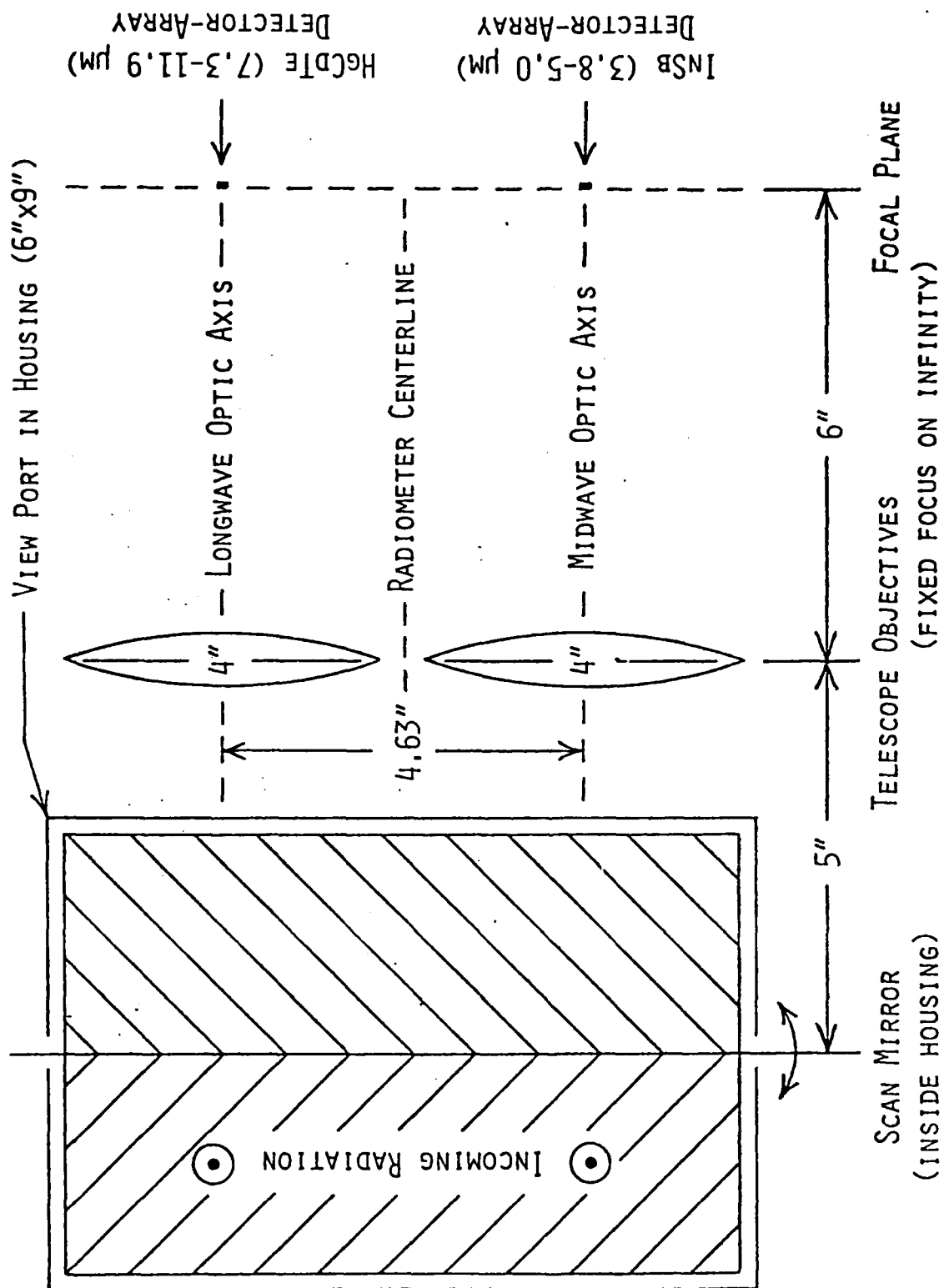
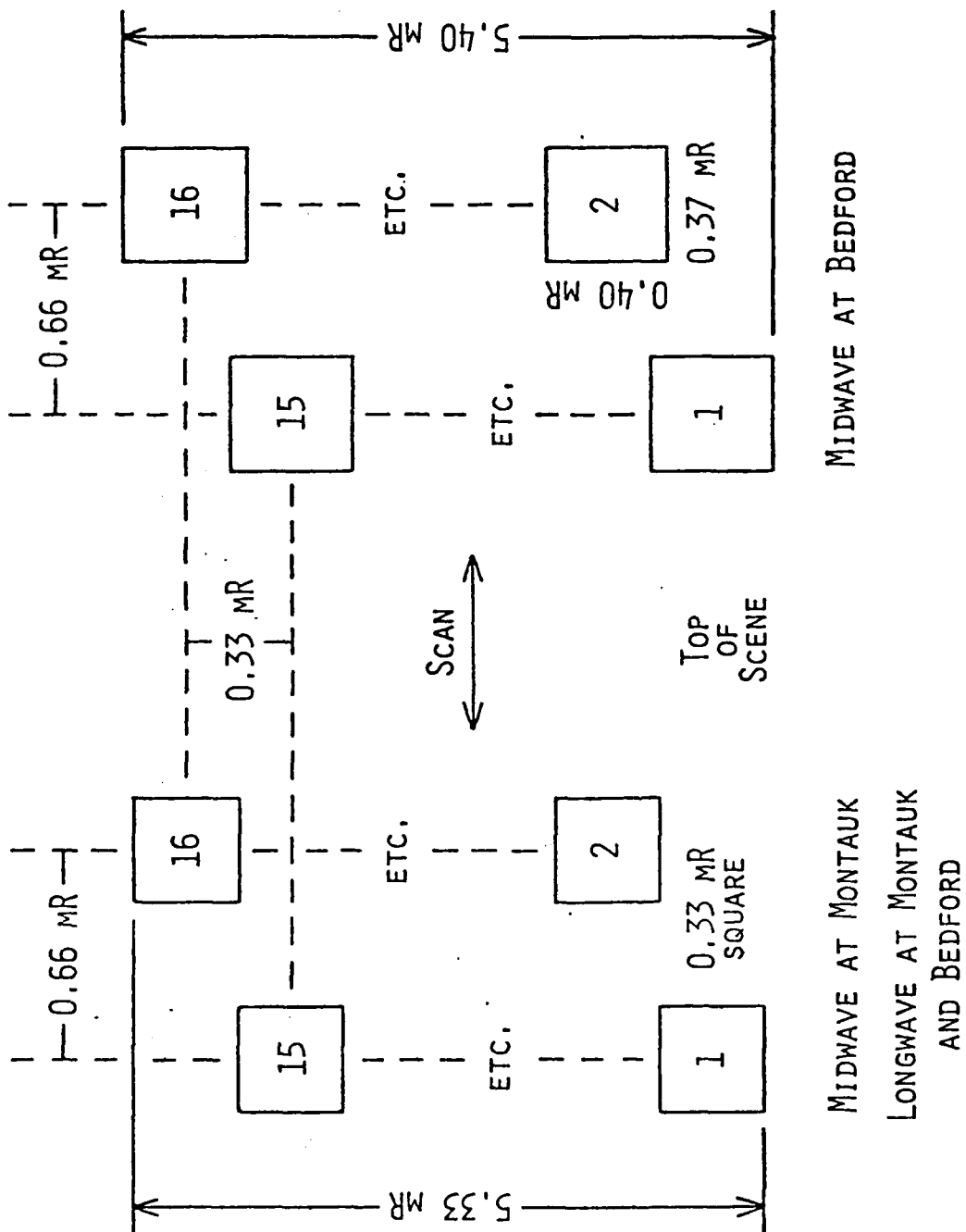
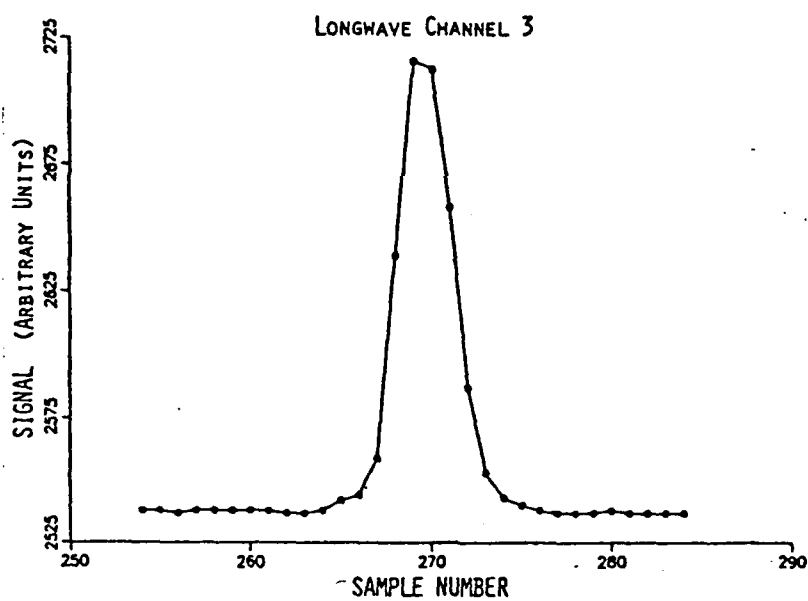
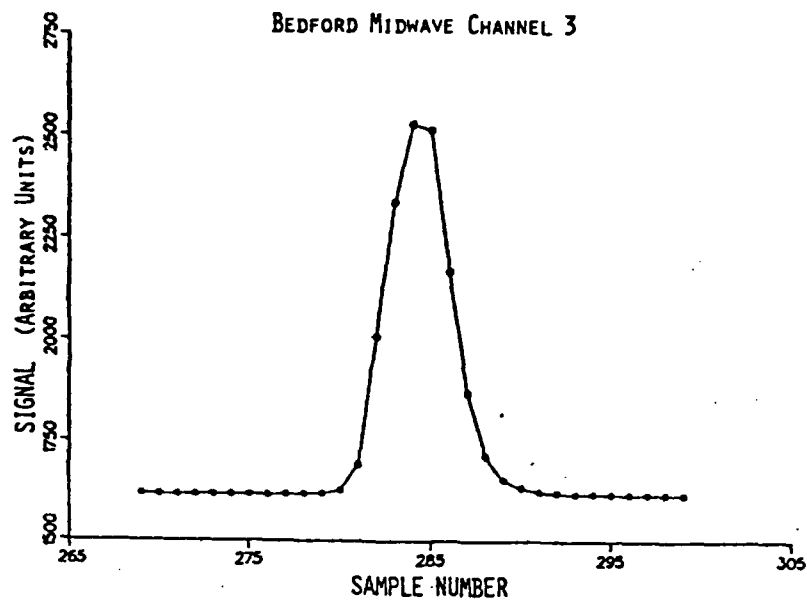


FIGURE 2



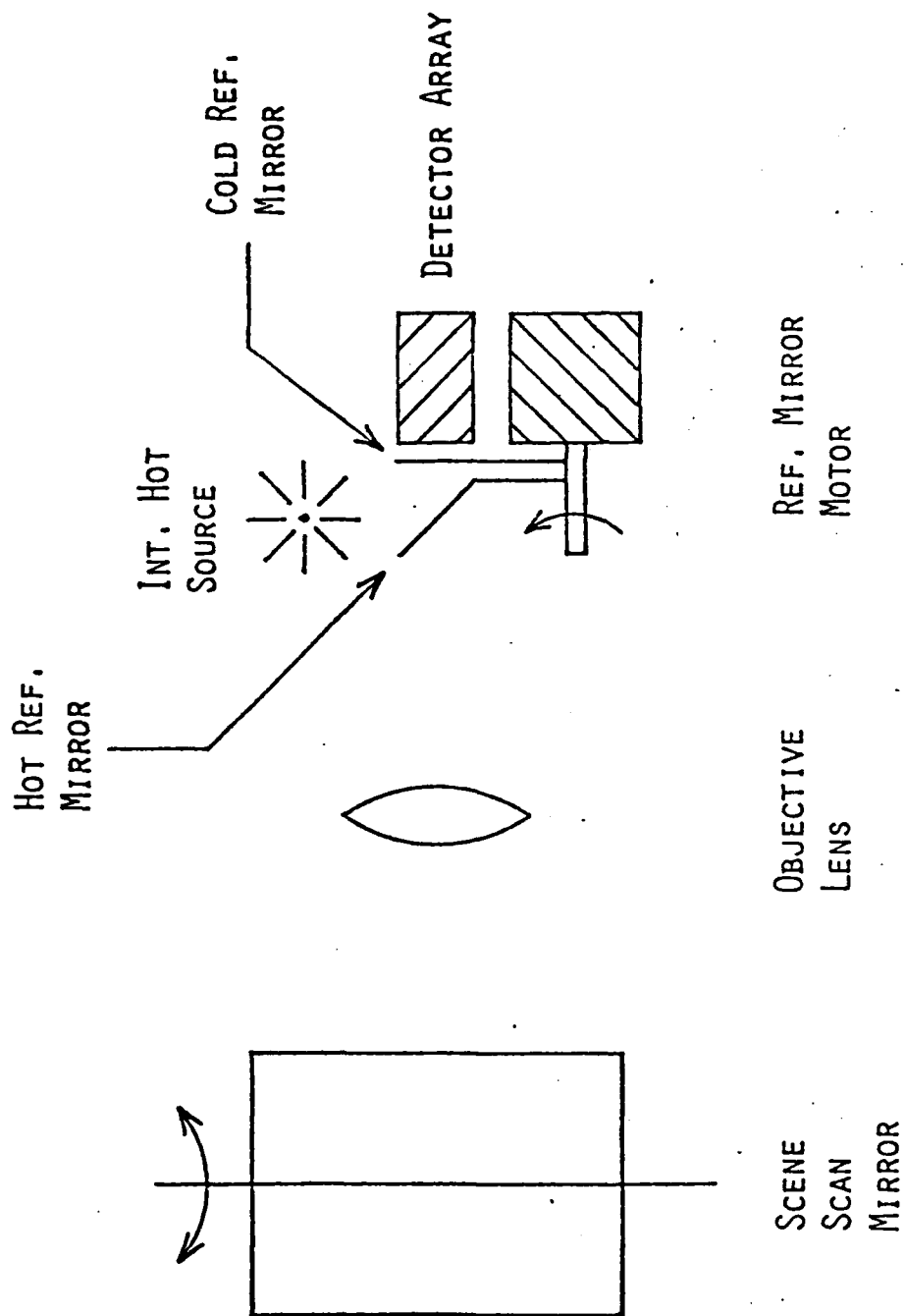
DETECTOR-ARRAY GEOMETRY

FIGURE 3



TYPICAL POINT-SOURCE OUTPUTS

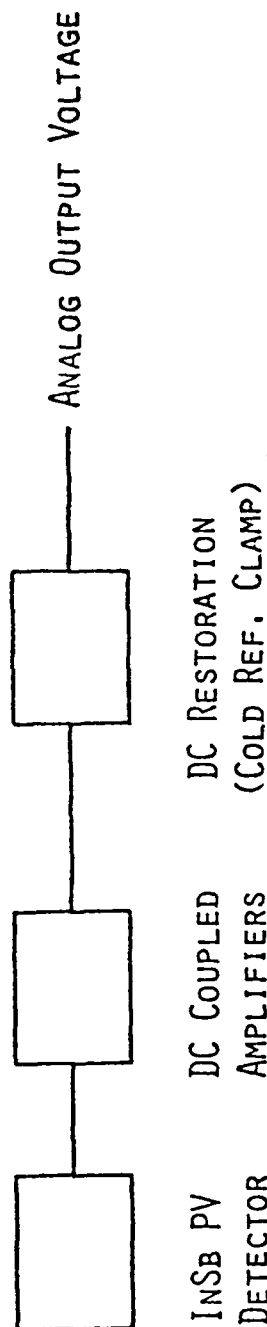
FIGURE 4



RADIOMETER INTERNAL REFERENCES

FIGURE 5

MIDWAVE ANALOG ELECTRONICS DIAGRAM



LONGWAVE ANALOG ELECTRONICS DIAGRAM

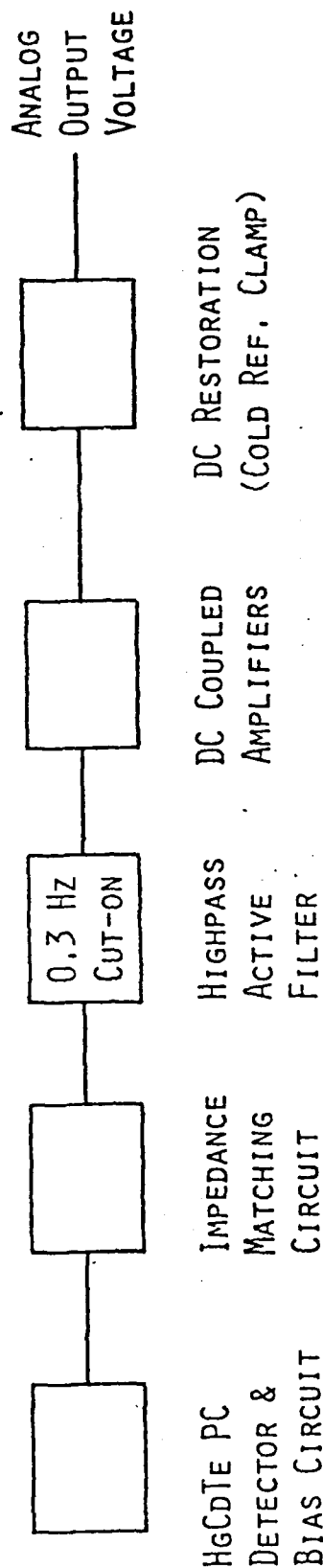


FIGURE 6

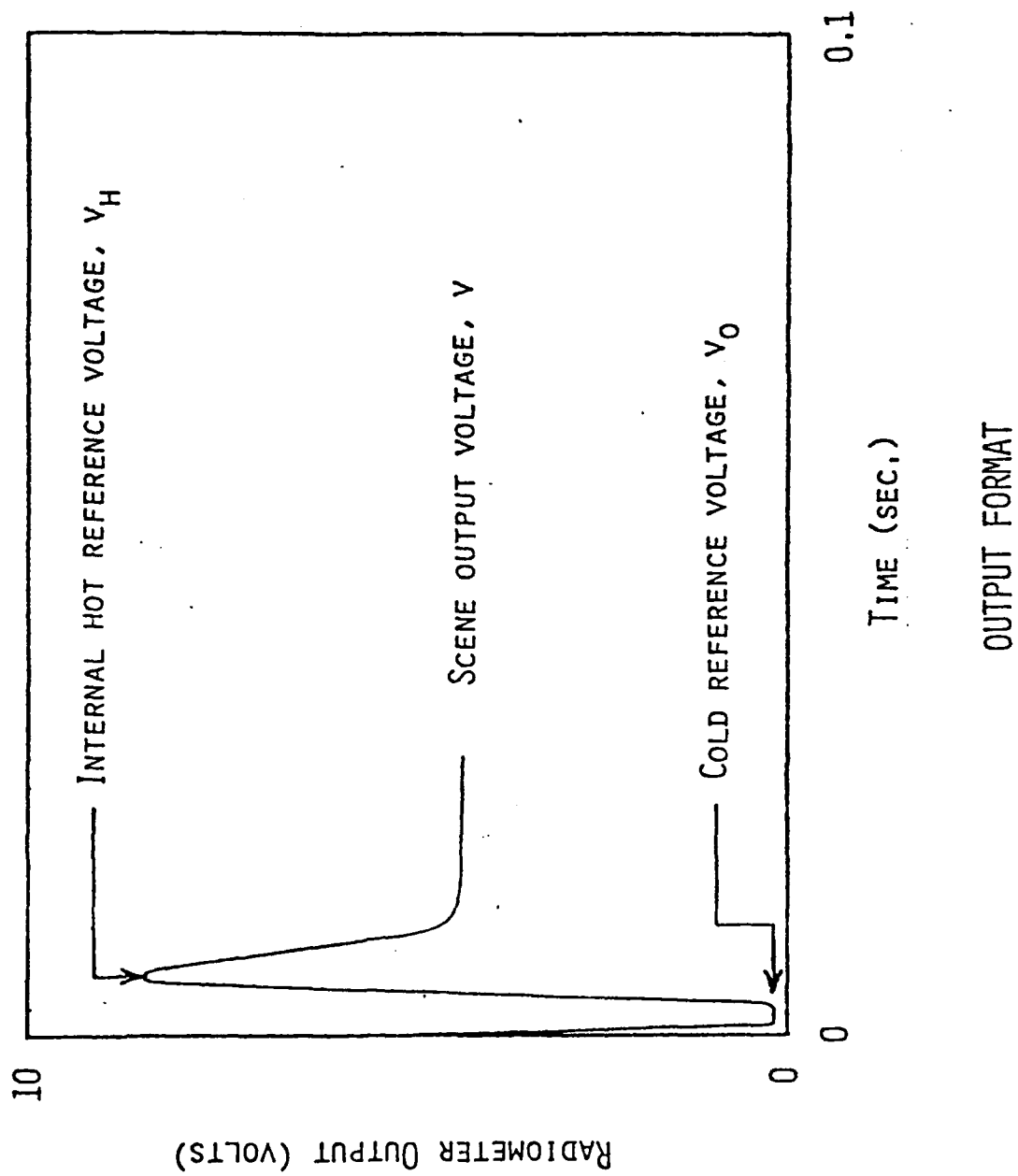
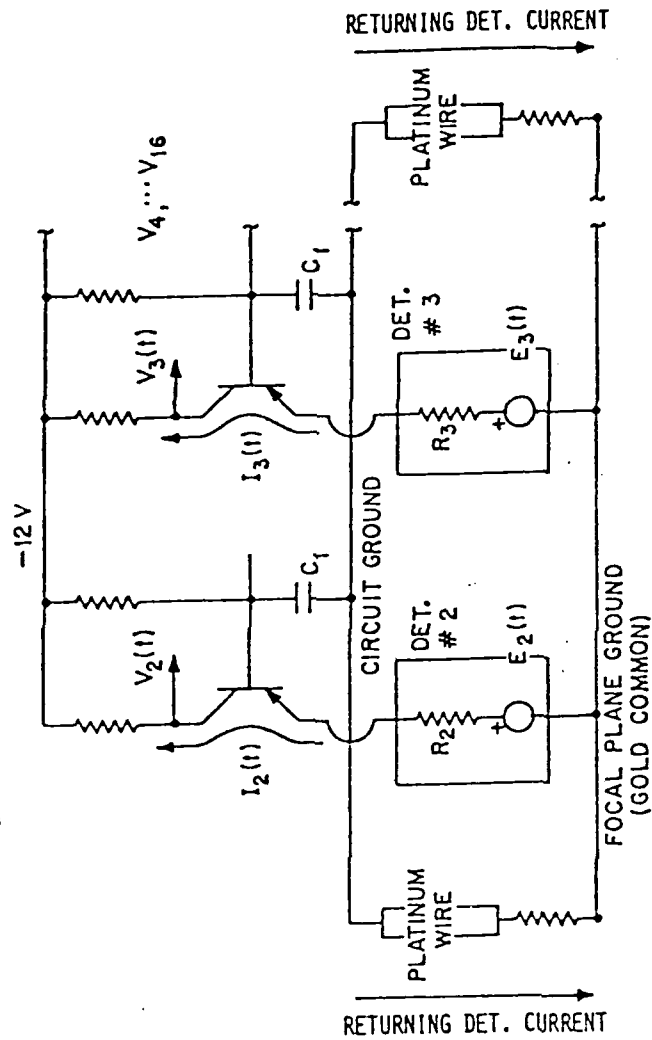
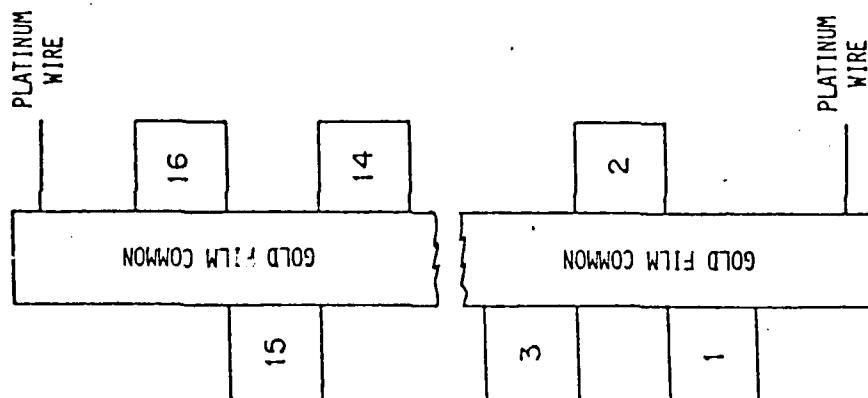
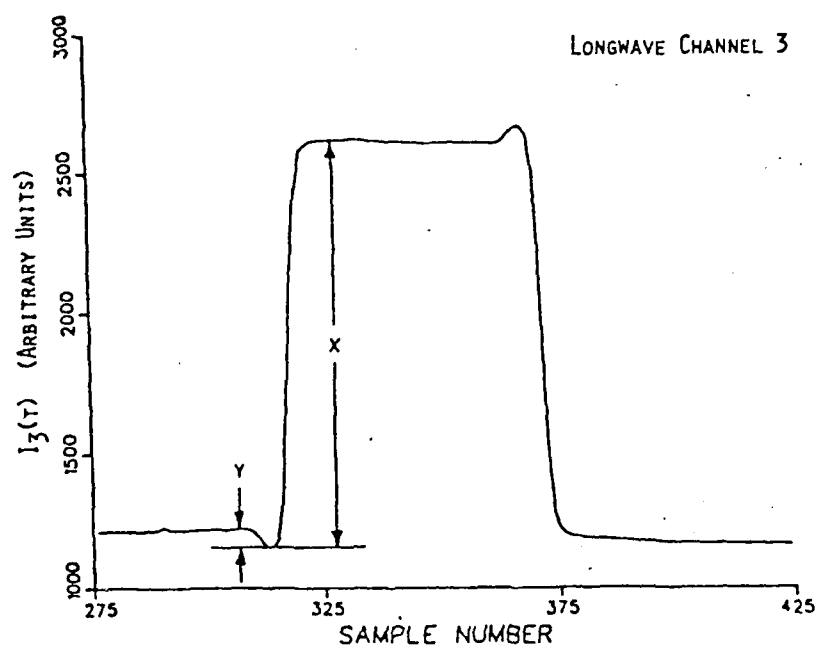
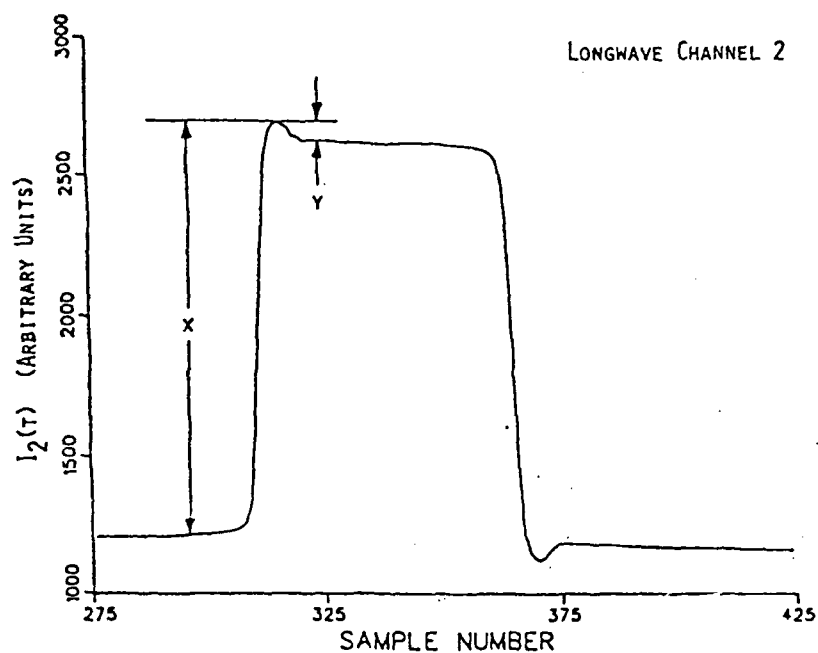


FIGURE 7



ORIGINS OF LONGWAVE RESISTIVE-COUPLING EFFECT

FIGURE 8

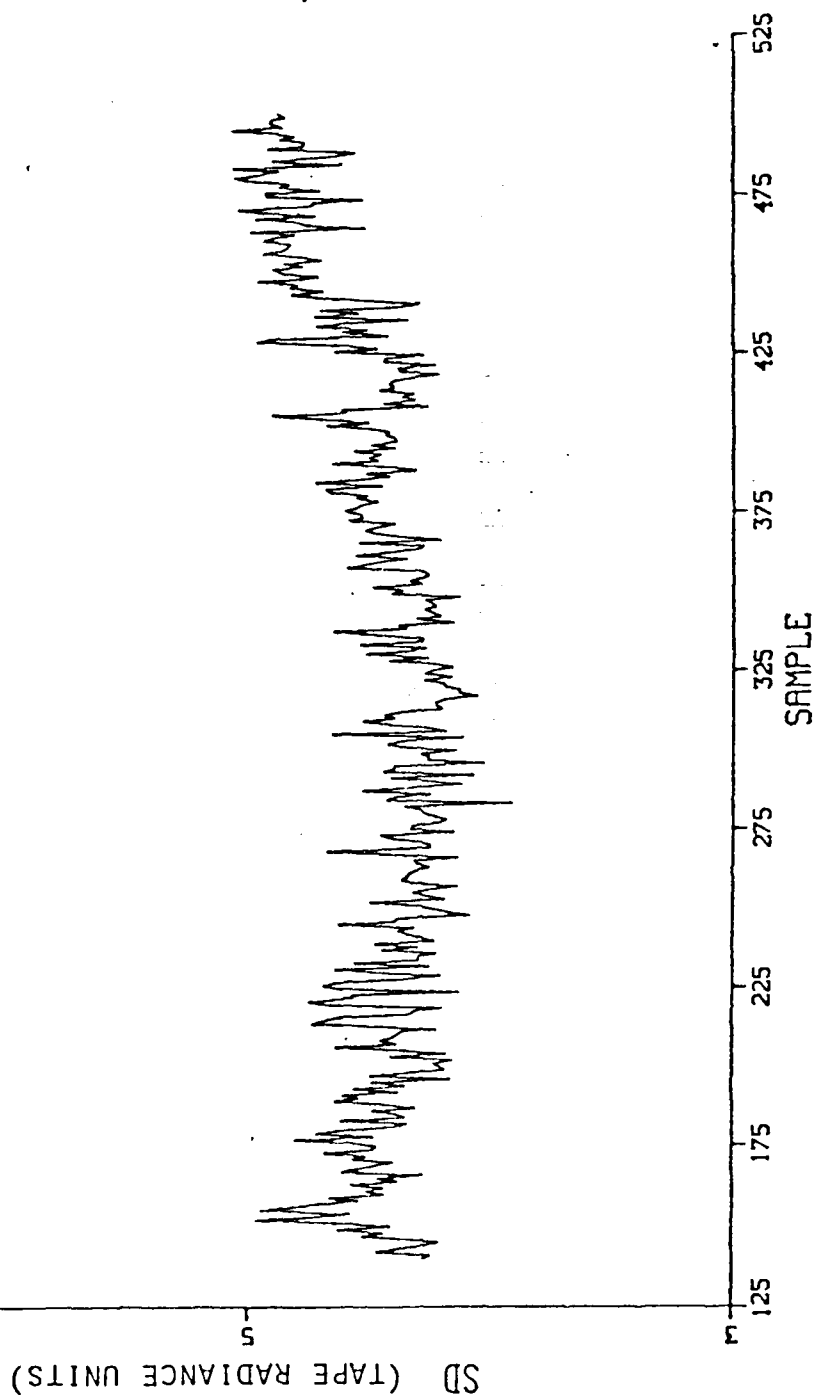


LONGWAVE BAR-SOURCE OUTPUTS WITH RESISTIVE-COUPPLING ARTIFACTS

FIGURE 9

1 TAPE RAD. UNIT = 1.000 X 10⁻⁶ W/M²·SR

EXTENDED SOURCE T = 50.0 °C

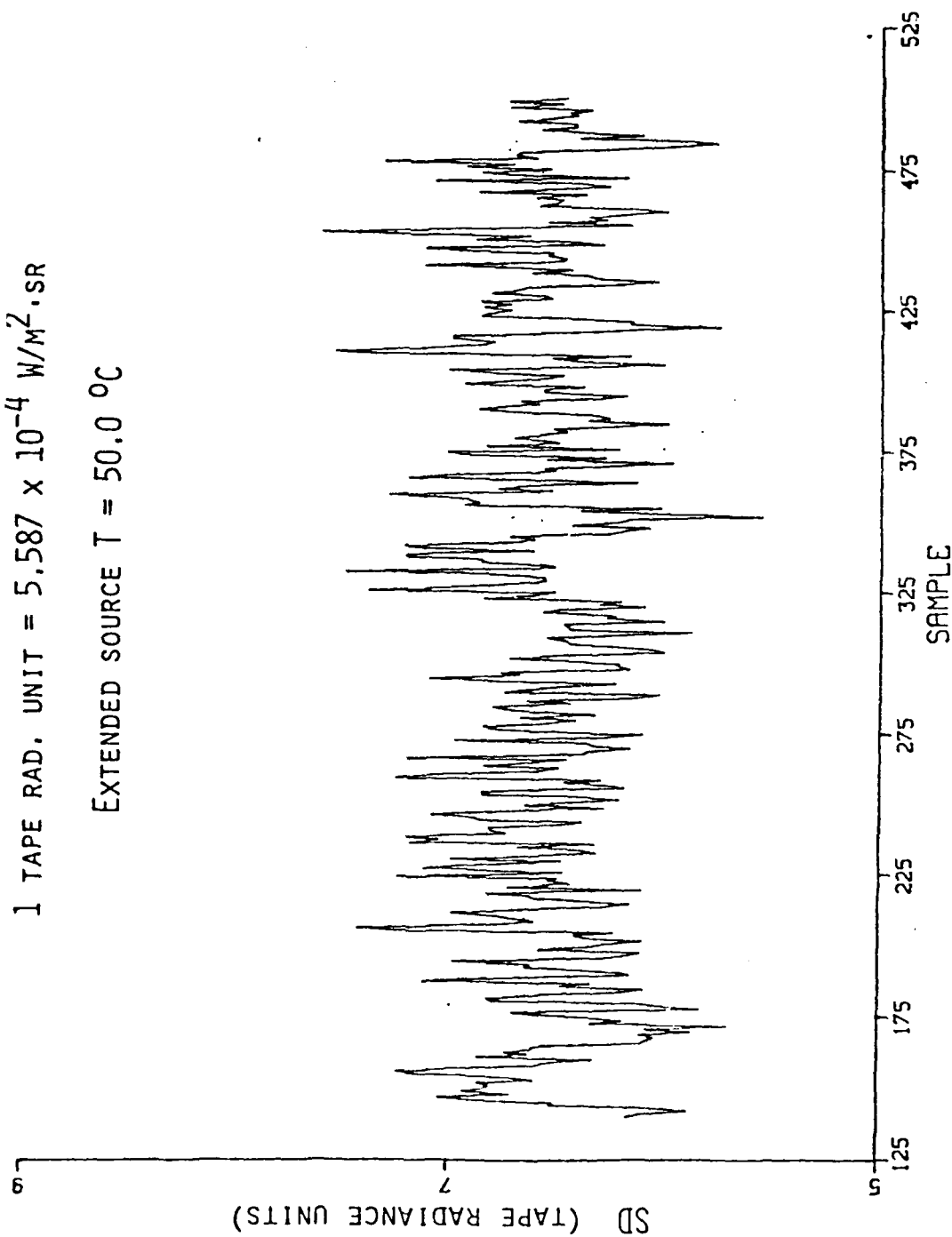


CROSS-CHANNEL STANDARD DEVIATIONS OF LONGWAVE RADIANCES

FIGURE 23

1 TAPE RAD. UNIT = $5.587 \times 10^{-4} \text{ W/M}^2 \cdot \text{SR}$

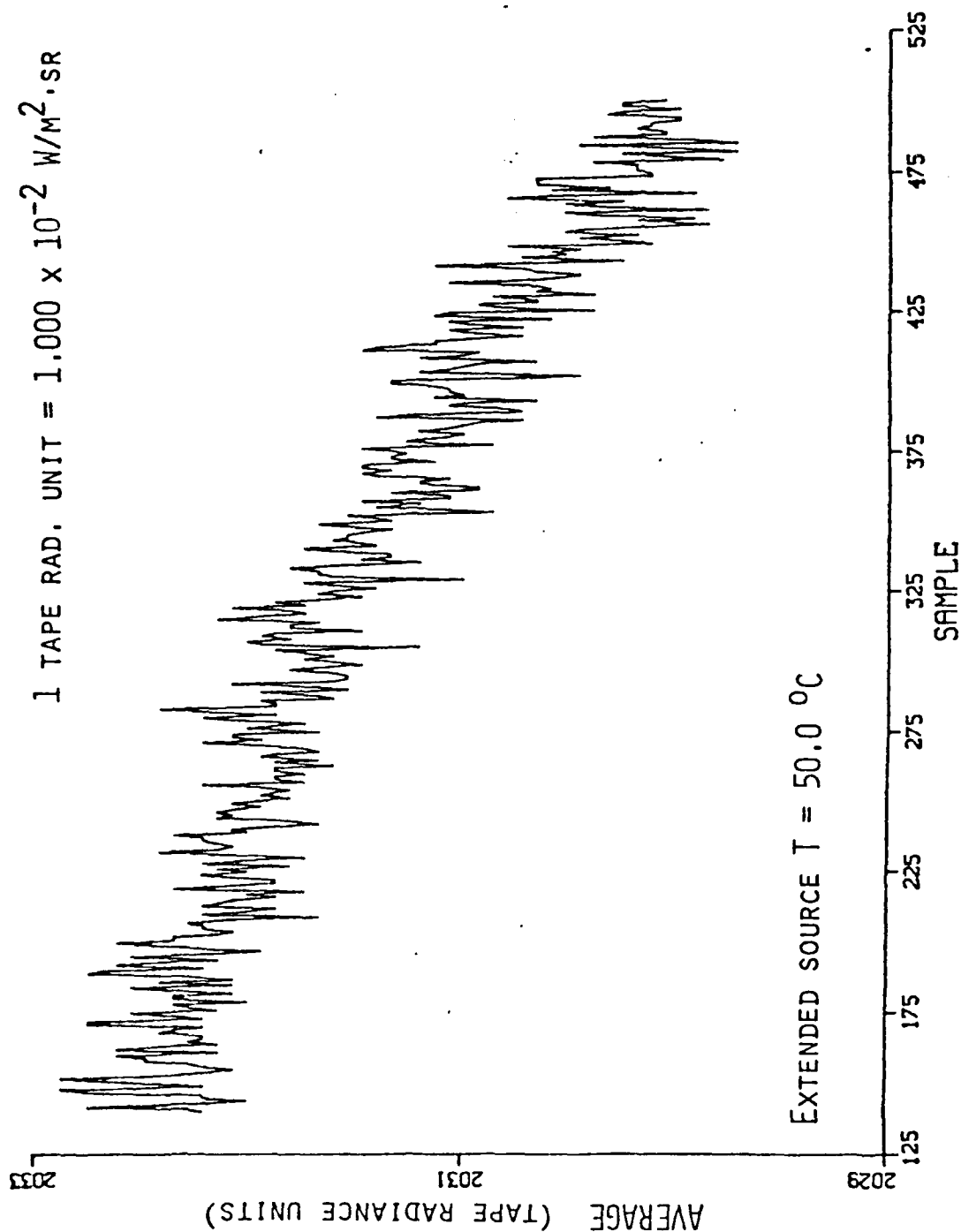
EXTENDED SOURCE $T = 50.0^\circ \text{C}$



CROSS-CHANNEL STANDARD DEVIATIONS OF MIDWAVE RADIANCES

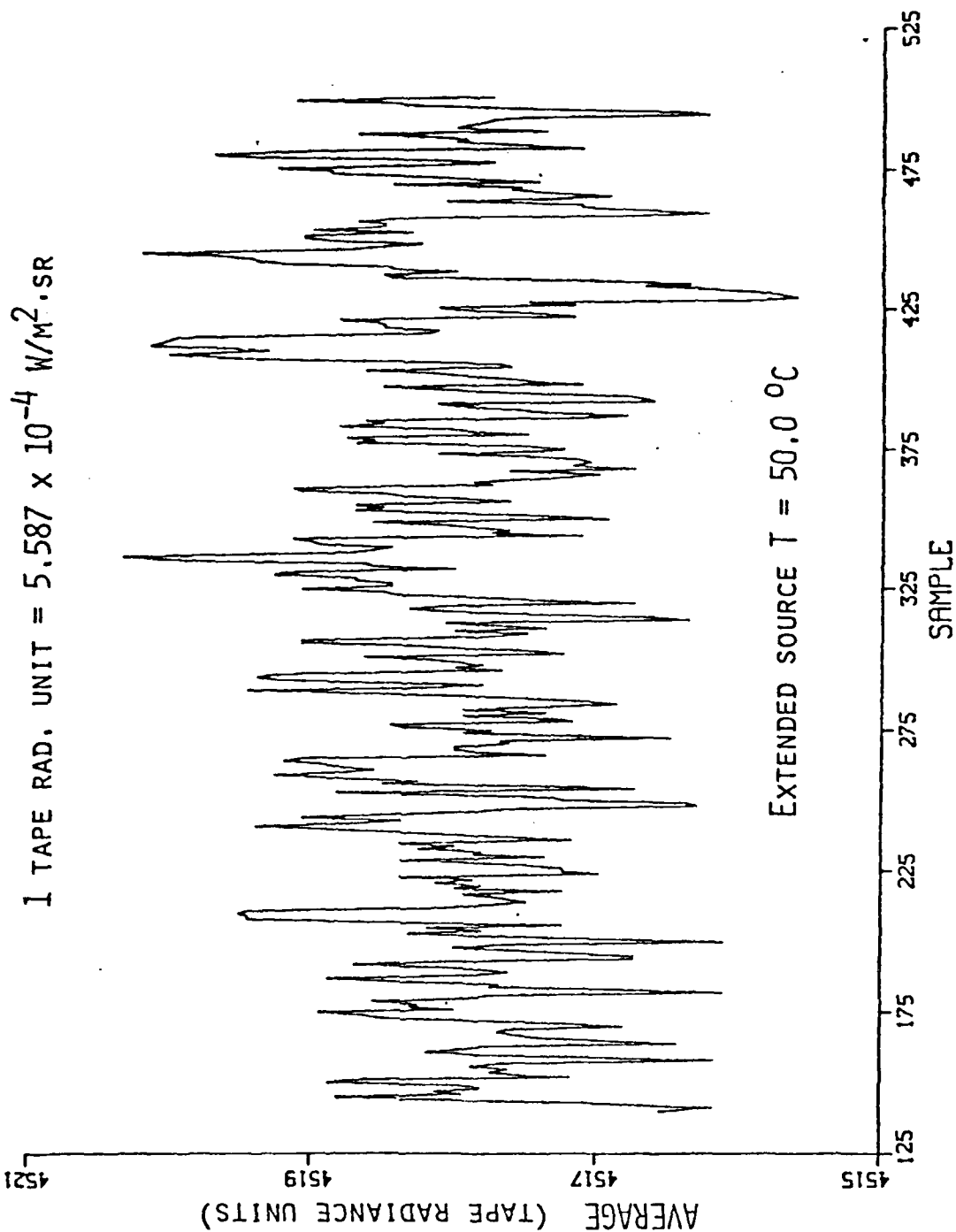
FIGURE 22

1 TAPE RAD. UNIT = $1.000 \times 10^{-2} \text{ W/M}^2 \cdot \text{SR}$



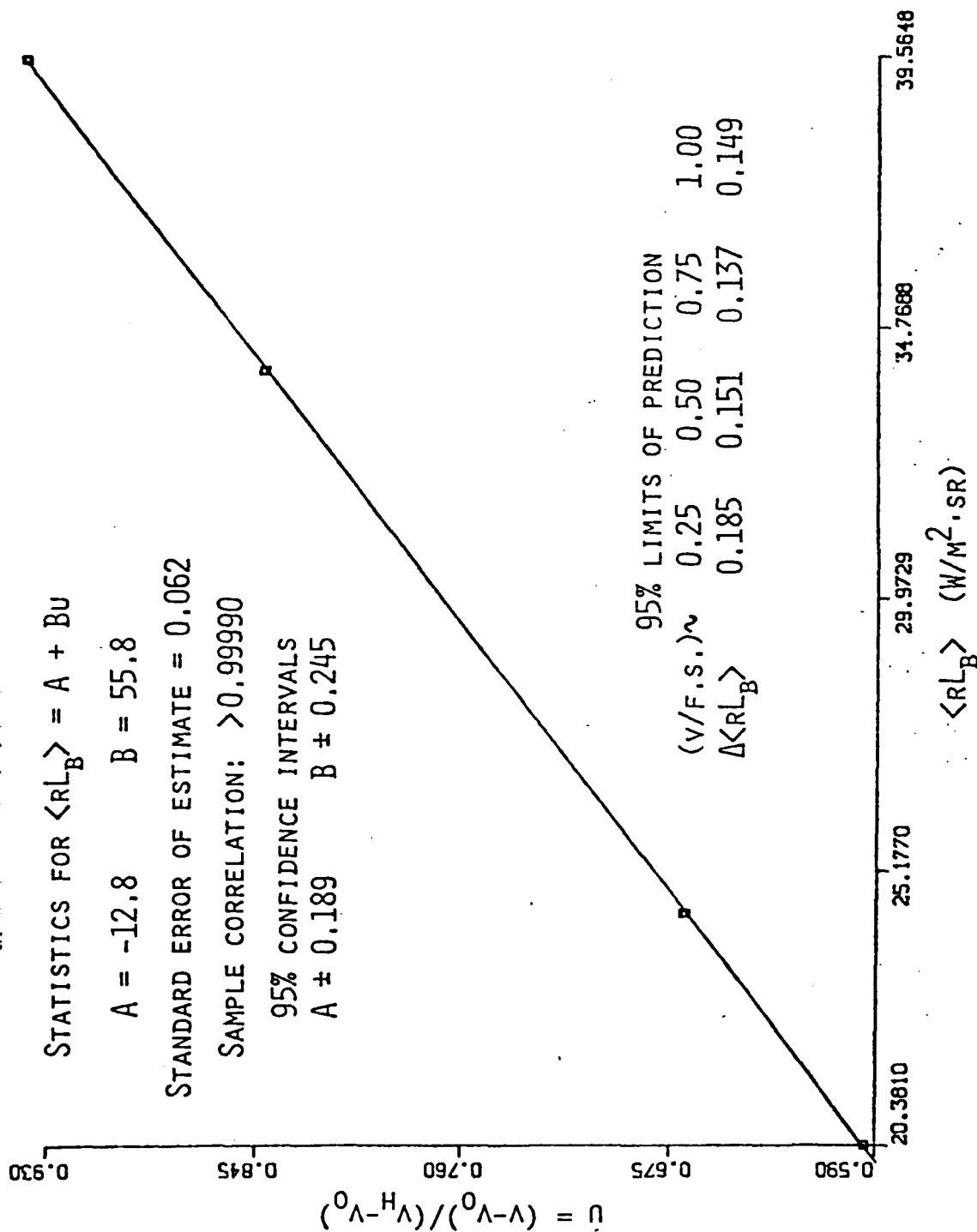
CROSS-CHANNEL AVERAGES OF LONGWAVE RADIANCES

FIGURE 21



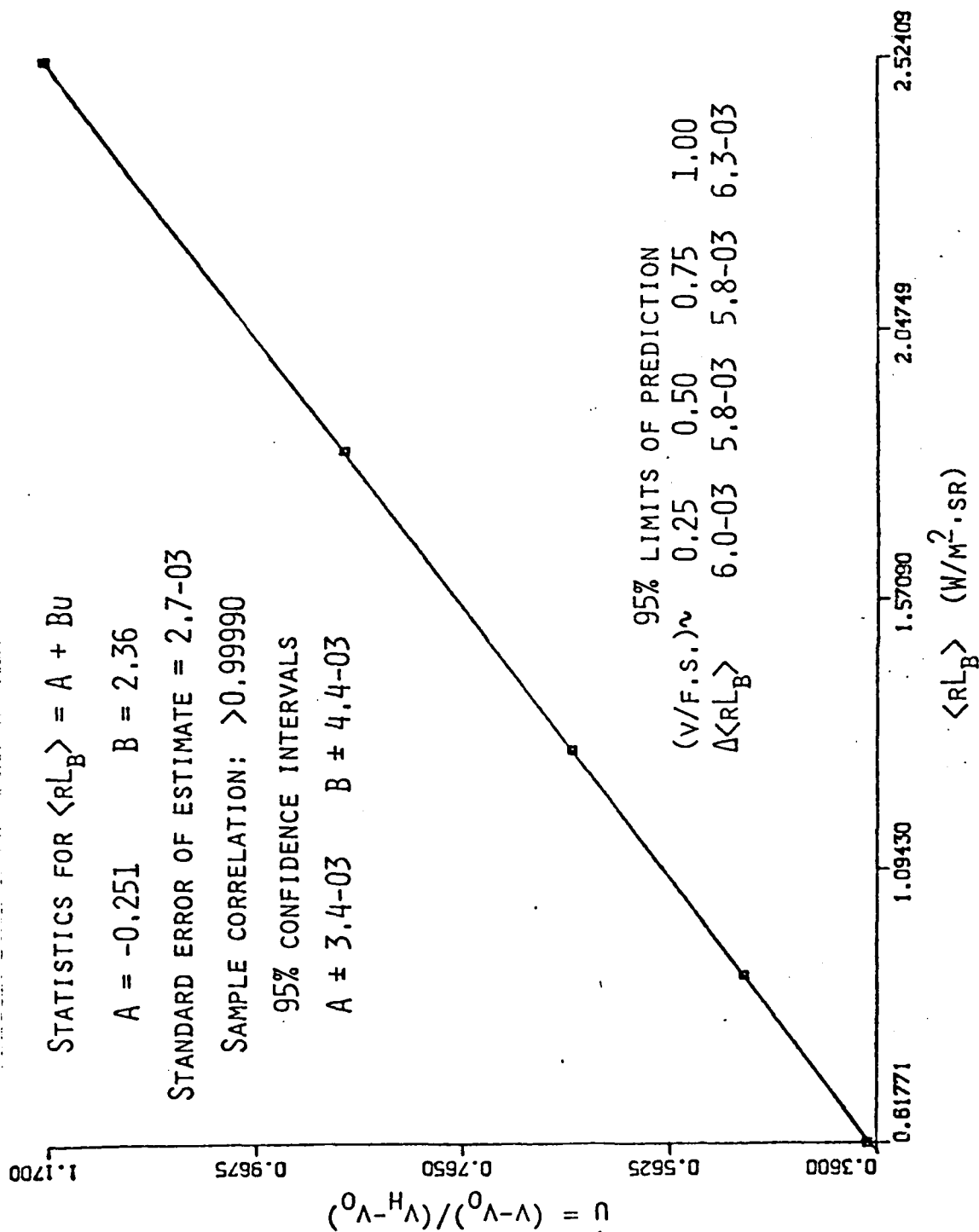
CROSS-CHANNEL AVERAGES OF MIDWAVE RADIANCES

FIGURE 20



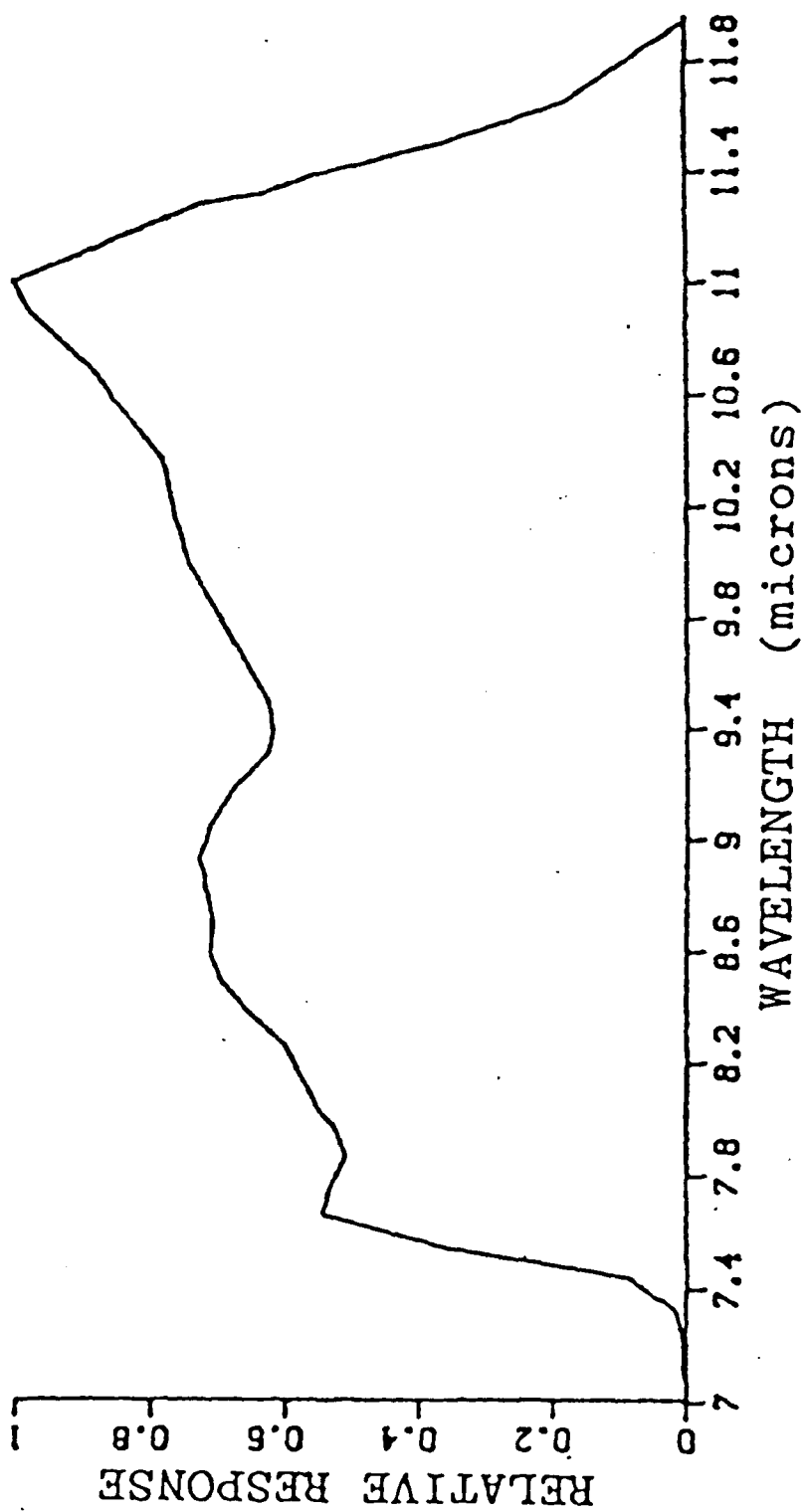
LONGWAVE CALIBRATION, CHANNEL 6, TAPE BF7

FIGURE 19



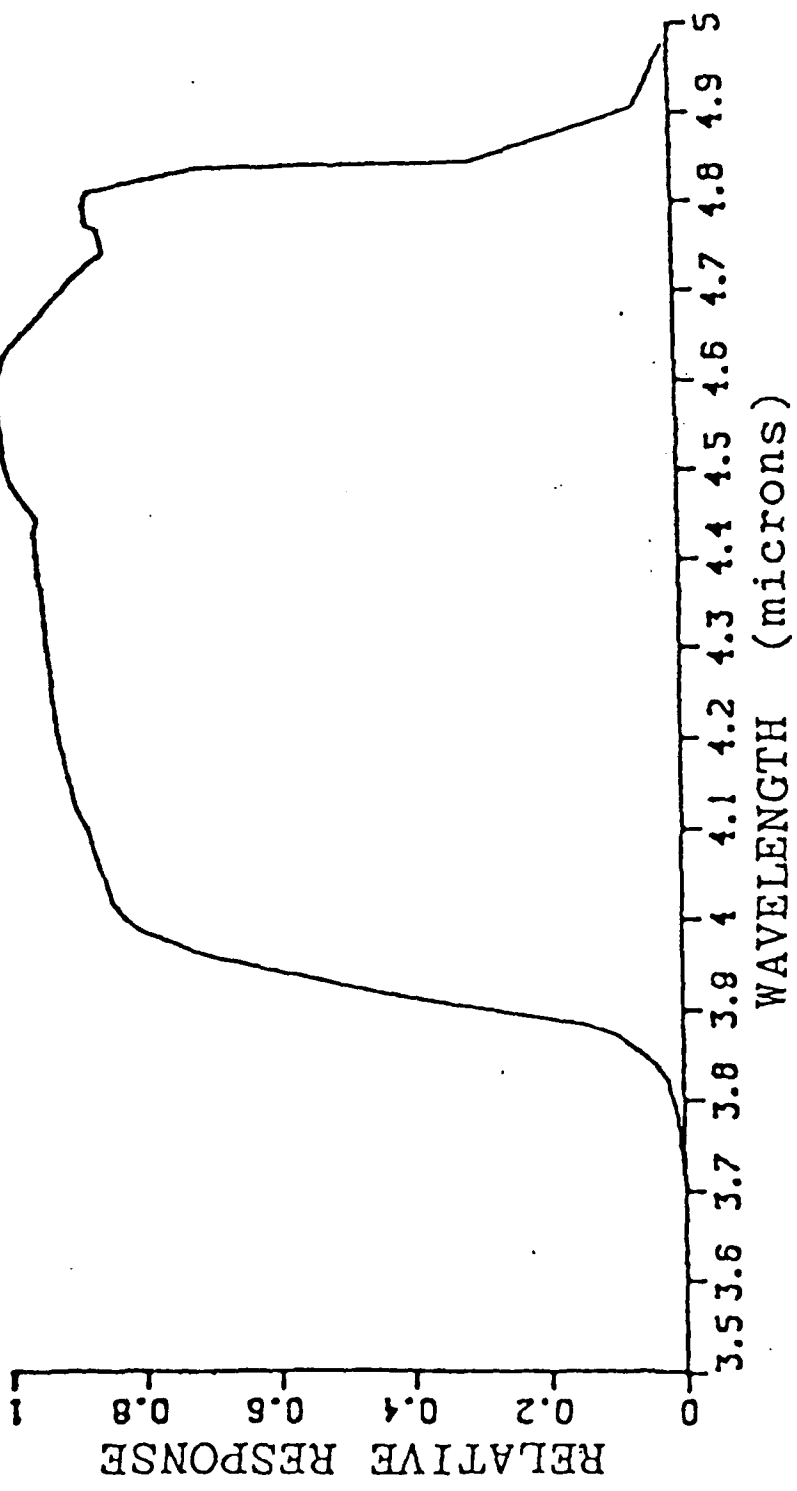
MIDWAVE CALIBRATION, CHANNEL 6, TAPE BF7

FIGURE 18



LONGWAVE RESPONSE FUNCTION FOR CALIBRATION

FIGURE 17



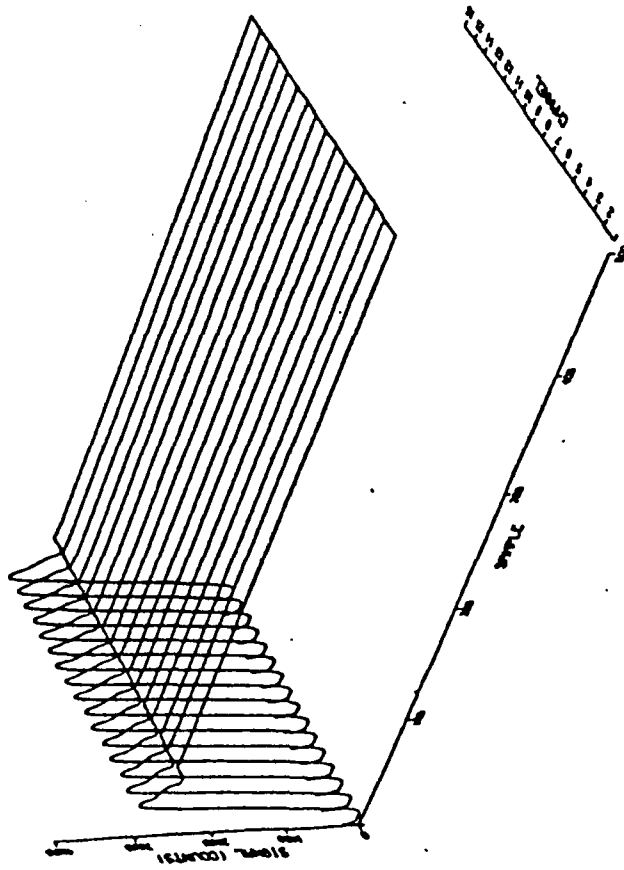
MIDWAVE RESPONSE FUNCTION FOR CALIBRATION

FIGURE 16

BEDFORD MA., 23 AUG 1984

TAPE : 1 , MODE : MW , FRAME : 189

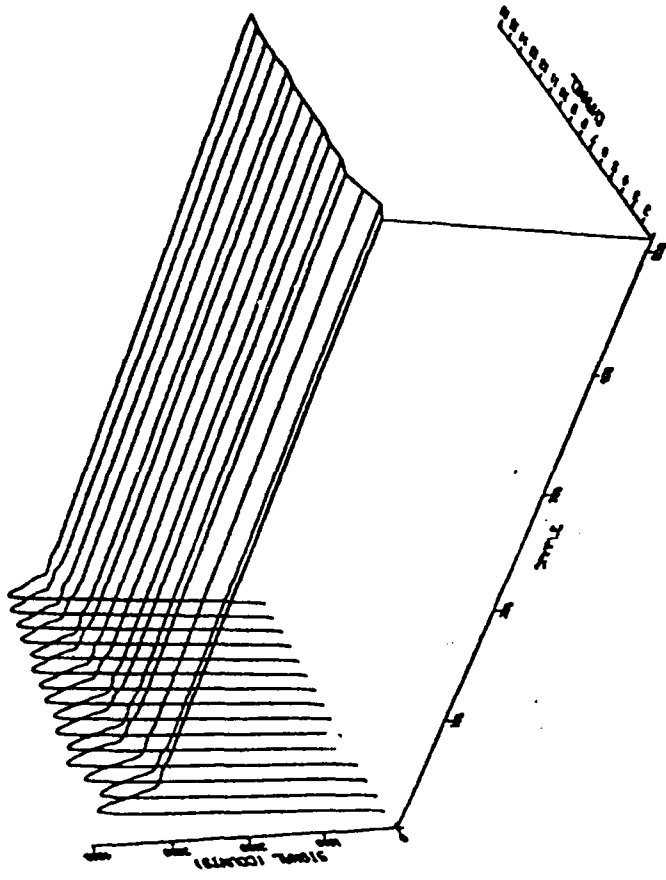
3 DAYS, 12 HOURS, 15 MIN, 1.3 SEC



BEDFORD MA., 23 AUG 1984

TAPE : 1 , MODE : LW , FRAME : 215

3 DAYS, 12 HOURS, 24 MIN, 40.8 SEC

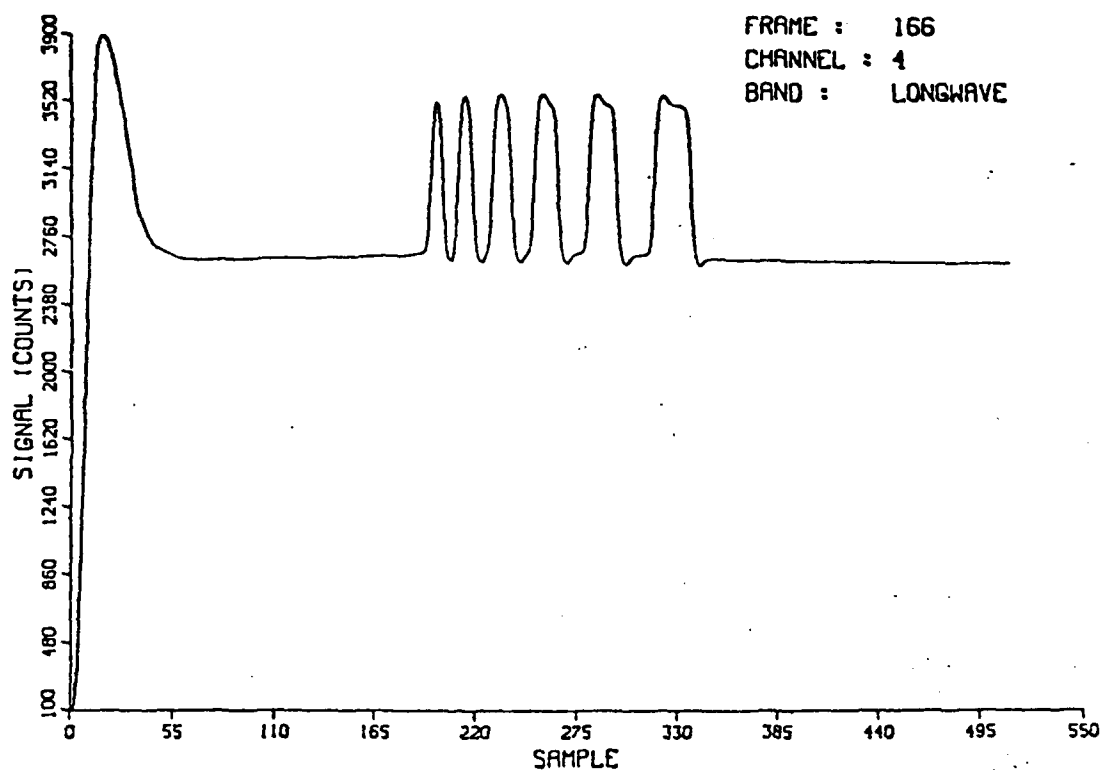


TYPICAL FRAMES OF RADIO-METRIC CALIBRATION DATA

FIGURE 15

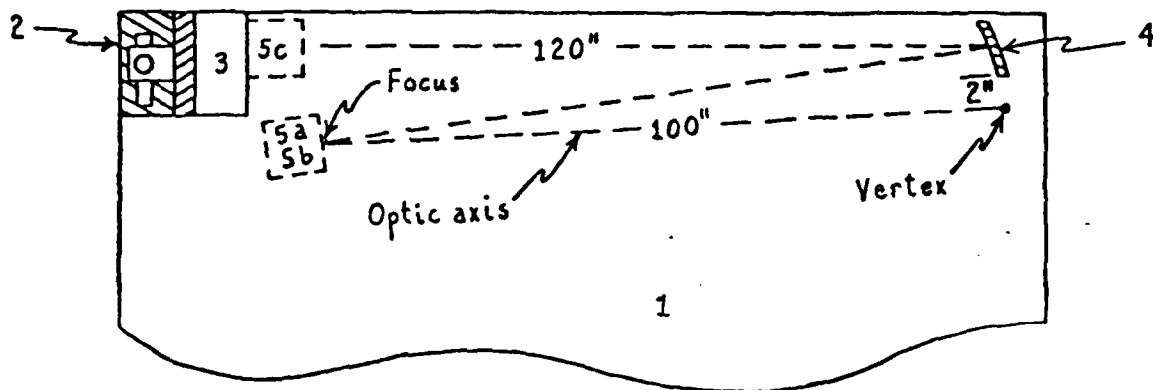
RADIOMETER T - 20.6C, BAR T - 50.0C, RAW DATA

3 DAYS 12 HRS 6 MIN 54.8 SEC



LONGWAVE OUTPUT FROM A MULTIPLE NARROW BAR SOURCE

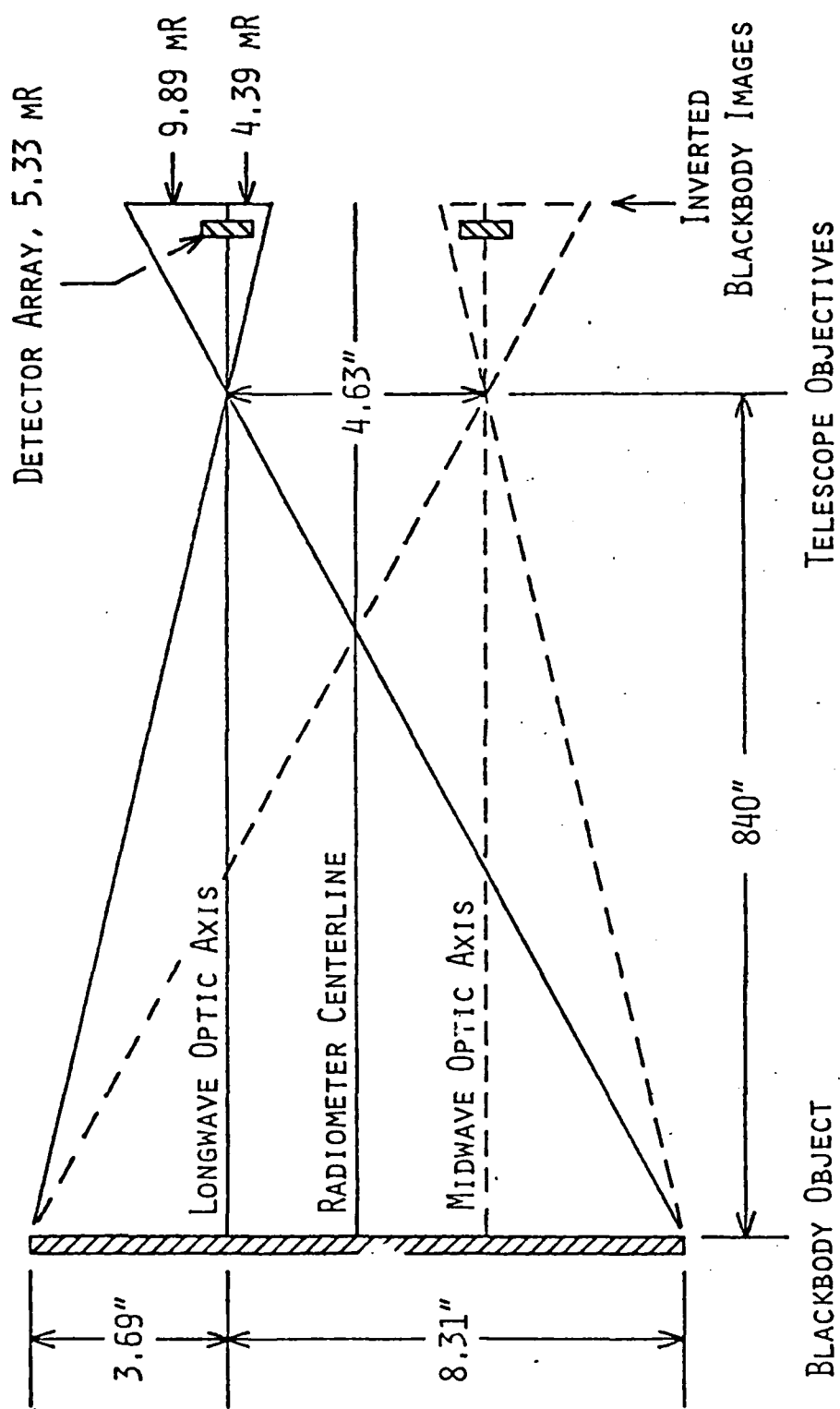
FIGURE 14



- | | |
|--|---|
| 1. Optical bench | 5. Blackbody source |
| 2. Movable stage,
horizontal & vertical
micrometer adjustments | a. EOI model HS 153,
4.7 mil aperture |
| 3. Radiometer | b. EOI model P1406S1
with 6 bar target |
| 4. Off-axis paraboloid,
10" dia., 100" f.l. | c. EOI model P1406S1
w/o 6 bar target |

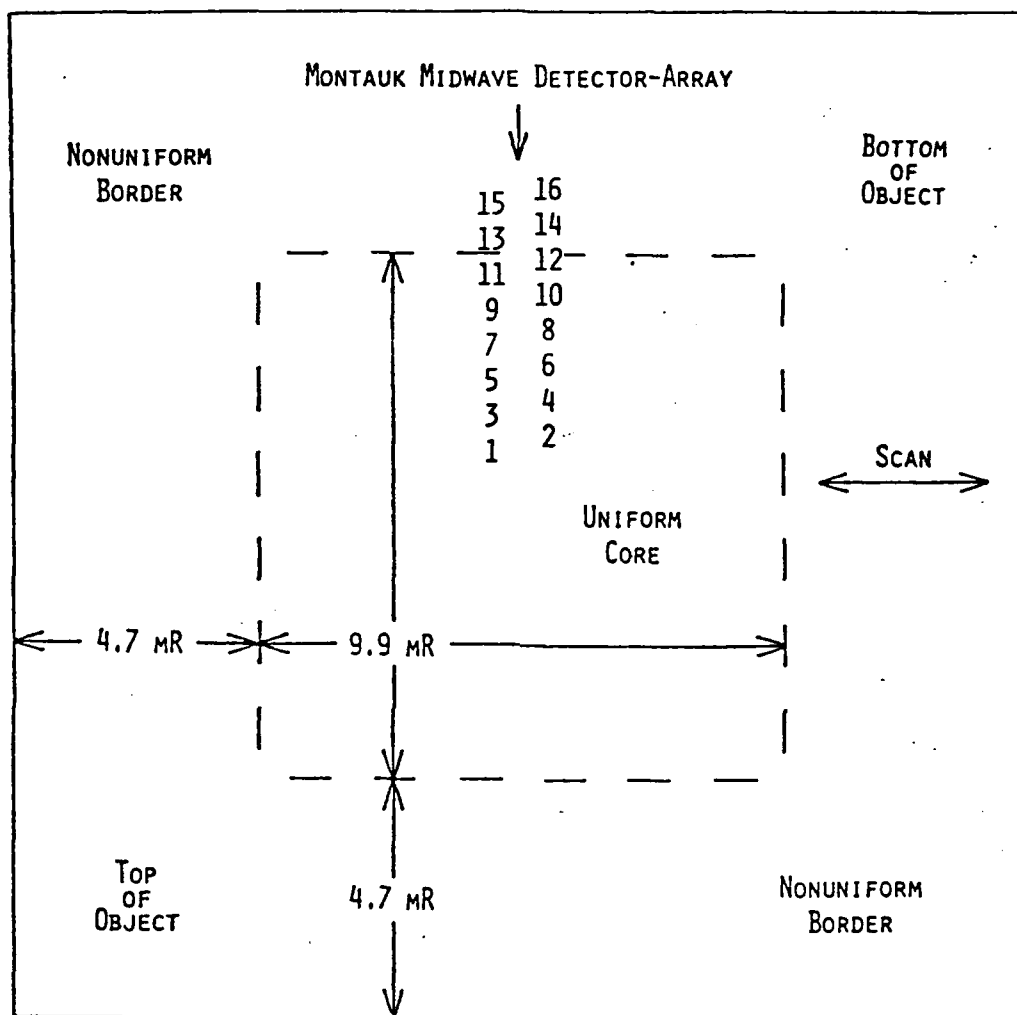
TOP VIEW OF LABORATORY CALIBRATION SETUP

FIGURE 13



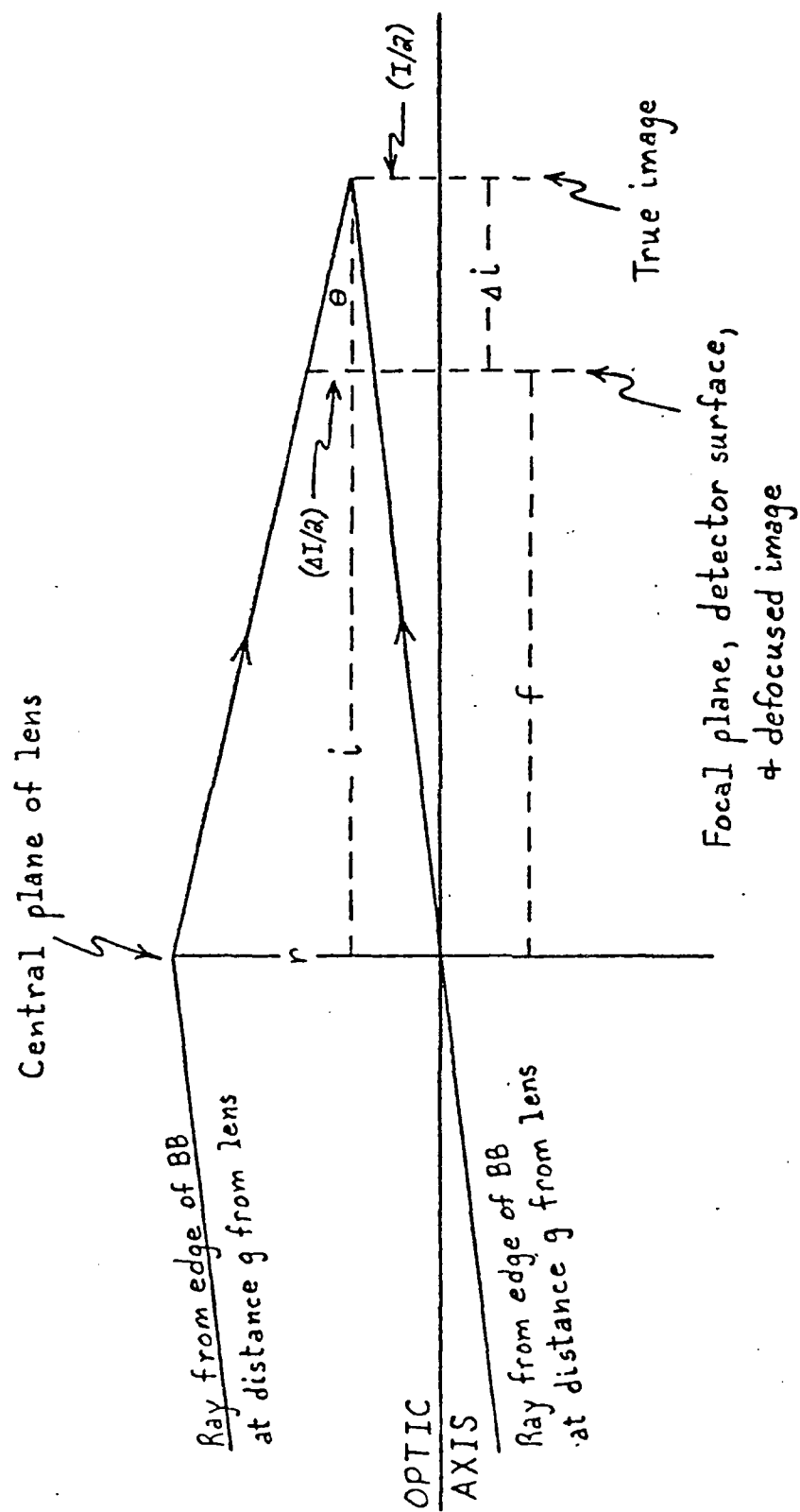
PARALLACTIC EFFECTS IN MONTAUK CALIBRATION SETUP

FIGURE 12



INVERTED, DEFOCUSED, PARALLACTIC, BLACKBODY IMAGE
CROSSING MIDWAVE DETECTOR AT MONTAUK POINT

FIGURE 11



BLACKBODY IMAGE FORMATION
DURING ATTEMPTED RADIOMETRIC CALIBRATION AT MONTAUK POINT

FIGURE 10

1.6 TABLES

1. System Parameters for Data Recording
2. Blackbody Calibration Options and BMAP Selection Criteria
3. Summary of Radiometer Log for Tape BF7
4. Summary of Radiometer Log for Tape BF8
5. Midwave Calibration Parameters and Statistics, Tape BF7
6. Longwave Calibration Parameters and Statistics, Tape BF7

TABLE 1: SYSTEM PARAMETERS FOR DATA RECORDING

Item	Midwave Spectral Band (3.8-5.0 μm)	Longwave Spectral Band (7.3-11.9 μm)
Telescope	4 inch diameter aperture 6 inch focal length	Same as midwave "
Detector array	InSb photovoltaic, 77°K 16 detectors in 2 columns of 8 ^a See Figure 1 for layout	HgCdTe photoconductive, 77°K Same as midwave ^b "
Field of view (mR)		
instantaneous	0.37 az. x 0.40 el. ^c	0.33 az. x 0.33 el.
total	49.09 az. x 5.40 el. ^d	49.09 az. x 5.33 el.
Spectral response	See Figure 16	See Figure 17
3dB electronic passband (Hz)	0 - 1000	0.3 - 1000 ^e
Point-source output	See Figure 2 for shape	Same as midwave
full width at half maximum	0.37 mR ^f	0.33 mR
Recorded random noise	2.5 mv	Same as midwave
NEI (W/cm^2)	2×10^{-14}	2×10^{-13}
Scan extent	7(5/8) ^g of scene	Same as midwave
data interval	2.8125°, 92.2 ms	"
period	0.5 s (time between data ints.)	"
rate during data interval	30.5°/s = 532 mR/s ^g	"
dwell time	0.695 ms ^h	0.620 ms ^h
Sampling time	<< dwell time	Same as midwave
interval	0.09606 mR	"
intervals/dwell	3.85 ⁱ	3.44
data interval	512 samples	Same as midwave
cold reference	10 samples ^j	"
cold & hot references	140 samples	"
usable scene data	370 samples	"
Digitization	0-10 v = 12 bits = 0-4096 decimal	Same as midwave

(a) Detectors 14 and 16 dead at Montauk Point

(b) Detector 1 dead

Values at Montauk Point: (c) 0.33 az. x 0.33 el., (d) 49.09 az. x 5.33 el., (e) 0.5 - 1000,
(f) 0.33 mR, (g) 36.0°/s = 628 mR/s, (h) 0.525 ms, (i) 3.44, (j) 23

+ : Advantage 0 : Neutral - : Disadvantage ? : Uncertain

Source Location and Size Selection Criteria	Distant		Near	
	Small	Large	Small	Large
Focus not required	-	-	+	+
Atmospheric attenuation	-	-	+	+
Stray background radiation	-	+	-	+
Aperture filled	+	+	-	+
Direct radiance responsivity	-	+	+	+
Source availability	+	?	?	+
Whole array illuminated	-	?	+	+
Ease of handling & control	-	-	0	+
Positioning not critical	0	0	-	+

BLACKBODY CALIBRATION OPTIONS AND BMAP SELECTION CRITERIA

TABLE 2

PLACE: Bedford, Massachusetts, USA
 42°28'42"N, 71°17'24"W, 250 ft. above mean sea level
 DATE: 13 September 1984

DIGITAL TAPE: BF7
 VIDEO TAPE: 45664302

SUMMARY OF RADIOMETER LOG

No.	Object Scanned Description	Local Time of Start	Record Mode*	Frame Nos.	Line of Sight [†]		Temperature(°C)		
					Azimuth	Elevat'n	Optics	IntBB	ExtBB
SCE33	Hole in cloud deck	08:52:21.3	A	001-061	108	12	25.2	37.4	----
SCE34	"	08:55:36.8	"	062-163	112	15	25.1	"	----
SCE35	"	08:58:39.8	"	164-285	109	19	"	"	----
SCE36	"	09:07:51.3	"	266-347	130	11	24.9	"	----
SCE37	"	09:11:47.8	8/8	348-389	113	09	24.2	"	----
SCE38	"	09:18:57.8	A	390-461	093	08	23.3	"	----
XBB9	External black body	09:24:42.3	MW	462-465	----	----	23.0	37.4	50.0
"	"	09:25:34.8	"	466-469	----	----	22.9	"	40.0
"	"	09:26:30.8	"	470-473	----	----	"	"	30.0
"	"	09:27:28.8	"	474-477	----	----	"	"	20.0
"	"	09:28:25.8	"	478-481	----	----	"	"	10.0
XBB9	External black body	09:29:31.8	LW	482-485	----	----	22.9	37.4	10.0
"	"	09:30:37.8	"	486-489	----	----	22.7	"	20.0
"	"	09:32:07.3	"	490-493	----	----	22.6	"	30.0
"	"	09:33:08.3	"	494-497	----	----	"	"	40.0
"	"	09:34:05.3	"	498-501	----	----	"	"	50.0
CC7	Closed cover	09:34:54.3	LW	502-505	----	----	22.6	37.4	----
"	"	09:35:51.3	MW	506-509	----	----	"	"	----
SCE39	Hole in cloud deck	09:38:33.3	8/8	510-551	120	14	22.6	37	----

*A = alternate midwave and longwave frames. MW or LW = midwave or longwave output only.
 8/8 = longwave outputs (5-12) in data channels (1-8) plus midwave outputs (5-12) in data channels (9-16).

[†]Azimuth in degrees clockwise from geographic N. Elevation in degrees above horizontal.
 IntBB, ExtBB = Internal, External Black Body

SUMMARY OF RADIOMETER LOG FOR TAPE BF7

TABLE 3

PLACE: Bedford, Massachusetts, USA
 42°28'42"N, 71°17'24"W, 250 ft. above mean sea level
 DATE: 13 September 1984

DIGITAL TAPE: BF8
 VIDEO TAPE: 45664302

SUMMARY OF RADIOMETER LOG

No.	Object Scanned Description	Local Time of Start	Record Mode*	Frame Nos.	Line of Sight [†]		Temperature(°C)		
					Azimuth	Elevat'n	Optics	IntBB	ExtBB
SCE40	Stratocumulus	15:36:55.3	A	001-059	233	33	29.6	37.7	----
SCE41	"	15:42:34.3	8/8	060-101	242	30	27.2	37.6	----
SCE42	"	15:46:15.8	"	102-143	253	19	27.3	"	----
SCE43	Thin, rapidly moving clouds	15:48:16.8	"	144-265	229	22	27.4	"	----
SCE44	Stratocumulus	15:58:11.8	"	266-307	275	24	27.8	"	----
SCE45	"	16:19:31.3	"	308-369	238	06	26.9	"	----
SCE46	"	16:21:31.3	"	370-411	248	08	26.6	"	----
XBB10	External black body	16:31:58.8	MW	412-415	---	---	26.4	37.6	50.0
"	"	16:33:11.8	"	416-419	---	---	"	"	40.0
"	"	16:34:30.3	"	420-423	---	---	26.5	"	30.0
"	"	16:35:24.3	"	424-427	---	---	"	"	20.0
"	"	16:36:41.3	"	428-431	---	---	26.4	"	10.0
XBB10	External black body	16:37:27.8	LW	432-435	---	---	"	"	10.0
"	"	16:38:43.3	"	436-439	---	---	26.3	"	20.0
"	"	16:39:54.8	"	440-443	---	---	"	"	30.0
"	"	16:41:03.8	"	444-447	---	---	26.2	"	40.0
"	"	16:42:05.8	"	448-451	---	---	"	"	50.0
CC8	Closed cover	16:44:50.3	LW	452-455	---	---	26.1	37.6	----
"	"	16:45:21.8	MW	456-459	---	---	"	"	----
SCE47	Stratocumulus	16:59:03.3	A	460-550	257	06	25.2	"	----

*A = alternate midwave and longwave frames. MW or LW = midwave or longwave output only.
 8/8 = longwave outputs (5-12) in data channels (1-8) plus midwave outputs (5-12) in data channels (9-16).

[†]Azimuth in degrees clockwise from geographic N. Elevation in degrees above horizontal.
 IntBB, ExtBB = Internal, External Black Body

SUMMARY OF RADIOMETER LOG FOR TAPE BF8

TABLE 4

CHANNEL	PARAMETERS		VARIANCE	95% CONFIDENCE INTERVALS	
	A	B		A	B
1	-0.195	2.23	3.591E-06	2.319E-03	2.927E-03
2	-0.201	2.27	3.812E-06	2.397E-03	3.060E-03
3	-0.232	2.30	5.194E-06	2.843E-03	3.620E-03
4	-0.231	2.32	3.720E-06	2.405E-03	3.095E-03
5	-0.258	2.35	3.237E-06	2.275E-03	2.920E-03
6	-0.251	2.36	7.109E-06	3.359E-03	4.361E-03
7	-0.268	2.38	1.205E-06	1.394E-03	1.805E-03
8	-0.256	2.38	4.916E-06	2.800E-03	3.651E-03
9	-0.276	2.41	5.141E-07	9.148E-04	1.197E-03
10	-0.267	2.43	5.771E-06	3.051E-03	4.037E-03
11	-0.273	2.42	5.943E-06	3.105E-03	4.081E-03
12	-0.250	2.39	4.965E-06	2.805E-03	3.688E-03
13	-0.263	2.40	4.407E-06	2.661E-03	3.487E-03
14	-0.244	2.39	4.624E-06	2.699E-03	3.557E-03
15	-0.251	2.39	4.152E-06	2.567E-03	3.367E-03
16	-0.227	2.37	5.707E-06	2.972E-03	3.920E-03

95% PREDICTION LIMITS

CHANNEL	U			
	0.300	0.630	0.960	1.30
1	4.271E-03	4.091E-03	4.134E-03	4.406E-03
2	4.399E-03	4.213E-03	4.265E-03	4.559E-03
3	5.145E-03	4.919E-03	4.978E-03	5.326E-03
4	4.351E-03	4.161E-03	4.218E-03	4.524E-03
5	4.066E-03	3.883E-03	3.934E-03	4.223E-03
6	6.019E-03	5.752E-03	5.839E-03	6.282E-03
7	2.480E-03	2.368E-03	2.403E-03	2.586E-03
8	5.004E-03	4.783E-03	4.859E-03	5.234E-03
9	1.620E-03	1.547E-03	1.572E-03	1.697E-03
10	5.421E-03	5.180E-03	5.275E-03	5.707E-03
11	5.505E-03	5.258E-03	5.349E-03	5.779E-03
12	5.025E-03	4.805E-03	4.888E-03	5.274E-03
13	4.739E-03	4.528E-03	4.604E-03	4.968E-03
14	4.847E-03	4.637E-03	4.718E-03	5.092E-03
15	4.596E-03	4.395E-03	4.469E-03	4.820E-03
16	5.379E-03	5.151E-03	5.241E-03	5.652E-03

CORRELATION: 1.00

MIDWAVE CALIBRATION PARAMETERS AND STATISTICS, TAPE BF7

TABLE 5

CHANNEL	PARAMETERS		VARIANCE	95% CONFIDENCE INTERVALS	
	A	B		A	B
2	-12.9	56.2	5.109E-03	0.218	0.284
3	-12.7	56.1	5.241E-03	0.220	0.287
4	-12.7	55.9	4.030E-03	0.193	0.251
5	-12.8	56.2	3.848E-03	0.189	0.246
6	-12.8	55.8	3.849E-03	0.189	0.245
7	-12.5	55.6	4.435E-03	0.201	0.262
8	-12.6	55.4	4.327E-03	0.199	0.257
9	-12.8	55.5	5.699E-03	0.230	0.296
10	-13.0	55.4	4.379E-03	0.202	0.259
11	-12.8	55.0	4.178E-03	0.197	0.251
12	-12.8	54.5	3.277E-03	0.174	0.220
13	-13.3	54.8	5.668E-03	0.232	0.291
14	-13.2	54.0	3.852E-03	0.191	0.237
15	-14.1	54.8	5.705E-03	0.237	0.292
16	-13.7	53.9	4.439E-03	0.207	0.254

95% PREDICTION LIMITS					
CHANNEL	0.250	0.500	0.750	1.00	
2	0.213	0.174	0.158	0.173	
3	0.216	0.176	0.160	0.175	
4	0.189	0.154	0.140	0.153	
5	0.185	0.151	0.137	0.150	
6	0.185	0.151	0.137	0.149	
7	0.198	0.162	0.147	0.160	
8	0.196	0.160	0.145	0.158	
9	0.226	0.184	0.167	0.181	
10	0.199	0.162	0.146	0.158	
11	0.194	0.158	0.143	0.154	
12	0.172	0.141	0.127	0.136	
13	0.228	0.186	0.167	0.178	
14	0.188	0.154	0.138	0.146	
15	0.231	0.188	0.168	0.177	
16	0.204	0.166	0.148	0.155	

CORRELATION: 1.00

LONGWAVE CALIBRATION PARAMETERS AND STATISTICS, TAPE BF7

TABLE 6

SYNCHRONOUS DEDICATED PROCEDURES

Activation

1. Power on equipment.
2. When connected, identify your terminal to the network by entering
D\$\$\$SON XXXXXX (enter your sign-on identification code for XXXXXX)
(Example: D\$\$\$SON AA1234) *D\$\$\$SON EK0115*
3. The system will respond with:

UNIVAC's Telcon Network-Level XXX DCPID=XXX
SESSION PATH OPEN
4. Identify your site to the DROLS system by transmitting the following:
DSGNONS/TERMINAL ID
(Example: DSGNONS/ABCDE) *DSGNONS/RTISO4*
5. The system will respond with:

*MSG ON1 SIGN-ON ACCEPTED
6. Enter your terminal ID as in the past. Entering of the terminal ID at this point will be eliminated in the near future.
7. DROLS commands remain the same.

Termination

1. Enter @TERM@ and transmit.
2. The system will respond with:

THIS TERMINAL HAS BEEN TERMINATED
*MSG DO7 PLEASE SIGN OFF TERMINAL
3. Disconnect (sign off) from the network by transmitting:

D\$\$\$SOFF
4. The system will respond with:

SESSION PATH CLOSED
5. Power off equipment.

TERMINAL USER CONDITION MESSAGE DESCRIPTION

TERMINAL MESSAGE	DESCRIPTION	USER ACTION
*MSG ON1 SIGN-ON ACCEPTED	DROLS System has validated the user and allowed access.	N/A
*MSG ON2 SIGN-ON REJECTED	DROLS System error.	Call On-Line Support Office
*MSG ON3 SIGN-ON REJECTED	Sign on error.	Check for data error If correct, call On-Line Support Office
*MSG ON4 SIGN-ON REJECTED	DROLS System error.	Call On-Line Support Office
*MSG ON5 SIGN-ON REJECTED	Terminal is already active.	Continue with DROLS
*MSG ON6 SIGN-ON REJECTED	Illegal Terminal ID used.	Check for data error If correct, call On-Line Support Office
*MSG ON7 SIGN-ON REJECTED	Terminal has been disabled.	Call On-Line Support Office
*MSG OF1 TERMINAL INACTIVE	DROLS System termination error.	Call On-Line Support Office
*MSG DI1 USER TERMINATED	DROLS System error.	Call On-Line Support Office
*MSG DI2 USER TERMINATED	DROLS System error.	Call On-Line Support Office

TERMINAL USER CONDITION MESSAGE DESCRIPTION

TERMINAL MESSAGE	DESCRIPTION	USER ACTION
*MSG D13 USER TERMINATED	DROLS System error.	Call On-Line Support Office
*MSG D14 WAIT-LAST INPUT IGNORED	Terminal is in output mode.	Wait for data to return
*MSG D01 USER TERMINATED	DROLS System error.	Call On-Line Support Office
*MSG D02 USER TERMINATED	DROLS System error.	Call On-Line Support Office
*M D03 USER TERMINATED	DROLS System terminating all users.	Standby for Broadcast or call Voice Recorder
*M D04 USER TERMINATED	DROLS System terminating this user.	Call On-Line Support Office
*MSG D05 CANNOT INITIALIZE SITE	DROLS System will not allow this site to activate.	Call On-Line Support Office
*MSG D06 USER TERMINATED	DROLS System error.	Call On-Line Support Office
*MSG D07 PLEASE SIGN OFF TERMINAL	Normal termination request.	N/A
*MSG D08 USER TERMINATED	DROLS System error.	Call On-Line Support Office.
*MSG D09 USER TERMINATED	DROLS System error.	Call On-Line Support Office

end 301

Part 2

PART 2

SIMULATION OF MID-INFRARED CLUTTER REJECTION.

2: THRESHOLD-SENSOR-SIZE EFFECTS WITH LMS-FILTERED NOISE.

Published in Applied Optics, 15 February 1985

by

M. S. Longmire, F. D. Bryant, J. D. Wilkey, and A. F. Milton

04 30 079

Abstract

The relation between an adaptive threshold sensor's size and its performance is analyzed numerically using LMS-filtered noise. The analysis links signal detection to size through the threshold parameter, sampling variance, and a clutter-edge effect. A principle is established for determining by statistical analysis of natural background data whether a 2-D threshold sensor may be advantageous. It is not under the conditions of this simulation. Critical, optimum, and best sizes are given for a 1-D threshold sensor following a 1-D LMS filter with input from an optical sensor having NEI (noise equivalent irradiance) = $1.5 \times 10^{-13} \text{ W/cm}^2$ and spatial resolution $0.15 \times 0.36 \text{ mR}$ (milliradians).

I. Introduction

Wide-field infrared (IR) surveillance sets must detect signals against backgrounds with uniformly radiant parts (often clear sky) and cluttered parts of variable radiance (often sunlit clouds). Techniques for detecting signals in uniform-sky noise are well developed, but those for detecting signals in clutter noise - or simply rejecting clutter to avoid false alarms - are not. This state of affairs exists chiefly because theoretical analysis using a simple noise model gives the optimum method of detecting signals in uniform sky, but not in clutter. With clutter an alternative approach is to compare signal processing options using a computer, recorded natural background noise, and programmed algorithms to simulate the processing. This approach identifies the best option without requiring each to be tested in a surveillance set. Simulation does not give theoretically optimum solutions, but that is not perforce a disadvantage. For example, the theoretically optimum method of detecting point-source signals in clear sky fails altogether in clutter and has, therefore, limited value for wide-field IR surveillance. In this case a compromise between performance in clear sky and clutter may be more useful than optimum performance in either. A possible compromise was studied and several signal processing options were compared in the article preceding this one.¹

Both articles explore clutter rejection and signal detection by electronic filters and threshold sensors operating on the output of a

mid-IR (4.0-4.8 μ m) optical sensor scanned over clear sky and clouds with very bright, backlit edges. Detailed descriptions of the data, the algorithms and the method of simulation appear in the previous article.¹ (An appendix abstracting those descriptions is provided here at the request of the editor and reviewers to make this article reasonably self-contained.) The previous article compared the performance of two threshold sensors - one fixed, the other adaptive - following several one-dimensional (1-D) linear filters. The combination of a 1-D adaptive threshold sensor and a 1-D LMS spatial filter was found to suppress extreme cloud clutter effectively and to detect simulated signals almost as well in clutter as in clear sky. This combination merits further study, since the performance of an adaptive threshold sensor depends on its size - its spatial extent or the number of data used to estimate the local noise statistics - but only one size was studied in the previous article. Here we report the results of further work to determine how changing the size of a 1-D threshold sensor following a 1-D LMS filter affects signal detection.

The relation between an adaptive threshold sensor's size and its performance has already been investigated theoretically, e.g., see references 2-7. Most of this work has dealt with processing of radar or sonar signals, but the principles apply also to processing of infrared signals. The theory is not directly applicable to real cases, however, because it must employ low fidelity clutter models and other simplifying assumptions to render the problem

false alarm permitted in all the data always occurs in the clutter.

Except for a clutter-edge effect discussed below, the threshold parameters vary with frame size as the sampling s.d.s do. This means that there are certain critical sample sizes beyond which the threshold parameter and signal detection improve very slowly. The critical sample size depends on the fractional rate of decrease of the sampling s.d., which is obtained by differentiating equation (2).

$$\left[\frac{1}{(\sigma_{\hat{\eta}}/\sigma)} \right] \left[\frac{d(\sigma_{\hat{\eta}}/\sigma)}{dN} \right] = \frac{\alpha}{2N} \quad (3)$$

If ξ is the fractional rate of decrease at the critical sample size N_c , then $N_c = \alpha/2\xi$. From Figs. 4A and 4B the critical sample size in uniform sky appears to be about 100 uncorrelated noise values (250 data), which agrees with the theoretical result for a radar set operating in a constant noise environment, reference 2, p. 421. This gives $\xi \approx -1.8 \times 10^{-3}$ per datum or roughly -10^{-2} per uncorrelated noise value. Owing to the clutter-edge effect, it is difficult to estimate the critical sample size in clutter from Fig. 4. However, if ξ has the same value in clutter as in uniform sky, then $N_c \approx 150$ data (6 mR) in clutter, which agrees well enough with the appearance of the curves in Fig. 4. The critical sample size is always greater in uniform sky than in clutter, provided ξ is the same in the two regions, because $|\alpha|$ is always greater in uniform sky than in clutter.

B. Threshold Parameter, Critical Sample Size, and Clutter-edge Effect

The sampling s.d.s of the uniform sky and clutter populations of Figs. 3E and 3F are replotted against frame size in Fig. 4A. Obviously in both cases the sampling s.d. decreases at a decreasing rate with increasing frame size. This is not surprising; the law of diminishing returns with increasing sample size is well known. More important is the relation between the sampling s.d. and the threshold parameter.

To study this relation we first calculated threshold parameter ratios $x_w / \langle |x_f| \rangle$ from the two data sets (each containing 114 segments) used in the previous article,¹ not from the restricted sets of Figs. 3E and 3F. (The frame sizes employed were $2n = 36, 80, 144, 240$, and 340 data, the limit of 340 being necessary to prevent excessive loss of ratios. A pair of data added to the frame reduces the number of ratios calculable from a segment by two. The smallest of the 228 segments each contained 1486 data. A frame size of 340 data is 23 percent of a smallest segment, which means that 23 percent of the data in those segments could not be used as window values x_w . If larger frame sizes had been used, the results would be unreliable because of the additional ratios lost.) Next we arranged the ratios in statistical frequency tables from which we determined threshold parameters that allow one false alarm (f.a.) in all the data or one in the uniform sky; these parameters are plotted in Fig. 4B. The one

stationary noise. If the noise is correlated and non-stationary, δ is determined by these two properties jointly, and a numerical analysis would require calculations with synthetic noise having a known type and amount of non-stationarity. The effort did not seem worthwhile. In this case we simply regard equation (2) as an empirical relation useful for interpreting and predicting the effects of changing threshold-sensor size.

This treatment of non-stationarity needs clarification, lest it seem flawed. Non-stationary noise has no definite mean absolute deviation, so the sampling variance of that statistic cannot approach zero and may not decrease monotonically with increasing sample size. True, for an infinite data set, but real data sets are finite. A finite data set does have a definite mean absolute deviation whose value is obtained without error when the sample includes all data of the set. An infinite, non-stationary data set is equivalent to an infinite ensemble of finite data sets, each having different statistics. One always works with a few members of the ensemble at most. Conclusions thus reached will be useful if the data fairly represent the conditions the surveillance set encounters.

$$\log(\sigma_{\hat{\eta}}/\sigma) = \beta + \alpha \log(\sqrt{N}). \quad (2)$$

The line through the uniform-sky results is adequately fit by $\alpha = -0.909$ and $\beta = 0.0819$, that through the clutter results by $\alpha = -0.530$ and $\beta = -0.0433$.

The fact that $\alpha > -1$ for the uniform-sky results requires comment. The uniform-sky noise may not be strictly stationary because small gain differences ($< 8\%$) between segments were not corrected. (Neither were they corrected for the simulations here or in the previous article.¹) On the other hand, non-stationarity between segments should increase the ranges of the sampling s.d.s primarily, whereas non-stationarity within the segments should be the chief cause of increases in the slopes. The small differences between -1 and α for the uniform-sky results may, therefore, be due to ordinary experimental uncertainty like that in Figs. 3A and 3B, not to gain differences.

If the noise is stationary, β can be related to the fraction f of the data which are effectively independent. The lines through the sampling s.d.s of the correlated Gaussian noise have $\alpha = -1$ and $\beta = 0.188$. From the latter we find $f = 0.42$. Calculations of product-moment correlation coefficients show that the first and last of five sequential magnitudes in the LMS-filtered synthetic noise are uncorrelated, giving $f = 0.40$. The theoretical correlation length of LMS-filtered white noise¹³ gives $f = 0.5$ approximately. Clearly the suggested interpretation of β is sound for correlated

to obtain Gaussian noise with the same correlation as the LMS-filtered uniform-sky noise. The correlated synthetic noise was then processed in the same way as the uncorrelated noise; results are plotted in Figs. 3C and 3D. Correlation and non-random sampling together reduce the number of independent values in the frame, so that the values and, usually, the ranges of the sampling s.d.s are increased. For reasons already given the sampling s.d.s at a frame size of eight data are closer to the diagonals than those at larger frame sizes, which alone are of practical importance. At the larger frame sizes correlation and non-random sampling simply shift the reference line rightward parallel to itself, as illustrated by the lines with slope -1 drawn through the points at frame sizes above eight data.

Finally, sampling variances were calculated for ten segments of uniform-sky noise (each 1900 values long) and ten of clutter (each 3200 values long). Comparing these results - Figs. 3E and 3F - with those for correlated synthetic noise, we see that non-random sampling and non-stationarity increase the ranges of the sampling s.d.s and the slopes of the lines through them, most obviously in the case of the clutter. The sampling s.d.s of both the uniform-sky noise and the LMS-filtered clutter can be described empirically at the frame sizes of interest simply by extending equation (1) to include the effects of non-random sampling, correlation, and non-stationarity. The general equation for any line in Fig. 3 is

correlated and non-stationary. (Correlation is measured in this work by the product-moment correlation coefficient.¹¹) To relate the theorem to the problem in hand, we made computations in which we first approximated the conditions of the theorem and then relaxed them by steps to arrive at the actual conditions.

Nine segments of uncorrelated, Gaussian, pseudo random noise were generated by the method described in reference 12. This was done for two segment lengths, 1900 and 3200 values, which are the average lengths of the segments of recorded uniform-sky noise and clutter used in the previous article.¹ Sampling variances were calculated by passing the segments through the adaptive threshold algorithm using ten frame sizes from 8 to 640 values. The results appear in Figs. 3A and 3B, where the dots indicate the sampling s.d.s of the whole data set, and the bars span the ranges of the sampling s.d.s of the segments. (The variances are calculated about $\eta = \langle |x| \rangle$, the average absolute deviation of all data in a set. Consequently, a population sampling variance is the average of the associated segment sampling variances.) The sampling s.d.s for the population are on or very near the diagonals showing that sampling by an adaptive threshold sensor is equivalent to random sampling if the noise is stationary and uncorrelated. The ranges of the sampling s.d.s for the segments result from chance differences between the segments. They are larger for the shorter segments as expected.

Next the synthetic noise was passed through the 1-D LMS filter

A. Numerical Analysis of Sampling

Since dispersion is measured by the mean absolute deviation, the sensor's sampling performance can be related to the theorem on the sampling distribution of the mean, which states in part:¹⁰ If random samples of $2n = N$ values each are taken from a population (data set) of more than $20N$ values, the relation between the population variance σ^2 and the sampling s.d. $\sigma_{\hat{\eta}}$ of the mean is closely approximated by

$$\sigma_{\hat{\eta}}^2 = \sigma^2/N \quad \text{or} \quad \log(\sigma_{\hat{\eta}}/\sigma) = -\log(\sqrt{N}). \quad (1)$$

The sampled population consists of the absolute deviations $|x - \mu|$, which are the noise magnitudes $|x|$ since the LMS-filtered data have zero means locally and globally.

The logarithmic form of equation (1) is represented by the diagonals in Fig. 2. The sampling s.d. is divided by the population s.d. to facilitate comparison of results from data sets with different variances. It is useful to think of a one-sided threshold sensor and consider the limit of equation (1) when $N = 1$. In that case $\hat{\eta} = |x_f|$ so that $\sigma_{\hat{\eta}} = \sigma$ by definition, and the equation is an identity. Thus, we expect equation (1) to be nearly satisfied when the sample size is small, regardless of other conditions. Except for $N = 1$, however, the theorem is not applicable to the adaptive threshold sensor and the recorded background noise because the sensor does not take random samples, and the recorded noise is

increasing frame size, but the threshold parameter may decrease or increase, and signal detection may improve or deteriorate depending on other factors. To transform this qualitative description into a semi-quantitative one, we analyzed the threshold sensor's sampling performance, related that to the threshold parameter required for a given false alarm rate, and finally linked the threshold parameter to signal detection.

the sensor of Fig. 1 cannot operate statistically; its behavior in that case is described in the appendix.

(Here a digression is necessary to explain an important detail. With uniform-sky noise, which is stationary, the local values η_1 of the mean absolute deviation are the same as its global value η_g . The frame averages $\hat{\eta}$ estimate both η_1 and η_g . The variance of $\hat{\eta}$ about η_g is due only to chance differences between samples. With a finite set of non-stationary clutter data, the local values η_1 differ from the global value $\eta_g = \langle |x| \rangle$ for the whole data set. The frame averages $\hat{\eta}$ still estimate both η_1 and η_g , and chance differences between samples still contribute to the variance of $\hat{\eta}$ about η_g , but the variance is increased by the non-stationarity.)

This summary of the adaptive threshold sensor's operation implies certain effects which occur as the frame size is increased. When the frame is small some estimates of $\eta = \langle |x| \rangle$ are much too small, others much too great. Large $\hat{\eta}$ degrade signal detection locally by causing the local threshold $K\hat{\eta}$ to be larger than necessary to prevent a false alarm. Small $\hat{\eta}$ degrade signal detection globally since the threshold parameter, $K = \text{limit of } (x_w/\hat{\eta})$, is the same throughout the scene and must be large to prevent a false alarm where $\hat{\eta}$ is small. As the frame size is increased the estimates of η become more accurate, the sampling variance and the threshold parameter decrease, and signal detection improves, provided the noise is stationary. If the noise is non-stationary the sampling variance may still decrease with

shows cloud-edge clutter at the outputs of the LMS filter and the wideband filter used for data collection. In this work the optical sensor is the one used for data collection, but the wideband filter is virtually eliminated by passing the data through the LMS filter to obtain a low value of $\langle |x| \rangle$ throughout the scene. (This is permissible because the LMS passband lies well within that of the wideband filter.) With the optical sensor and electronic filter specified, the quality of signal-detection depends mainly on the value of K required for the designated false alarm rate.

The mean μ of the filtered noise determines the mode of the sensor's operation as follows: If the mean is always zero over the sensor's reach ("locally"), it is also zero over all greater extents ("globally"). The mean of uniform-sky noise is zero locally and globally, as is the mean of LMS-filtered clutter (Fig. 2B). In such cases the mean magnitude $\langle |x| \rangle$ and mean absolute deviation $\langle |x - \mu| \rangle$ are identical and are estimated locally and globally by the frame averages $\hat{\eta} = \langle |x_f| \rangle$. The estimate $\hat{\eta}$ and the local threshold $(\mu + K\hat{\eta}) = K\hat{\eta}$ vary as the filter output passes through the sensor. The distribution and variance of $\hat{\eta}$ about $\eta = \langle |x| \rangle$ are known as the sampling distribution and sampling variance; the standard deviation (s.d.) is known as the standard error of the mean,⁹ but we shall call it the sampling s.d.. With noise whose mean is zero locally and globally, the sensor of Fig. 1 operates "statistically", i.e., sets the threshold at $T = (\mu + K\hat{\eta})$ and makes a statistical test of the window value's signal content. If the noise mean is not zero locally,

Because of difficulties in estimating the local probability distribution and its parameters, no adaptive threshold sensor operates ideally. The simpler, practical, 1-D sensor studied here is represented in Fig. 1 with discrete values of the filter output passing stepwise through it. At each step this sensor averages the magnitudes of $2n$ values which lie equally about the single value x_w whose signal content is to be tested. The local threshold is a constant multiple K of the average $\langle |x_f| \rangle$. The part of the sensor containing the tested value will be called the signal window, and the part containing the $2n$ averaged magnitudes will be called the frame. The part called the shutter blocks values from the wings of a point-source signal centered on the window and prevents them from affecting the threshold. Since the threshold parameter K is constant, the false alarm probability varies with the local probability distribution as well as at clutter edges. Nonetheless, K can be made large enough to provide any desired false alarm rate in the whole scene.

The mean magnitude $\langle |x| \rangle$ of the filtered noise determines the quality of this sensor's operation. The lower the average threshold $K\langle |x| \rangle$, the better the signal detection is on average. Ordinarily $\langle |x| \rangle$ affects signal detection more than K because noise magnitude can vary as much as 20 dB with different optical sensors and electronic filters; the range of the threshold parameter is smaller unless there is an extreme clutter-edge effect. Differences in noise magnitude with different filters are illustrated in Fig. 2 which

II. Results and Discussion

An adaptive threshold sensor rejects noise and detects signals through a statistical test of the null hypothesis, filter output = noise, and the alternative, filter output = (signal + noise). Ideally the sensor does this by: taking a sample of N values from the local noise; estimating the local mean, dispersion, and probability distribution from the sample; setting a threshold ϵ from the estimates; taking a sample of one value x_w from the local noise not previously sampled; rejecting the null hypothesis if $x_w > \epsilon$. A threshold crossing is either a signal or a false rejection of the null hypothesis (false alarm).⁸ Further discriminants are needed to distinguish the two under operating conditions, but not in a simulation because it is known whether a simulated signal was added to the background data. The dispersion is usually measured by the standard deviation σ or the mean absolute deviation η . The local threshold is the sum of the local mean μ and a multiple of the local dispersion, e.g., $\epsilon = (\mu + k\eta)$. The multiple is chosen to provide a desired probability of false alarm and so depends on the local probability distribution. Nevertheless, the false alarm probability will vary at the "clutter edges" described in section II(B),⁶ and these can occur if either the distribution or its parameters alone vary. Thus, constant false alarm probability is unattainable in a cluttered scene even with a statistically ideal adaptive threshold sensor.

LMS-filtered noise. This leads to some useful experimental generalizations and to a principle for determining by data analysis whether a 2-D threshold sensor may be advantageous. The methods employed are applicable wherever recorded background data are available and should be useful for developing threshold sensors to operate under conditions different from the ones in this simulation.

mathematically tractable. Our simulation incorporates the theoretical ideas but is applicable to real cases because recorded natural background noise is used instead of clutter models and no simplifying assumptions need be made - the algorithms can be programmed to operate on the noise data as the filter and threshold sensor would operate on the sampled output of the optical sensor. (For convenience the sensor algorithm actually was simplified by ignoring off-peak detection of signals. The resulting error is negligible, as determined by computation. See the last paragraph of section II(C) for details.)

Because recorded background noise and exact algorithms are used, the simulation provides inputs, intermediate quantities, and outputs of the simulated devices under actual operating conditions. By studying the properties and interrelations of the inputs, intermediates, and outputs while varying the device parameters, one gains both insight into the operation of the devices and quantitative design information. In this connection, it should be noted that the simulations of this article and the previous one¹ emphasize statistical analysis of the data at all stages; they do not simply mimic device behavior. In fact, a major purpose of this work is to develop techniques of simulation which incorporate statistical analysis for design purposes, and to demonstrate the value of these techniques by example. With that in mind, we present a numerical study of the threshold sensor's sampling performance, taking account of non-random sampling, correlation, and non-stationarity of the

The plot of sampling s.d. in clutter suggests that the threshold parameter for one false alarm in clutter should decrease slowly beyond $N_c = 150$ data. In fact, it passes through a broad, shallow minimum because of the following clutter-edge effect, which appears to begin at a frame size between 8 and 10 mR (200 and 250 data). As the size of the threshold sensor is increased, the frame includes larger and larger proportions of the benign clutter which flanks severe clutter like that from 158 to 165 mR in Fig. 2B. This lowers the estimates $\hat{\eta} = \langle |x_f| \rangle$ and raises the ratios $x_w/\hat{\eta}$ in the vicinity of the severe clutter, thus increasing the threshold parameter needed to prevent a false alarm. Ordinarily the increase will be no more than a few decibels; only an extreme clutter-edge effect like the hypothetical one described in section V(B) of the previous article¹ could change the threshold parameter by 10-20 dB. Partly for this reason, the threshold sensor usually affects signal detection less than the optical sensor and electronic filter, as noted earlier. Here the increase of the threshold parameter - 2.3% between frame sizes of 240 and 340 data - is within the experimental uncertainty. However, the occurrence of a clutter-edge effect fits so well into the pattern of the results that we do not doubt its actuality. With that granted the dashed part of the top curve in Fig. 4B indicates how the threshold parameter might behave at larger frame sizes.

To verify or refute this behavior would require computations with unsegmented data. Many frame size effects can be studied

without separating uniform-sky noise from clutter, and if the data were not segmented, much larger frame sizes could be used before the loss of window values mentioned above became a problem. This would be advantageous for frame size studies, but would hide differences between performance in uniform sky and clutter. We chose to emphasize the latter, realizing that frame size studies with separated data are valid provided the clutter segments do not begin or end at clutter edges, a condition satisfied here.

(The clutter-edge effect has also been called the cloud-edge effect, but bright cloud edges may not be its only cause. The term, clutter-edge, is preferable since it accurately describes the origin of the effect in the waveform but is noncommittal about its origin in the scene.)

C. Signal Detection, Optimum Sample Size, and Best Sample Size

Frequencies of detecting simulated signals were calculated using the threshold parameters in Fig. 4B and the two data sets of 114 segments each from uniform sky and from clutter. The computed values are frequencies of detecting simulated signals at their peaks. There is an additional small chance for signals missed at their peaks to be detected elsewhere on the waveform. Ignoring off-peak detection causes $< 2.5\%$ error in detection frequencies ≥ 0.5 , as determined by calculation. Specifically, if the frequency of detection at the peak is 0.5000, the actual detection frequency including off-peak detection is < 0.5125 . Frequency of off-peak detection decreases with increasing frequency of detection at the peak, since only one detection of a signal is independent and, therefore, off-peak threshold crossings are not counted when the signal is detected at its peak. If off-peak detection is ignored, the adaptive threshold algorithm is much simpler and faster, yet the resulting error is negligible. Accordingly, this approximation was used here and in the previous work.¹

Frequencies of detection at the peak are plotted in Fig. 5 except those for the frame size of 144 data, which are in the previous article¹ and are hardly distinguishable from the results for the frame size of 340 data. From these curves we obtained data for Fig. 6, where simulated signal strengths required for detection frequencies of 0.50, 0.70, 0.90, and 0.95 are plotted against frame

size. The ordinates of curves in Fig. 6 will be called equally detected signal strengths.

The curves of equally detected signal strengths are much like the top threshold parameter curve in Fig. 4B, indicating that threshold-sensor size influences signal detection chiefly through its effect on the threshold parameter. The minima of the curves occur, regardless of detection frequency, at a frame size of about 10 mR (250 data), the same as the minimum of the threshold parameter curve. This is the optimum sample size for signal detection. Increasing the frame size to 14 or 15 mR increases equally detected signal strengths about 0.2 dB, the same as the causative increase of the threshold parameter. Because of the scales employed in Fig. 6, signal detection appears to deteriorate quickly below the optimum size, but actually it does not. Using frames of 144 or 36 data rather than the optimum size reduces signal detection by only 0.2 dB and 2.4 dB respectively. Thus, the best sample size here is the critical sample size in clutter since use of a larger frame risks a clutter-edge effect but improves signal detection very little in either clear sky or clutter. The frame must not be too much less than the optimum size, however, because the curves in Figs. 4B and 6 are rising rapidly at 36 data, one-seventh the optimum size.

D. Reality of the Simulation and Limitations of the Results

These subjects are discussed at length in the previous article (sections I, V(B), VI and appendix A),¹ but it may be worthwhile to re-emphasize two points here.

The first concerns the "reality" of the simulation. There are two realities, that of the signal processing and that of the scene and signal sources. As regards signal processing, the simulation and reality are alike since the algorithms effectively operate on the noise data as the simulated devices would operate on the output of the optical sensor. However, the relation of simulated signals to sources in the scene departs from reality. The simulated signals should correspond to sources of constant radiance placed at each sampled position of the scene, with account taken of the background covered by the sources (reference 1, appendix A). That was impossible in this work because the data could not be radiometrically calibrated. Consequently, the simulated signals used here correspond to real sources of constant "excess radiance" placed at each sampled position of the scene. ("Excess radiance" is radiance above that of the background covered by the source, all radiances being measured at the source plane.) In clear sky where the background radiance is uniform, signals from the two types of sources are the same, but they are different in clutter where the background radiance varies. To recapitulate, the simulated signals added to the uniform-sky noise and to the clutter correspond, respectively, to real sources of

constant radiance and to real sources of constant excess radiance. For that reason, the two types of simulated signals are called, respectively, signals and pseudo signals. Use of pseudo signals makes the computed frequencies of detection too large in clutter, i.e., the detection frequencies in Fig. 5B actually require larger signal strengths than those shown. Thus the simulated performance is better in clutter than the actual performance by an unknown and, with the given data, an unknowable amount. This should not significantly affect comparison of signal processing options, however, because all options are tested against simulated signals with the same connection to real sources.

The second point for re-emphasis concerns limitations of the results. Since this simulation is a form of data analysis, the results are restricted by the data employed, specifically, by all the natural and man-made conditions existing when the data were collected. Relative to the present simulation the most important experimental conditions are: (Natural) time and place of measurements, meteorologic conditions, type and range of clouds; (Man-made) line of sight, optical resolution, spectral passband, dwell time of the point-source image on the detector, point-source output of the detector, electronic passband and dynamic range, NEI, sampling rate, and sampling time. Section II of the previous article¹ and the appendix to this article give all available information about these conditions; any such information not found in either place is not available.

Despite restrictions imposed by experimental conditions, data analysis often leads to inferences of more general validity, and that is true here. In the next section, the more general and the more restricted results are clearly disjoined, and conditions for the validity of each are plainly stated. The conditions are inseparable from the results and conclusions; the latter must not be read, recalled, or used without the former.

III. Summary and Conclusions

We first summarize results and state conclusions which are valid in general for the type of adaptive threshold sensor in Fig. 1, when it follows a spatial filter whose mean output is zero over extents \geq the sensor's reach. Barring an extreme clutter-edge effect, the quality of signal detection depends primarily on the average magnitude of the filtered noise (set by the optical sensor and electronic filter) and secondarily on the threshold parameter. The threshold parameter required for a given false alarm rate is determined by the threshold sensor's sampling variance and by a clutter-edge effect. Ordinarily these factors change the threshold parameter and signal detection no more than a few decibels within the range of practical threshold sensor sizes. Only an extreme clutter-edge effect could result in changes greater than 10 dB. Sampling variance decreases at a decreasing rate with increasing threshold-sensor (sample) size. The decrease is more rapid when the noise is stationary than when it is non-stationary. There are loosely delimited critical sample sizes above which sampling variance decreases very slowly. The critical sample size for stationary noise is about 100 independent data at both radar and IR wavelengths. The critical sample size is larger for clear-sky (stationary) noise than for clutter (non-stationary) noise. If the scene is uncluttered, the threshold parameter and equally detected signal strength behave as the sampling variance does. If the scene is cluttered, they behave

likewise, provided there is no clutter-edge effect. If there is one, the threshold parameter for a given false alarm rate in the whole scene passes through a minimum with increasing sensor size, causing equally detected signal strength to do the same in both the clear and cluttered parts of the scene, as in Figs. 4B and 6.

The critical sample size is as large as the adaptive threshold sensor of Fig. 1 need be, since making it larger hardly improves performance. On the other hand, the sensor cannot be larger than the onset of a clutter-edge effect without loss of performance. Thus if a clutter-edge effect occurs, it may be impossible to expand the sensor enough in the scan direction to reach the critical sample size in clear sky or even in clutter. With a column of detectors normal to the scan, however, sampling in two directions is possible. This allows the sample size to be increased without expanding the sensor's length, albeit at the risk of clutter-edge effects in all directions within the field of view. The question then is whether 1-D and 2-D sensors perform equally or whether one type is better.

The following principle will be useful for investigating that question: If the onset of a clutter-edge effect with a 1-D sensor is less than the critical sample size in either clutter or clear sky, a 2-D sensor may be (but is not guaranteed to be) advantageous, otherwise it will not be. Note that if a 1-D sensor fails to achieve the critical sample size in clutter, a 2-D sensor may do so, and thus be advantageous, even if it too fails to reach the critical sample size in clear sky. The intended use of this principle is evaluation

of threshold sensor performance by statistical analysis of background data. To apply the principle, one must know the critical sample sizes and the onset of the clutter-edge effect. The critical sample sizes can be estimated from the sampling variance, the threshold parameter, or signal detection. The sampling variance gives the least accurate estimates but is by far the easiest method to use. The clutter-edge effect and its onset can be found only from the threshold parameter or signal detection. The principle is limited to cases where the sensor makes a statistical test for signals, i.e., cases where the noise mean is zero over extents \geq the sensor's reach. This requires the filter preceding the sensor to have a high cut-on frequency. The principle is not applicable with a low-pass filter or a bandpass filter having a low cut-on frequency. The clutter outputs of these filters simply cause the sensor to turn off the surveillance set, as explained in the appendix.

(Some hypothetical cases can be described to exemplify the principle. If a 1-D and a 2-D sensor both achieve the critical sample size in clear sky without a clutter-edge effect, they perform equally. That is true because they estimate the local noise statistics in the same way from samples of the same size and test the same statistical hypotheses. A 2-D sensor may perform better than a 1-D sensor if the clutter is spatially homogeneous and the 1-D sensor incurs a clutter-edge effect before reaching both critical sample sizes. In this case a 2-D sensor may achieve one or both critical sample sizes without a clutter-edge effect. It is necessary to be

more precise about the meaning of "homogeneous", since clutter is intrinsically heterogeneous. In the present context, clutter is homogeneous if its statistical properties change slowly in all directions over extents \geq the sensor's reach. If the clutter is spatially inhomogeneous, a 2-D sensor might be inferior to a 1-D sensor. This could occur if the noise statistics changed slowly in the scan direction but rapidly in another direction, resulting in a clutter-edge effect with the 2-D but not the 1-D sensor. A bright cloud edge parallel to the scan might lead to that outcome. The principle applies in all these cases because it involves only invariable relations between statistical properties of the noise and sensors. The principle is inapplicable (e.g., with low-pass clutter) only if the noise and sensors do not have these properties. However, the intended use of the principle is analysis of data, not hypothetical cases. The principle tells one how to determine whether 1-D and 2-D threshold sensors perform differently, but the actual determination awaits analysis of data.)

We next state less general results and conclusions. These are valid only for a 1-D adaptive threshold sensor following a 1-D LMS filter when the filter input is from an optical sensor having an $NEI \geq 1.5 \times 10^{-13} \text{ W/cm}^2$ and a spatial resolution better than $0.15 \times 0.36 \text{ mR}$. Further restrictions are imposed by all the natural and man-made experimental conditions existing when the data were collected, as discussed above in section II(D) and summarized in the appendix.

Under the stipulated conditions, the standard critical sample size in clear sky (100 independent values) corresponds to 250 data extending over 10 mR; the critical sample size in clutter is 6 mR or 150 data. A clutter-edge effect with an onset between 8 and 10 mR results in an optimum threshold-sensor size of 10 mR, but increasing the size to 14-15 mR increases the threshold parameter and equally detected signal strengths only 0.2 dB, indicating a very weak clutter-edge effect. (The weakness is due to the fact that the worst clutter in the filtered data is the same order of magnitude as the NEI.) Similarly, the threshold sensor can be made smaller than the optimum size with very little loss of signal detection; for example, the loss is only 0.2 dB at the critical sample size in clutter. Consequently, the best 1-D threshold sensor size, under the stated conditions, is the critical sample size in clutter because the larger optimum size risks a clutter-edge effect but improves signal detection very little. A 2-D threshold sensor probably would not be advantageous in this case, even though the onset of the clutter-edge effect is slightly below the critical sample size in clear sky; the reason is that the weakness of the clutter-edge effect allows the critical sample size in clear sky to be reached with no significant loss of signal detection.

Finally, signals are almost always detected at their peaks, although rarely a signal missed at the peak is detected elsewhere on the waveform. Off-peak detection is more likely at lower detection frequencies but is never very important. Specifically, at detection

frequencies ≥ 0.5 , a signal missed at the peak has less than a 1 in 80 chance of being detected elsewhere on the waveform. Although this result was obtained from computations with LMS-filtered noise, it is probably true for any noise with zero local mean and correlation length about the same as the signal length.

Appendix. Summary Descriptions of Data, Algorithms, and Method of Simulation

(This appendix, excepting Fig. 9, summarizes the detailed descriptions of the same topics in the previous article.¹ The summary is provided at the request of the editor and reviewers to make this article reasonably self-contained.)

The background data were collected, recorded, and digitized by the General Electric Company.¹⁴ The optical sensor consisted of a scanning telescope with a 4.0-4.8 μm spectral filter and an InSb detector of six photosensitive elements in the telescope's focal plane. Each element was 0.15 mR in azimuth (the scan direction) and 0.36 mR in elevation; the element width was matched to the diameter of the point-source image. Data collection took place at 43°N, 76°W on 22 February 1974 at 5 p.m. with the telescope pointed in a westerly direction at an elevation of 12-13°. The temperature was 60°F, relative humidity 70%, and visibility 25 km or more. The scene contained clear sky (38% of the total field of view) and midlevel cumulus clouds (62% of the field) with extremely bright edges backlit by the setting sun. The range to the clouds was 10-20 km, as estimated from their type and the conditions of observation.

The steps taken in recording and digitizing the detector outputs are illustrated in the top half of Fig. 7. Owing to the brightness of the cloud edges, wideband filters were needed to limit the outputs to the dynamic range (42 dB) of the analog tape recorder. The

AD-A154 793

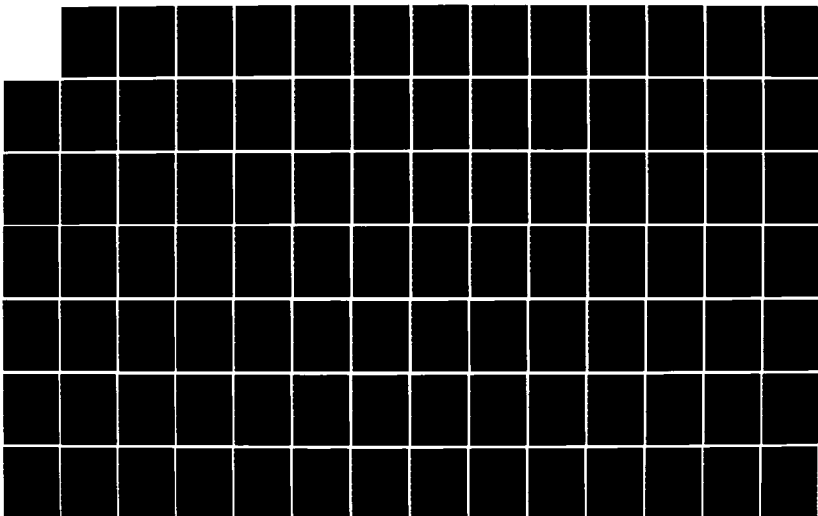
CALIBRATION AND USE OF CLUTTER DATA FOR SIMULATION(U)
WESTERN KENTUCKY UNIV BOWLING GREEN H S LONGHIRE 1985
N00014-84-C-2034

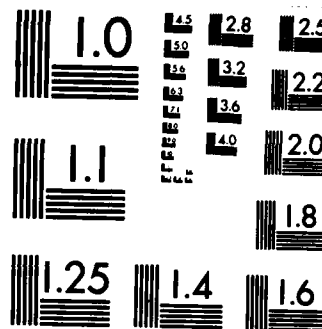
2/3

UNCLASSIFIED

F/G 17/5

NL





MICROCOPY RESOLUTION TEST CHART
NATIONAL BUREAU OF STANDARDS-1963-A

passband was sufficiently wide so that its effect on the noise and signal (the point-source output of a detector element, Fig. 8) was negligible compared to the effect of the LMS filter simulated in this work. On the other hand, the low-frequency time constant, (1/40) sec, was too small relative to the scan time, (3/4) sec, to allow radiometric calibration of the data. The noise equivalent irradiance (NEI), referred to the wideband output, was $1.5 \times 10^{-13} \text{ W/cm}^2$. Recording, sampling, and digitization did not increase this value, i.e., did not add more noise to the data. The sampling rate was about 3.5 per dwell, and the sampling time was much less than the dwell time (0.344 msec). Digital values consisted of a sign bit and eleven numeric bits.

Wideband output from a typical cloud edge is plotted in Fig. 2A. The maximum clutter-to-NEI ratio is about 36 dB. Inspection of the plot and physical considerations indicate that the clutter is the sum of two components: a deterministic, pure clutter component from spatial changes of cloud radiance, and a random component from photon-arrival fluctuations and charge fluctuations in the detector and electronics. (When the random component exists alone, it is often called NEI noise or detector noise.) Fig. 2B shows the cloud-edge clutter of Fig. 2A after passage through the LMS filter described below. The maximum clutter-to-NEI ratio is reduced about 20 dB, and the clutter below 158 mR and above 165 mR is visually indistinguishable from LMS-filtered uniform-sky noise. Obviously the LMS filter suppresses the pure clutter component very effectively.

However, clutter suppression alone is not an adequate measure of filter performance; the signal-to-clutter and signal-to-noise ratios given below are needed also.

The LMS filter is a linear, time-invariant, electronic filter; with input from a scanning optical sensor, it acts as a spatial filter. Its impulse response is derived as follows: The point-source signal and additive noise are modeled, respectively, by a raised cosine function $s(t)$ and by the first two terms of a Maclaurin series $n(t) = b_0 + b_1 t + \dots$; thus the sum of noise and a signal with arbitrary amplitude A is $m(t) = As(t) + (b_0 + b_1 t)$. This model is fit by least squares to the filter output $v(t)$ over one period of the raised cosine, resulting in integral expressions for the best-fit values of A , b_0 , and b_1 . The equation for the best-fit A is a convolution integral which yields the LMS filter's impulse response.¹³ Fig. 8 shows this impulse response and output from a point-source input; Fig. 9 exhibits the filter's amplitude response together with the square roots of the clutter power density and signal energy density. (The power density of the uniform-sky noise is approximately constant to the wideband cut-off at 5600 Hz.) The impulse response is shaped like the signal's mirror image but lowered so that its average value is zero. The shaping matches the filter to the signal; the symmetry and lowering cause the filter to eliminate the dc and entire odd part of any input. Together the shaping and lowering of the impulse response result in the LMS filter having the optimum ratio of peak signal to rms noise for a point-source signal

in noise whose power spectrum varies as the reciprocal of the squared electrical frequency. Such a function models cloud clutter noise. The LMS filter is, therefore, not optimum in clear sky, but it provides a good compromise between performance in clear sky and in cloud clutter. For example, the LMS filter has a maximum signal-to-clutter ratio which is 22 dB greater than that of the low-pass filter with the best possible signal-to-noise ratio in clear sky. The price paid for this large advantage in clutter is only 1.3 dB of clear-sky signal-to-noise ratio, relative to the same low-pass filter.¹

The adaptive threshold sensor of Fig. 1 is discussed in section II where it is explained that this sensor makes a statistical test for signals if the noise mean of the filter output is zero locally and globally (over extents \geq the sensor's length). Uniform-sky noise has this type of mean, as does the cloud-clutter output of a filter with a high cut-on frequency like that of the LMS filter (Fig. 2B). With a low cut-on frequency like that of the wideband filter, the clutter mean is zero globally but not locally (Fig. 2A). With a low-pass filter, whose cut-on frequency is zero, the clutter mean is non-zero both locally and globally. The sensor of Fig. 1 cannot operate statistically with the clutter output of a filter having a low or zero cut-on frequency, because it cannot estimate local values of the mean μ and mean absolute deviation η for setting the threshold ($\mu + K\eta$). Rather, the sensor estimates the local noise magnitude, which is large, and sets the threshold at a level several times greater, virtually turning off the surveillance set in clutter.

A filter should condition the noise so that the threshold sensor can function statistically. The LMS filter does this by reducing the correlation length in clutter so that the noise average is zero within the sensor frame.

The simulation was carried out with a digital computer using programmed algorithms for the LMS filter and adaptive threshold sensor. Fig. 1 is effectively a flow chart from which the reader can program the sensor algorithm, given also that the shutter prevents the wings of a point-source signal centered on the signal window from distorting the estimate of the local noise dispersion. An approximation described in section II(C) can be used to simplify the sensor algorithm with negligible error. The principles underlying any digital filter algorithm in both the time and frequency domains are discussed in many texts, edited books, and review articles; reference 15 gives an especially lucid, introductory account; references 1 and 13 describe the time-domain LMS algorithm used in this work. After studying reference 15, a reader with no prior knowledge of digital filter principles can program the LMS algorithm with understanding. Regrettably, the principles cannot be briefly and intelligibly summarized for him. However, if he is content to program the algorithm without understanding, two facts are all he needs: Each LMS filter output is a weighted sum of the present and the M consecutive past inputs, and the $(M+1)$ normalized weights can be obtained from the recipes given in reference 1, section IV.

The main steps of the simulation are indicated in the lower

half of Fig. 7. After LMS-filtering of the background data, the number of false alarms was determined as a function of the threshold parameter K . This was done by calculating the ratios $K = x_w / \langle |x_f| \rangle$ and ordering them in statistical frequency tables. The value of K which allowed one false alarm in all the data was then read from the tables and given to the threshold sensor algorithm. As each noise value entered the signal window it was added to a simulated signal amplitude, and the sum was tested against the threshold $K \langle |x_f| \rangle$. (Because the filter is linear, simulated signals can be added to the noise either before or after the filter, provided the signal waveform appropriate for each case is used.) The simulated signal amplitude was then increased and the process repeated to determine the curves of detection frequency in Fig. 5. This procedure assumes that a signal is detected only at its peak, an approximation which introduces $< 2.5\%$ error in detection frequencies ≥ 0.5 .

References

1. M. S. Longmire, A. F. Milton, and E. H. Takken, Appl. Opt. 21, 3819 (1982).
2. H. M. Finn and R. S. Johnson, RCA Review 29, 414 (1968).
3. B. O. Steenson, IEEE Trans. Aerosp. Electron. Syst. AES-4, 529 1968.
4. R. Nitzberg, IEEE Trans. Aerosp. Electron. Syst. AES-8, 27 (1972); AES-9, 399 (1973).
5. Dr. V. Gupta, J. F. Vetelino, T. J. Curry, and J. T. Francis, IEEE Trans. Aerosp. Electron. Syst. AES-13, 11 (1977).
6. R. Nitzberg, Proc. Soc. Photo-Opt. Instrum. Eng. 178, 33 (1979).
7. R. A. Steinberg, Appl. Opt. 19, 77, 1673, 3426 (1980).
8. Tests of hypotheses are discussed in most statistics texts, e.g., J. E. Freund and R. E. Walpole, Mathematical Statistics (Prentice-Hall, Englewood Cliffs, NJ, 1980), 3rd ed., Chs. 12-13.
9. M. G. Kendall and W. R. Buckland, A Dictionary of Statistical Terms (Longman Group Ltd, London, 1982), 4th ed., p. 172.
10. J. E. Freund and R. E. Walpole, *op. cit.*, Secs. 8.2-8.3.
11. M. G. Kendall and W. R. Buckland, *op. cit.*, p. 45.
12. D. E. Knuth, The Art of Computer Programming (Addison-Wesley, Reading, MA, 1981), 2nd ed., vol. 2, p. 117.

References (cont.)

13. E. H. Takken, D. Friedman, A. F. Milton, and R. Nitzberg, Appl. Opt. 18, 4220 (1979).
14. B. A. Boerschig and D. B. Friedman, "IR Signal Processing Techniques," Final Report, Office of Naval Research contract N00014-73-C-0249 (General Electric Co., Syracuse, NY, 1974).
15. K. Steiglitz, An Introduction to Discrete Systems (John Wiley & Sons, New York, 1974).

Figure Captions

Figure 1. Schematic diagram of an adaptive threshold sensor. The parameter K is fixed, but the threshold T varies with the estimate $\langle |x_f| \rangle$ of the local noise mean-absolute-deviation. The value of K required to prevent a false alarm from window value x_w is $x_w / \langle |x_f| \rangle$.

Figure 2. Plots of backlit cloud-edge clutter at the outputs of the (A) wide band and (B) LMS filters. The wide band output provided the noise data used in this work. The NEI unit of the ordinate is the standard deviation (and rms voltage) of the clear-sky noise from the wide band filter.

Figure 3. Sampling standard deviations (s.d.s) of sensor frame-averages $\hat{\eta} = \langle |x_f| \rangle$ as functions of sample (frame) size, noise type, and segment length. The noise means μ are zero locally and globally, so that noise magnitude $|x|$ and absolute deviation $|x - \mu|$ are identical, and their means are estimated by $\hat{\eta}$ locally and globally. The sample sizes are 8, 18, 36, 80, 144, 240, 340, 440, 540, and 640 data. Noise data of each type are divided into segments of the specified lengths. There are nine segments in each of sets A-D, and ten in each of sets E-F. Variances are calculated about $\eta = \langle |x| \rangle$, the average magnitude and average absolute deviation of all data in a set. Bars show the ranges of the sampling s.d.s of the

Figure Captions (cont.)

segments; dots indicate the sampling s.d. of the population (all segments of the set). A population sampling variance is equal to the average of the associated segment sampling variances. Sampling s.d.s $\sigma_{\bar{\eta}}$ are divided by the associated population s.d. σ to facilitate comparison of results from different data sets. The diagonals represent the logarithmic form of equation (1), which is the relation between sample size and sampling s.d. given by the theorem on the sampling distribution of the mean. The lines through the dots of data sets C-F are drawn for best visual fits; departures from the diagonals are due to non-random sampling, correlation, and non-stationarity of the noise.

Figure 4. Sampling standard deviation (s.d.) and threshold parameter K as functions of threshold-sensor-sample size and noise type. The sample sizes are 36, 80, 144, 240, and 340 data. (A) Population sampling s.d.s for the data sets of Figs. 1E and 1F; each set contains 10 segments. (B) Threshold parameters for one false alarm (f.a.) determined from the two data sets of reference 1, each of which contains 114 segments.

Figure 5. Frequencies of detecting simulated signals in LMS-filtered natural background noise with threshold sensors of

Figure Captions (cont.)

different sizes. These results are calculated from the two data sets used in reference 1; each set contains 114 segments. The difference between signals and pseudo signals is explained in section II(D). Results for a frame size of 144 data are in reference 1; they are hardly distinguishable from the results for a frame size of 340 data. The threshold parameters for one false alarm (f.a.) are plotted in the top curve of Fig. 4B.

Figure 6. Equally detected signal strength as a function of threshold-sensor size, noise type, and detection frequency. Simulated signal strengths for these plots were read from the curves in Fig. 5. The curves here show simulated signal strengths required to achieve the indicated detection frequencies with threshold sensors of different sizes. The difference between signals and pseudo signals is explained in section II(D).

Figure 7. Steps taken in collecting the background data and performing the simulation.

Figure 8. Time-domain properties of the point-source signal (input) and the LMS filter. The output is the convolution of the input and the LMS impulse response. The tick marks are one dwell time apart.

Figure Captions (cont.)

Figure 9. Frequency-domain properties of the LMS filter, the clutter, and the point-source signal. The filter's phase response (not shown) is directly proportional to the frequency.

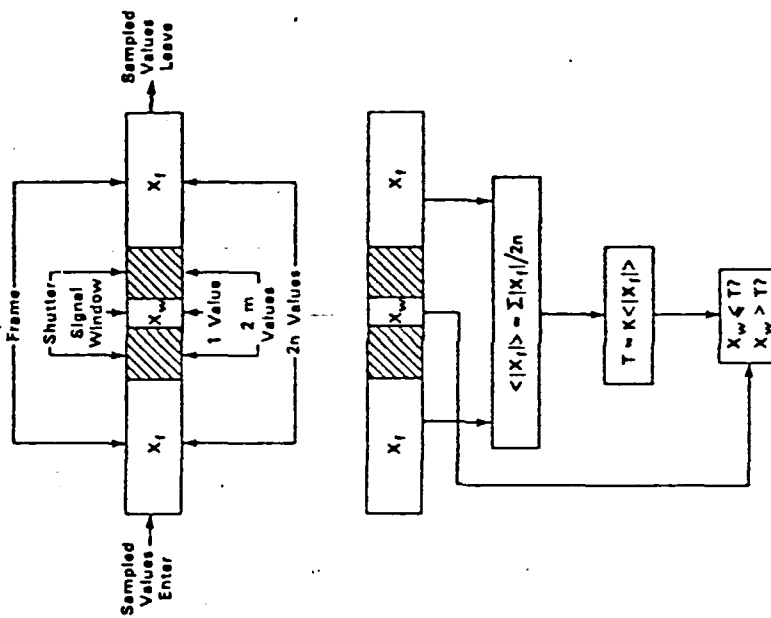


Figure 1

MONTAUK CALIBRATION DATA
 NAV100
 0 DAYS 9 HOURS 36 MINUTES 41.3 SECONDS
 CHANNEL 1

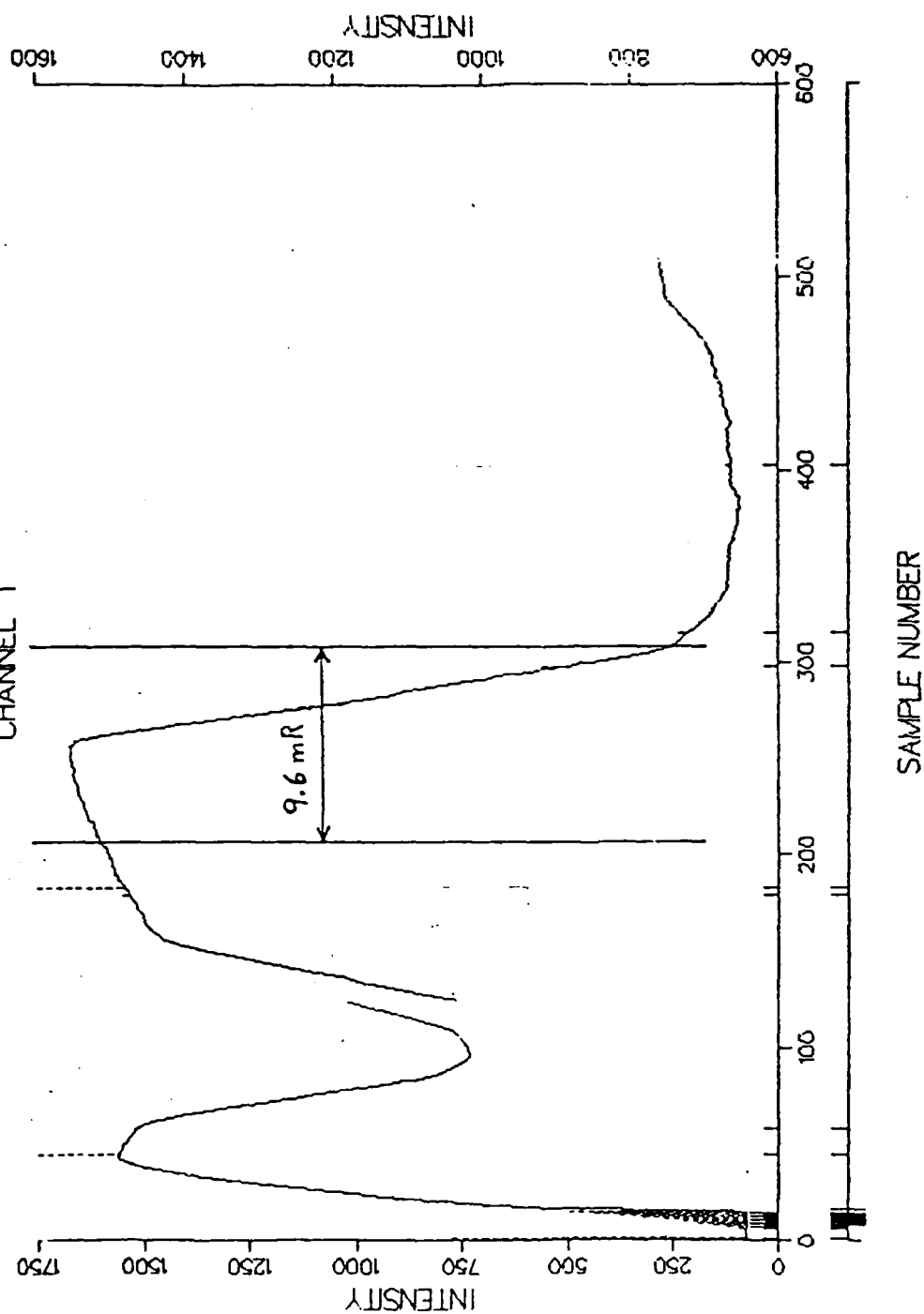


FIGURE 5: PULSE FROM MID-WAVE CHANNEL 1 (LOW ELEVATION)

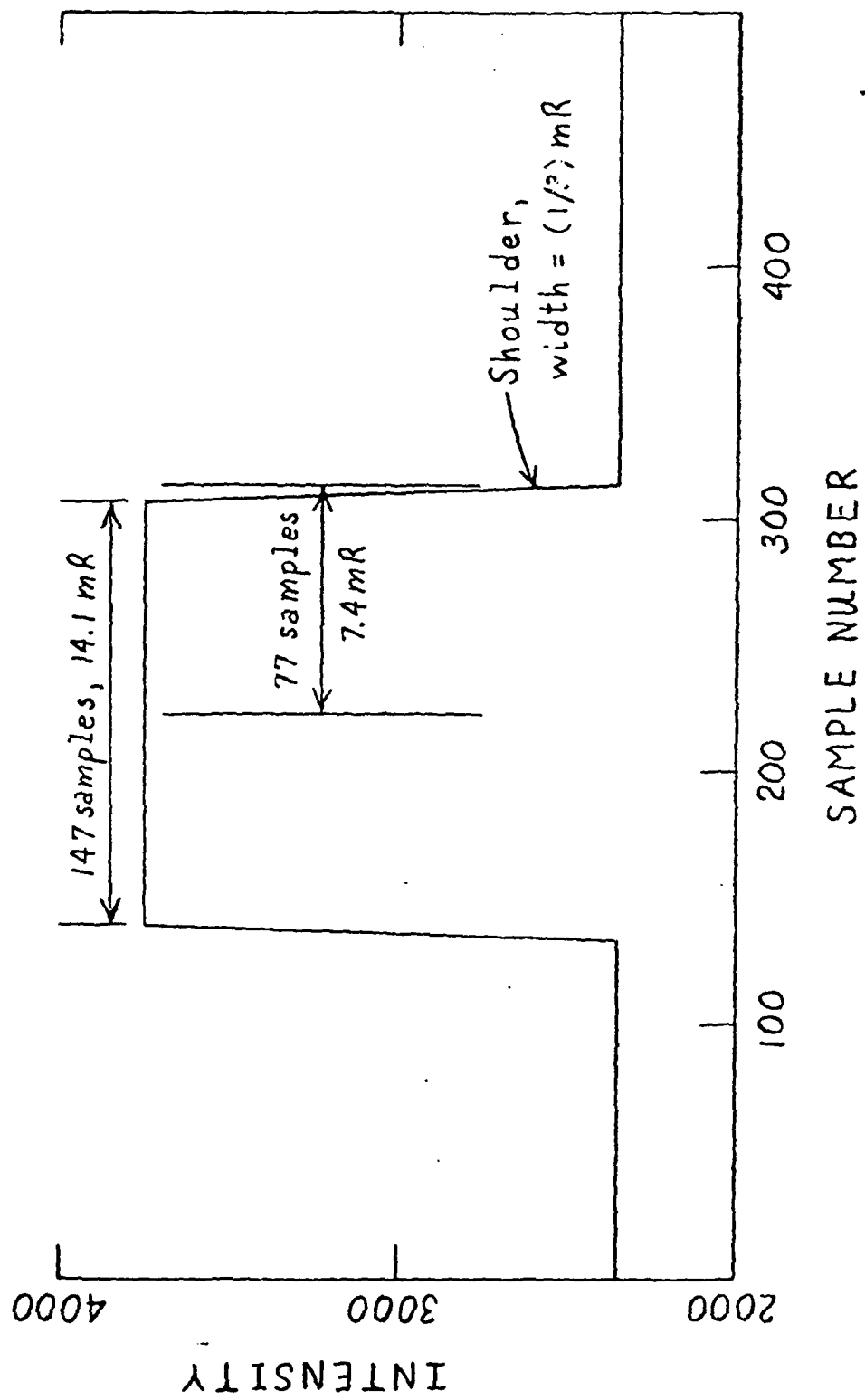


FIGURE 2: IDEAL PULSE PRODUCED BY TRUE IMAGE

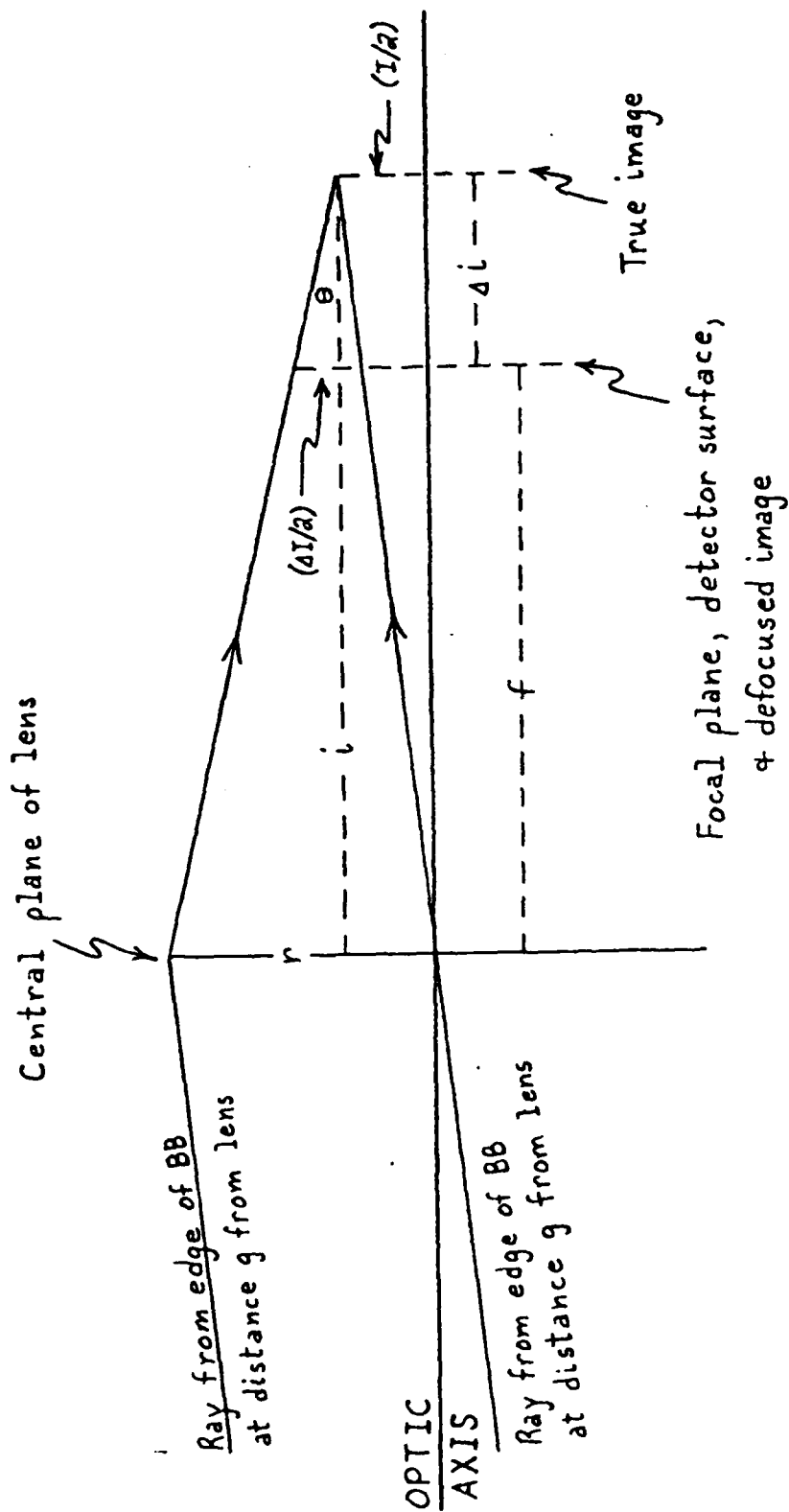
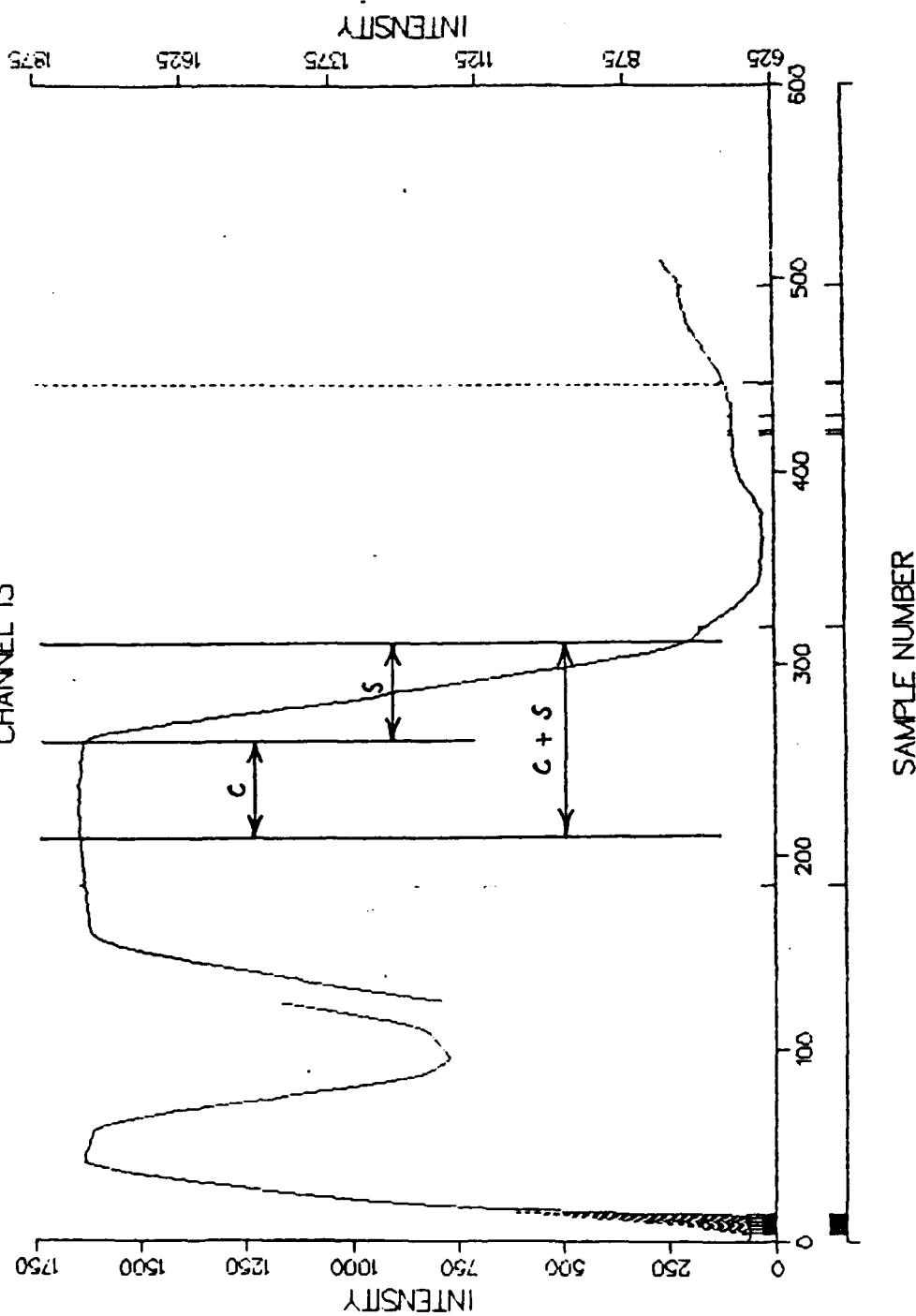


FIGURE 1: SCHEMATIC OPTICAL GEOMETRY

MONTAUK CALIBRATION DATA
NAV100
0 DAYS 1 HOURS 36 MINUTES 40.8 SECONDS
CHANNEL 13



FIELD CALIBRATION

MONTAUK POINT

IN GENERAL

Part 3A

PART 3A

VUGRAPHS AND SUPPLEMENTAL TEXT FOR
BMAP REVIEW, 3 MAY 1984

85 04 30 080

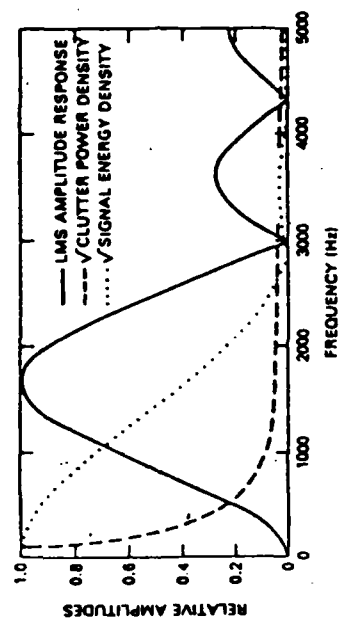


Figure 9

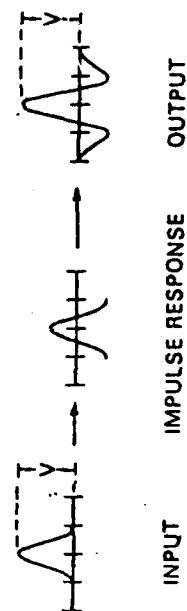


Figure 8

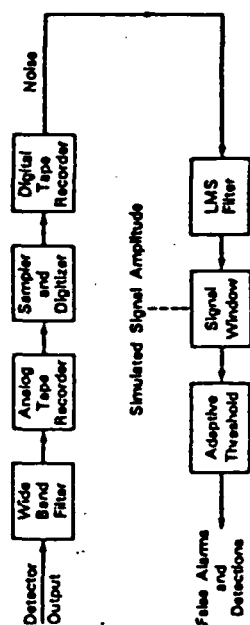


Figure 7

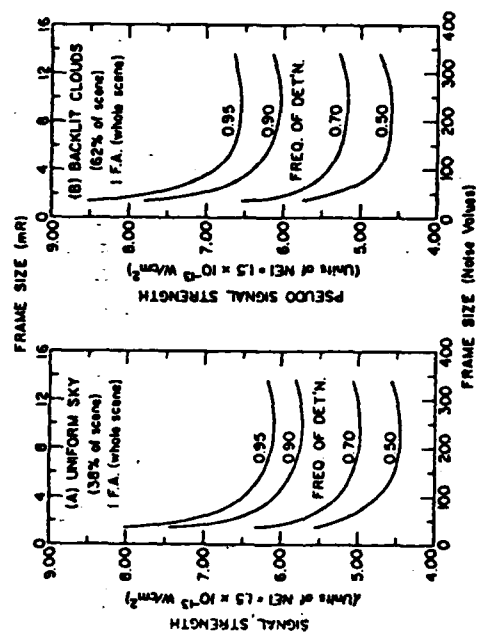
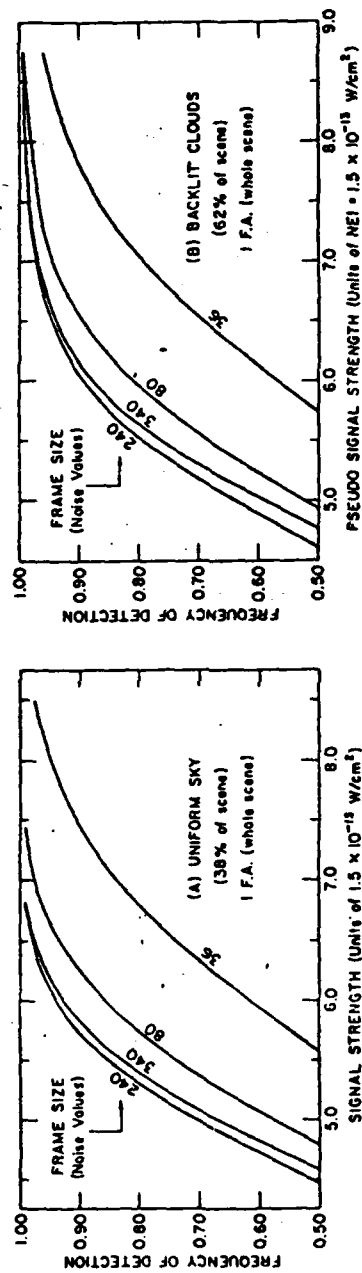


Figure 6



Do not reduce to column width.
 Figure 5 Figure is scaled for two column width.

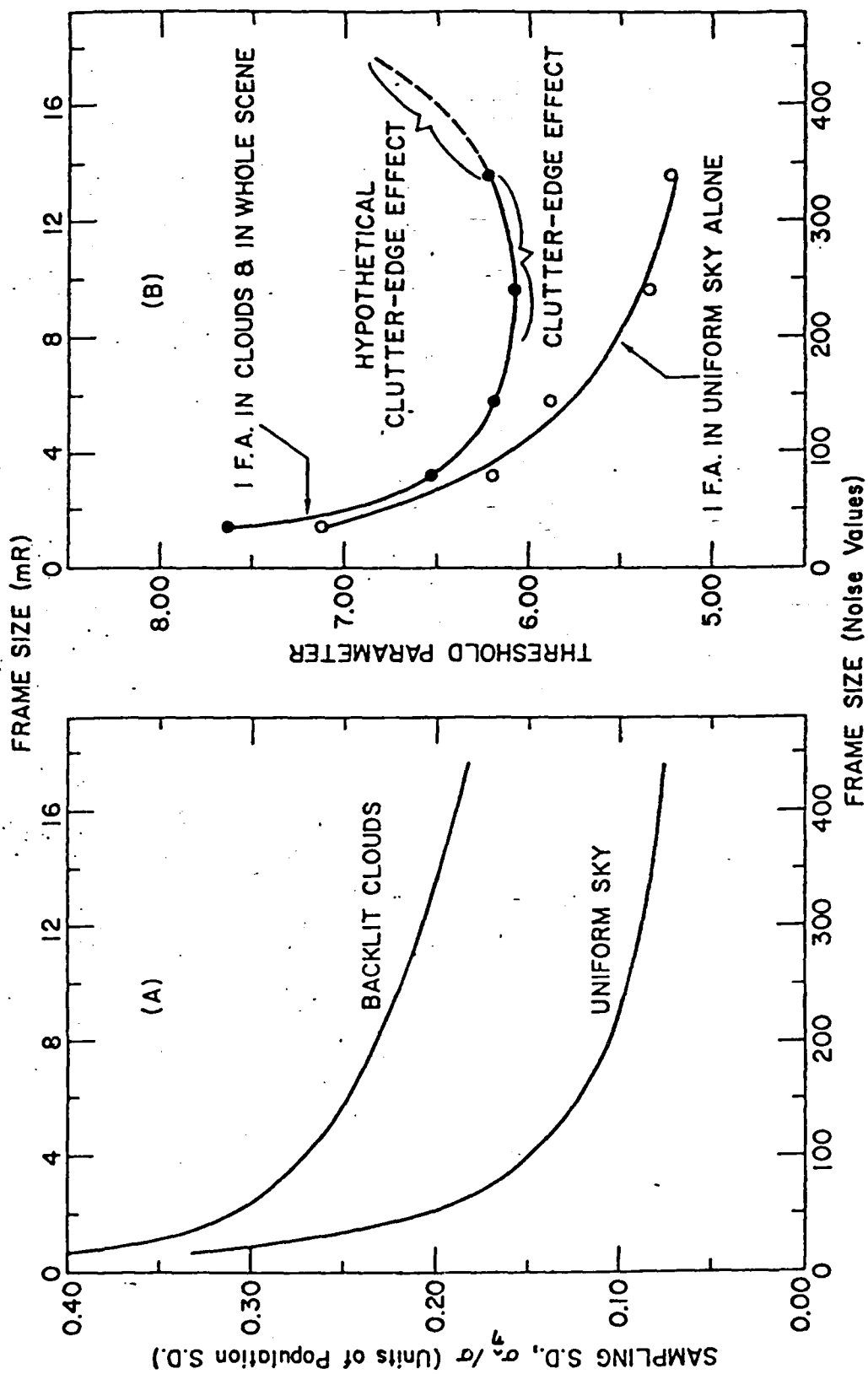


Figure 4
Do not reduce to column width.
Figure is scaled for two column width.

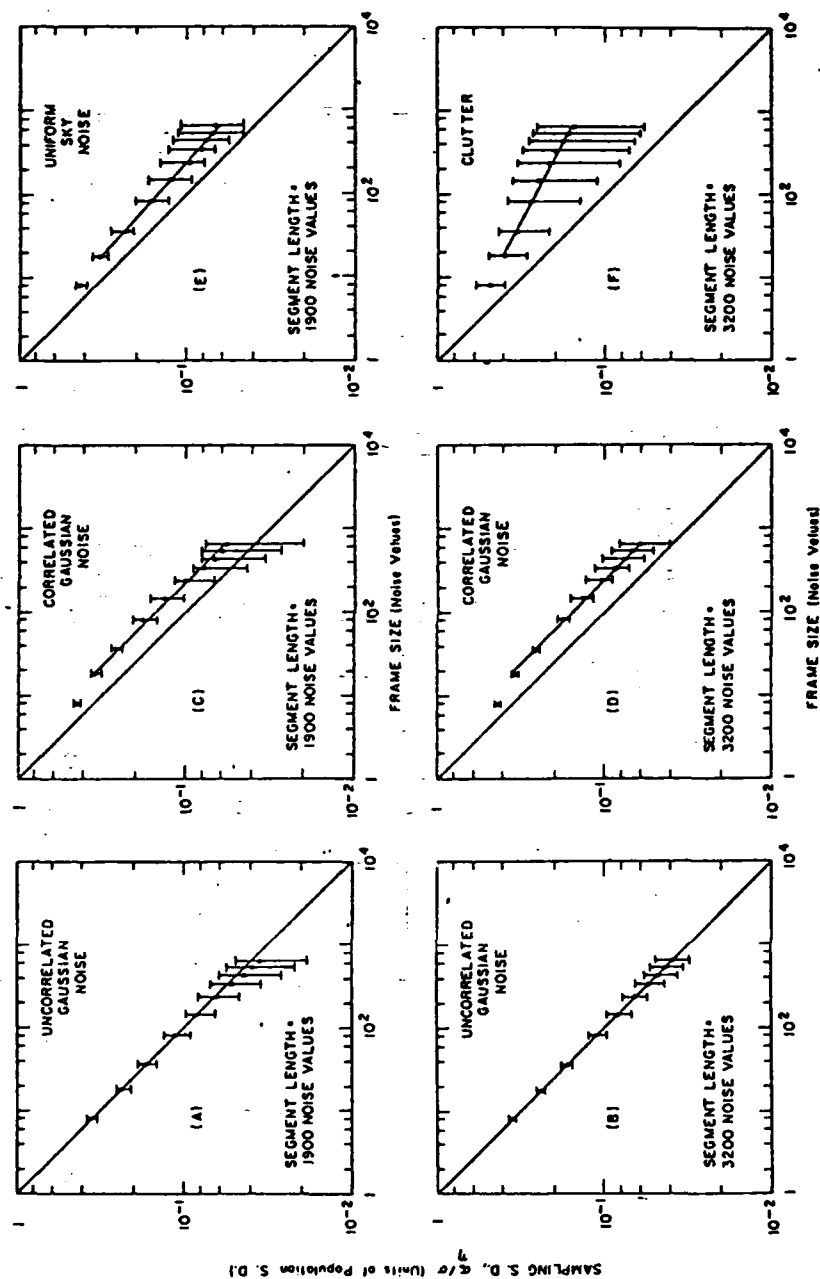


Figure 3 Do not reduce to column width.
Figure is scaled for two column width.

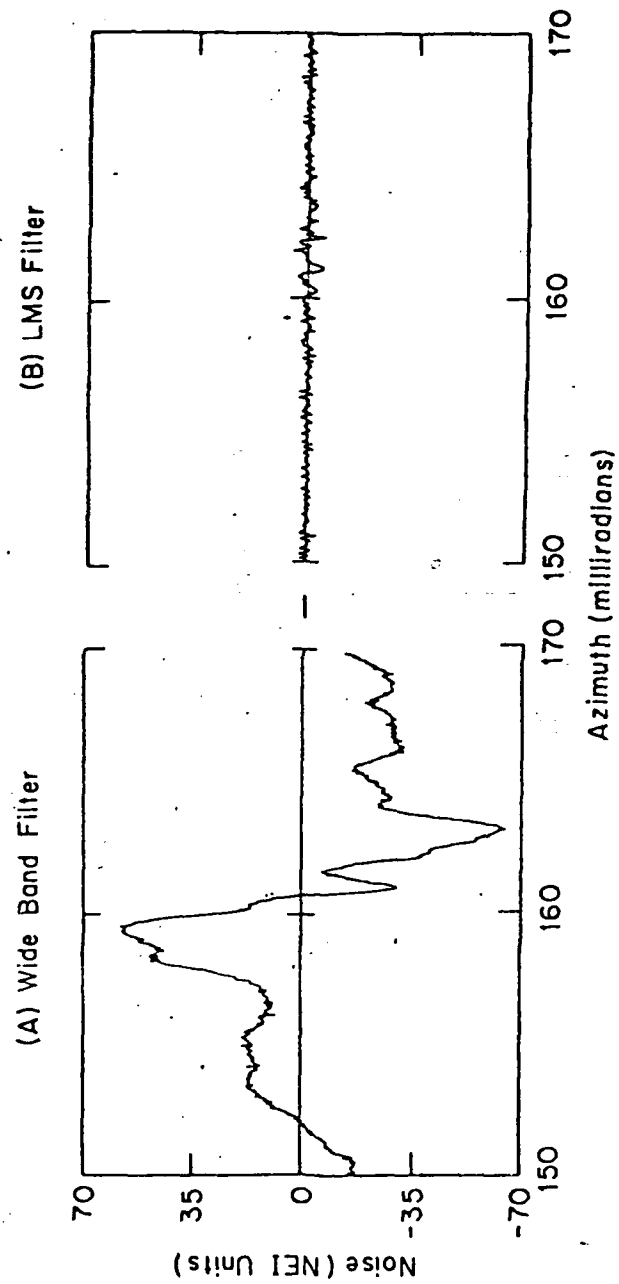


Figure 2
Do not reduce to column width.
Figure is scaled for two column
width.

FACTORS AFFECTING BB PULSE SHAPE

1. ORIENTATION OF BB RELATIVE TO SCAN
2. VERTICAL POSITIONING OF BB IMAGE ON DETECTOR ARRAY
3. FLUX DISTRIBUTION IN DEFOCUSED IMAGE
4. ALINEMENT OF OPTICS AND DETECTORS
5. RESPONSE OF ELECTRONICS
6. BB TEMPERATURE DISTRIBUTION

SUGGESTIONS FOR FIELD CALIBRATIONS DURING MEASUREMENTS AT BEDFORD, MA

1. REDUCE RADIOMETER APERTURE WITH REMOVABLE STOP.
2. ADJUST BB TEMPERATURE TO PROVIDE APPROPRIATE PEAK SIGNAL.
3. OBTAIN ANOTHER BB.
4. PUT BBs 100 FT. FROM RADIOMETER.
5. BEFORE RECORDING CHECK SCOPE DISPLAY TO ENSURE THAT
 - A. SIDES OF BBs ARE NORMAL TO SCAN.
 - B. BB IMAGES ARE VERTICALLY CENTERED ON DETECTORS.

FIELD CALIBRATION ALTERNATIVES

1. DISTANT EXTENDED SOURCE
2. CLOSE SOURCE
 - A. EXTENDED
 - B. POINT (JONES METHOD)
3. "COLLIMATOR" (SPECTACLES)

AT LEAST 2, PREFERABLY 3, TEMPERATURES NEEDED

"COLLIMATOR"

FORMS VIRTUAL OBJECT FOR RADIOMETER OPTICS

EXPENSIVE (\$50K), LONG DELIVERY TIME, 2 NEEDED

CURE RADIOMETER'S FAR-SIGHTEDNESS WITH SPECTACLES? COST?

CLOSE SOURCES

SEVERAL ADVANTAGES

BUT ONLY ONE SOURCE CAN BE IN VIEW

TEMPERATURE-CONTROLLED APERTURE COVERS? COST?

EXTENDED SOURCE WISH LIST

THREE PANELS WITH TEMPERATURE RANGES

- A. 190 TO 240 K (-80 TO -30 C)
- B. 240 TO 290 K (-30 TO 20 C)
- C. 290 TO 340 K (20 TO 60 C)

PANEL SIZE: 18 X 18 INCHES

COMMERCIALLY AVAILABLE SOURCE

BARNES 11-140T

SINGLE PANEL, 12 x 12 INCHES

TEMPERATURE RANGE: AMBIENT TO 500 K (230 C)

COST: \$4K

Comments on Field Calibration of the BMAP Radiometer

Martin S. Longmire

3 May 1984

Introduction

The optical sensors used in the Background Measurements and Analysis Program (BMAP) are to be calibrated in the laboratory so that data collected in the field can be assigned absolute radiance values. Internal references in the sensors can be used to link their responses in the field to the laboratory calibrations, but this provides only one calibration point, and at least two, preferably three, are needed to estimate both reference radiance and responsivity. To strengthen the link between laboratory calibration and field response, a second calibration in the field is desirable.

This note considers the questions, "What is the purpose of a field calibration (already answered), how should it be performed, and what information must it provide?" Concomitantly, the first steps toward reducing the field calibrations made during the background measurements at Montauk Point are described.

To begin, the possible methods of calibration are reviewed. "Calibrations are categorized into two groups: those in which the radiometer field stop is partially illuminated by the calibration source; and those in which the stop is totally filled with uniform calibration radiation." (The Infrared Handbook, p. 20-13.) The first type of calibration is impractical for field work with a multichannel detector because the source image must be carefully positioned several times to calibrate all channels. BMAP field calibrations must be of the second type. "The latter can be realized with a so-called extended source, either distant -- or close --, by a collimator -- or by a proper placement of a point source very close to the entrance aperture (the so-called 'Jones method' --)." (ibid.)

16

The Jones method is attractive in several ways: it can be used both in flight and on the ground; the source is easily accessible to the operators; it does not have to be carefully positioned; and atmospheric absorption is negligible so that the spectral distribution can be the same for the field and laboratory calibration. Two disadvantages are the need for very small standard sources and means of positioning them so that the mounts do not radiate significantly into the sensor. Also, because the sources are not imaged on the detectors, they cannot be exposed simultaneously to the sensor. Furthermore, radiation received by a detector element passes through only a small part of the lens, not all of it as in the field measurements and laboratory calibrations. The same comments apply to calibration with a close extended source except the remarks concerning source size and aperture differences. Chiefly because two sources cannot be used simultaneously, close-source calibrations are not completely satisfactory, but neither are the alternatives, so the close source methods cannot be ruled out.

Use of a collimator has the disadvantage that two would be required to deploy two sources. This leaves the distant extended source method. Since it was used at Montauk Point, it will be explored more fully with reference to conditions there. These conditions result in a defocused image on the detector. A problem concerning the size of this image is stated, a solution is given, and the implications of the solution are discussed. Finally the shapes of the calibration outputs recorded on Montauk Point are considered, and a procedure is described for analyzing them to obtain calibrations.

Problem

The radiometer is focused at infinity and then pointed at a blackbody (BB) placed a large but finite distance from the lens. Thus, the blackbody image lies behind the detector surface, which is in the focal plane. There

are two optical systems, long wave (LW) and mid wave (MW), with parallel axes $4\frac{5}{8}$ inches apart in the vertical plane. How does the size of the defocused "image" on the detector compare to the size of the true (focused) image?

Assumptions

The solution is based on the thin lens equations of geometric optics. Aberrations are ignored. The center of the BB is assumed to be on an optic axis. (When the BB is far away its center is more likely to be on or near the mid-line between the optic axes, but this results in negligible error, as verified by computation.) The true image is required to fill or overfill the instantaneous field of view (IFOV) in the scan (horizontal) direction and the total field of view (TFOV) in the cross-scan (vertical) direction.

Notation and Optical Parameters at Montauk Point

f = focal length of lens, 6 inches

r = lens (or aperture) radius, 2 inches

Horizontal IFOV = $(1/3) mR$

Vertical TFOV = $5(1/3) mR$

g = object (BB) distance, 840 inches

G = object (BB) size, 12 x 12 inches.

i = true (focused) image distance

I = true image size

Subscripts h and v denote the horizontal and vertical directions

Δ denotes a change in any quantity.

Figure 1 shows the optical geometry.

Solution

From Figure 1 and the thin lens equations:

$$\frac{\Delta I}{I} = \frac{2 \Delta i \tan \theta}{I} = \frac{2(i-f)}{I} \left[\frac{r-(I/2)}{i} \right] = \left(1 - \frac{f}{i} \right) \left(\frac{2r}{I} - 1 \right)$$

$$\frac{1}{i} = \frac{1}{f} - \frac{1}{g} \text{ or } i = gf/(g-f)$$

$$I_{h,v} / G_{h,v} = i/g \text{ or } I_{h,v}/f = G_{h,v}/(g-f)$$

Eliminating image parameters from the right hand side of the equation for $(\Delta I/I)$ gives:

$$\begin{aligned} \left(\frac{\Delta I}{I} \right)_{h,v} &= \frac{f}{g} \left[\frac{2r(g-f)}{fG_{h,v}} - 1 \right] \\ &= \frac{2r}{G_{h,v}} \left(1 - \frac{f}{g} \right) + \frac{f}{g} = \frac{2r}{G_{h,v}} - \frac{f}{g} \left(\frac{2r}{G_{h,v}} - 1 \right). \end{aligned} \quad (1)$$

Since the true image must fill or overfill the field of view, the fractional enlargement $(\Delta I/I)_{h,v}$ of the defocused image is constrained by the two relations,

$$I_{h,v}/f = G_{h,v}/(g-f) \geq \text{IFOV}_h \text{ or } \text{TFOV}_v. \quad (2)$$

Discussion of BB Image Size

This solution can be checked against measurements made at Montauk Point.

From the optical parameters given above:

$$(\Delta I/I)_{h,v} = (1/3) + (2f/3g) = 0.3381$$

$$i = 6.04317 \text{ in. } I_{h,v} = 0.08633 \text{ in.}$$

$$I_{h,v}/f = 14.39 \text{ mR} > \text{IFOV}_h \text{ or } \text{TFOV}_v$$

$$\Delta I_{h,v} = 4.87 \text{ mR}$$

$$\text{Defocused image size} = (I + \Delta I)_{h,v} = 19.26 \text{ mR}$$

If this defocused image were scanned across a detector element $(1/3)$ mR wide, an output pulse with a base 19.6 mR wide would be produced. Figures (3) - (6) show pulses recorded at Montauk Point; their bases are about 19.2 mR wide, close enough to the calculated width to validate the solution. For comparison, Figure 2 shows an idealized pulse that would be produced by the true image.

(Further explanation of Figures (3) - (6) is in order. The first 112 samples of the plots display the internal reference pulse and the clamped amplifier output with the detector viewing itself. There are two intensity scales. The one on the left is for the part of the figure leftward of the tallest vertical line in Figure 3; the right-hand scale is for the rest of the figure. The saturation intensity is 4096, so the internal reference source almost saturates the LW output. The dashed spikes are recording errors; the second horizontal axis and ticks are related to these errors. The errors are of no interest here because they will be corrected before the calibration is derived.)

It is useful to consider how $(\Delta I/I)$ depends on the optical parameters. In eq. (1) ordinarily $1 \gg (f/g) \ll (2r/G)$; consequently the fractional enlargement of the defocused image is determined mainly by the ratio $(2r/G)$. With a finite object both ΔI and I approach zero as g approaches infinity, so $(\Delta I/I)$ is indeterminate. However, using l'Hospital's rule one finds

$$\lim (\Delta I/I)_g \rightarrow \infty = (2r/G).$$

This agrees with the approximation, $(\Delta I/I) \cong (2r/G)$, for large g . Differentiating eq. (1) with respect to object distance gives

$$\frac{d(\Delta I/I)}{dg} = \frac{f}{g^2} \left(\frac{2r}{G_{h,v}} - 1 \right). \quad (3)$$

CALIBRATION OVERVIEW

1. METHOD OF RADIOMETRIC CALIBRATION
CHOSEN, PARTIALLY VERIFIED
2. STANDARD SOURCE
SPECIFIED
3. LABORATORY & FIELD CALIBRATION PROCEDURES
DEVELOPED, PARTIALLY VERIFIED
4. RADIOMETRIC CALIBRATION EQUATION
TENTATIVELY ESTABLISHED, PARTIALLY VERIFIED
5. PROGRAM TO COMPUTE CALIBRATION PARAMETERS
WRITTEN, DEBUGGED, USED
6. LW ELECTRONICS RESPONSE
ANALYSIS BEGUN, SOME PROGRESS MADE
7. ISSUES & PROBLEMS



CALIBRATION OVERVIEW

MARTIN S. LONGMIRE

28 NOVEMBER 1984



Part 3 B

PART 3B

VUGRAPHS AND SUPPLEMENTAL TEXT FOR
BMAP REVIEW, 28 NOVEMBER 1984

04, 30 082

MONTAUK CALIBRATION DATA
 NAV100
 0 DAYS 9 HOURS 36 MINUTES 41.3 SECONDS
 CHANNEL 13

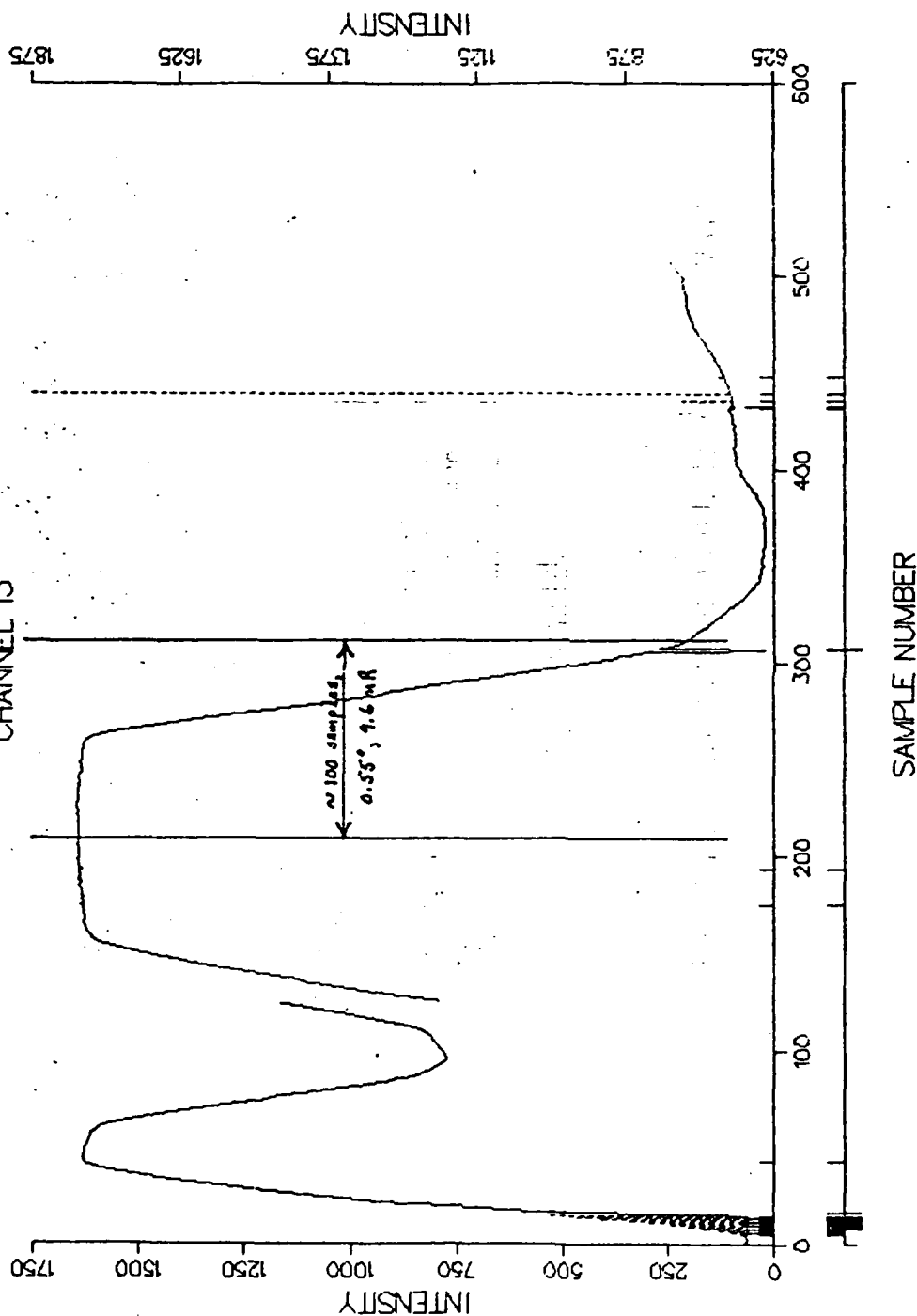


FIGURE 6: PULSE FROM MID-WAVE CHANNEL 13 (HIGH ELEVATION)

MONTAUK CALIBRATION DATA
 NAV100
 0 DAYS 9 HOURS 36 MINUTES 41.3 SECONDS
 CHANNEL 1

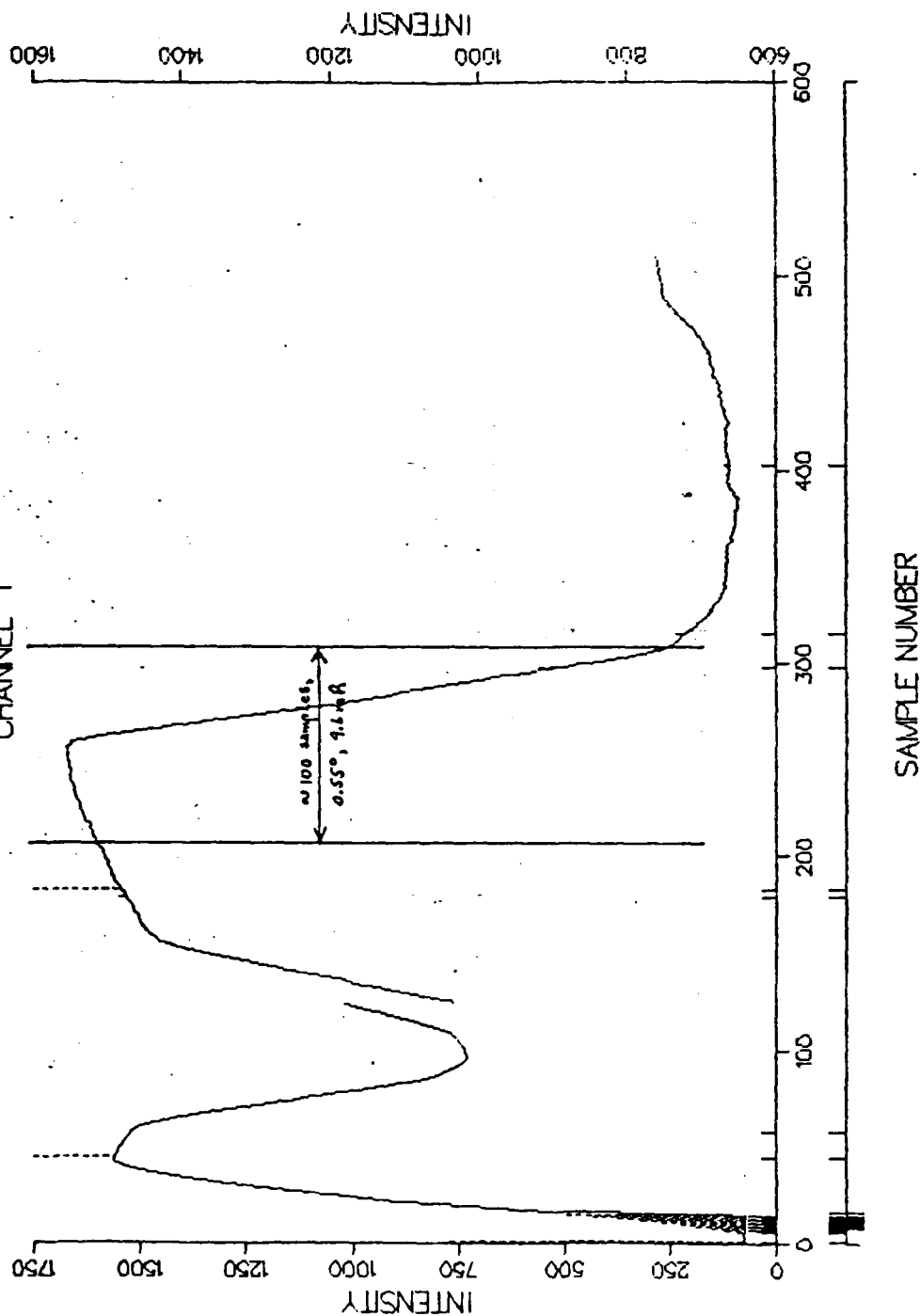


FIGURE 5: PULSE FROM MID-WAVE CHANNEL 1 (LOW ELEVATION)

MONTAUK CALIBRATION DATA
 NAV'100
 0 DAYS 9 HOURS 36 MINUTES 16.8 SECONDS
 CHANNEL 16

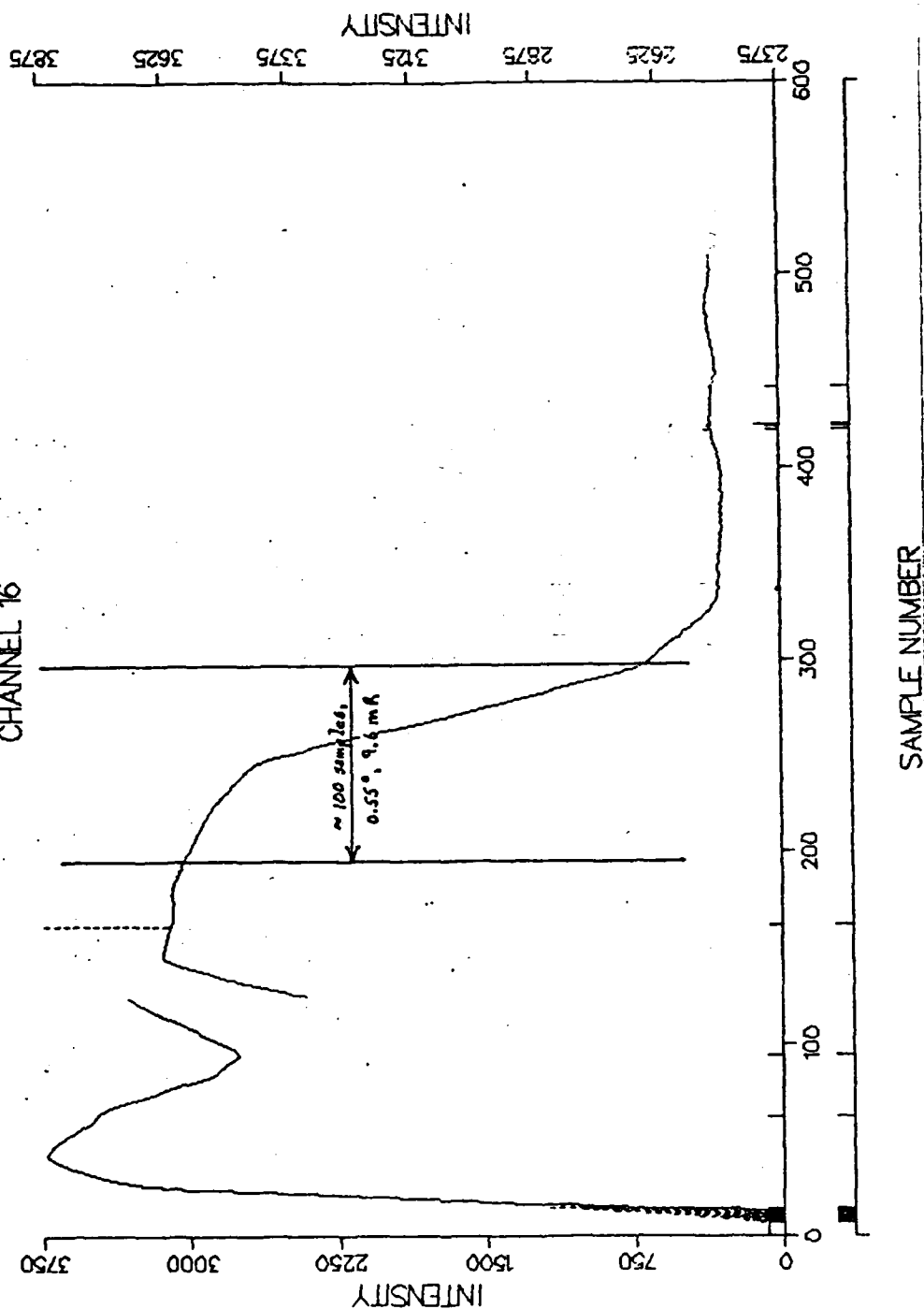


FIGURE 4: PULSE FROM LONG-WAVE CHANNEL 16 (HIGH ELEVATION)

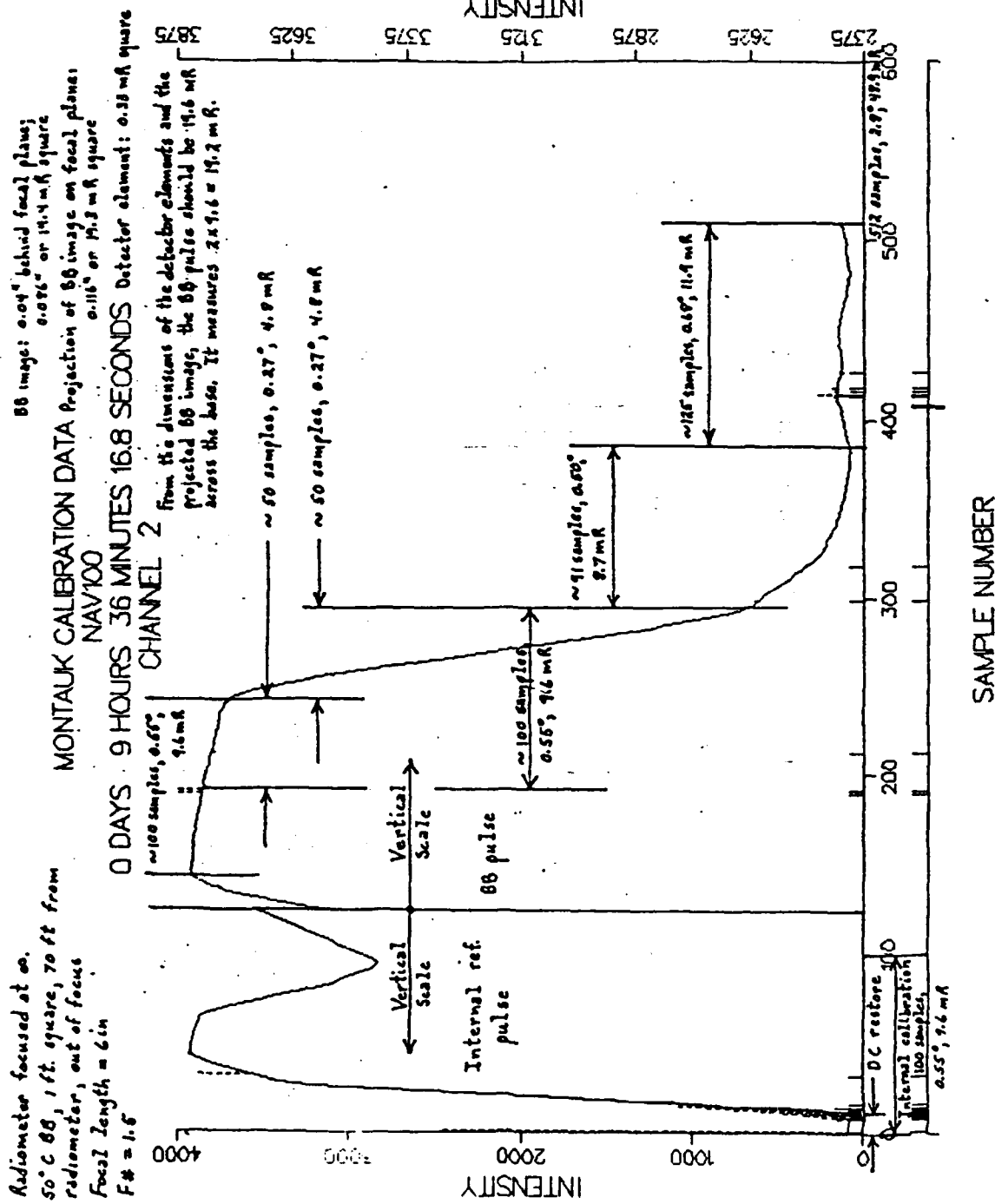


FIGURE 3: PULSE FROM LONG-WAVE CHANNEL 2 (LOW ELEVATION)

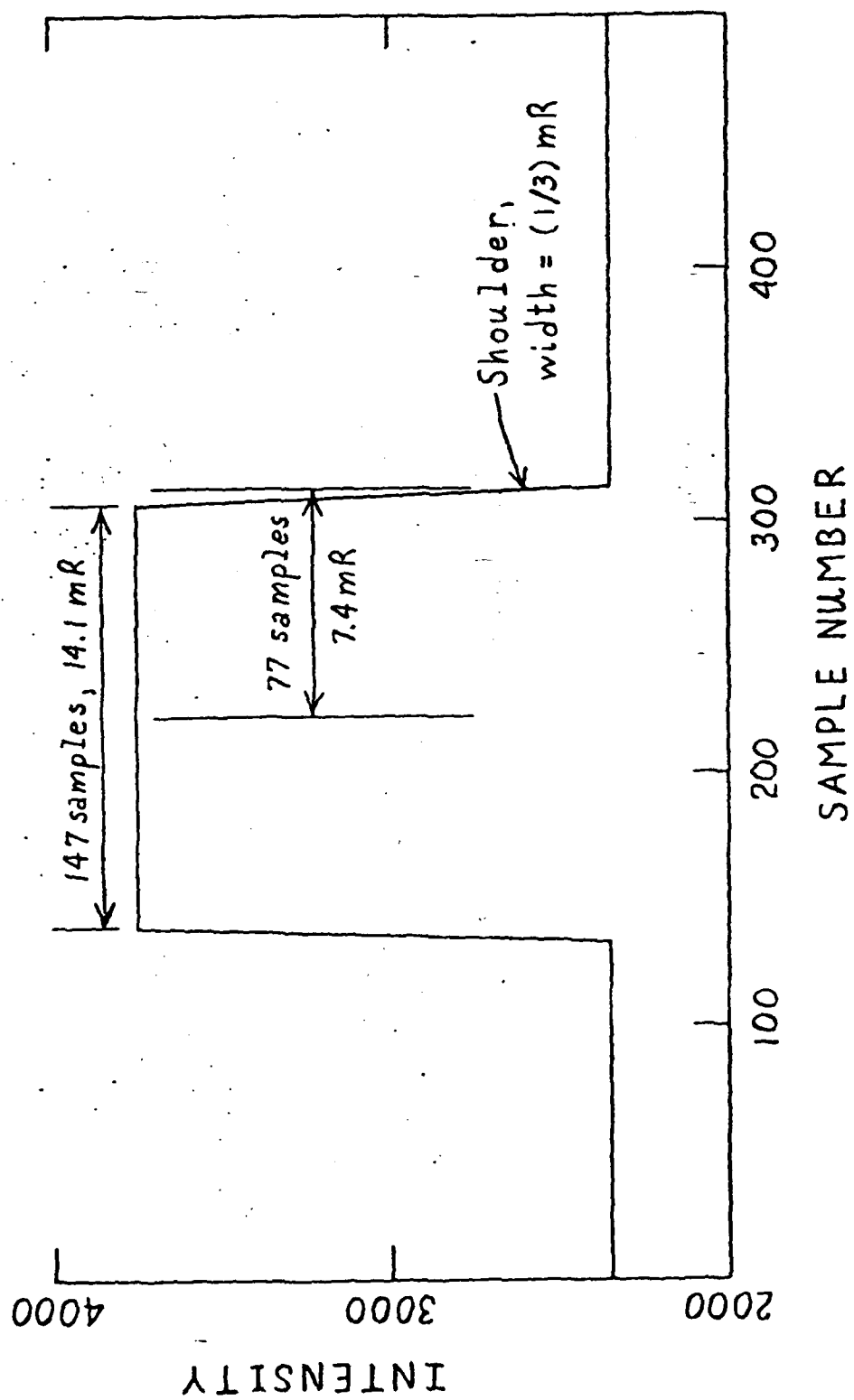


FIGURE 2: IDEAL PULSE PRODUCED BY TRUE IMAGE

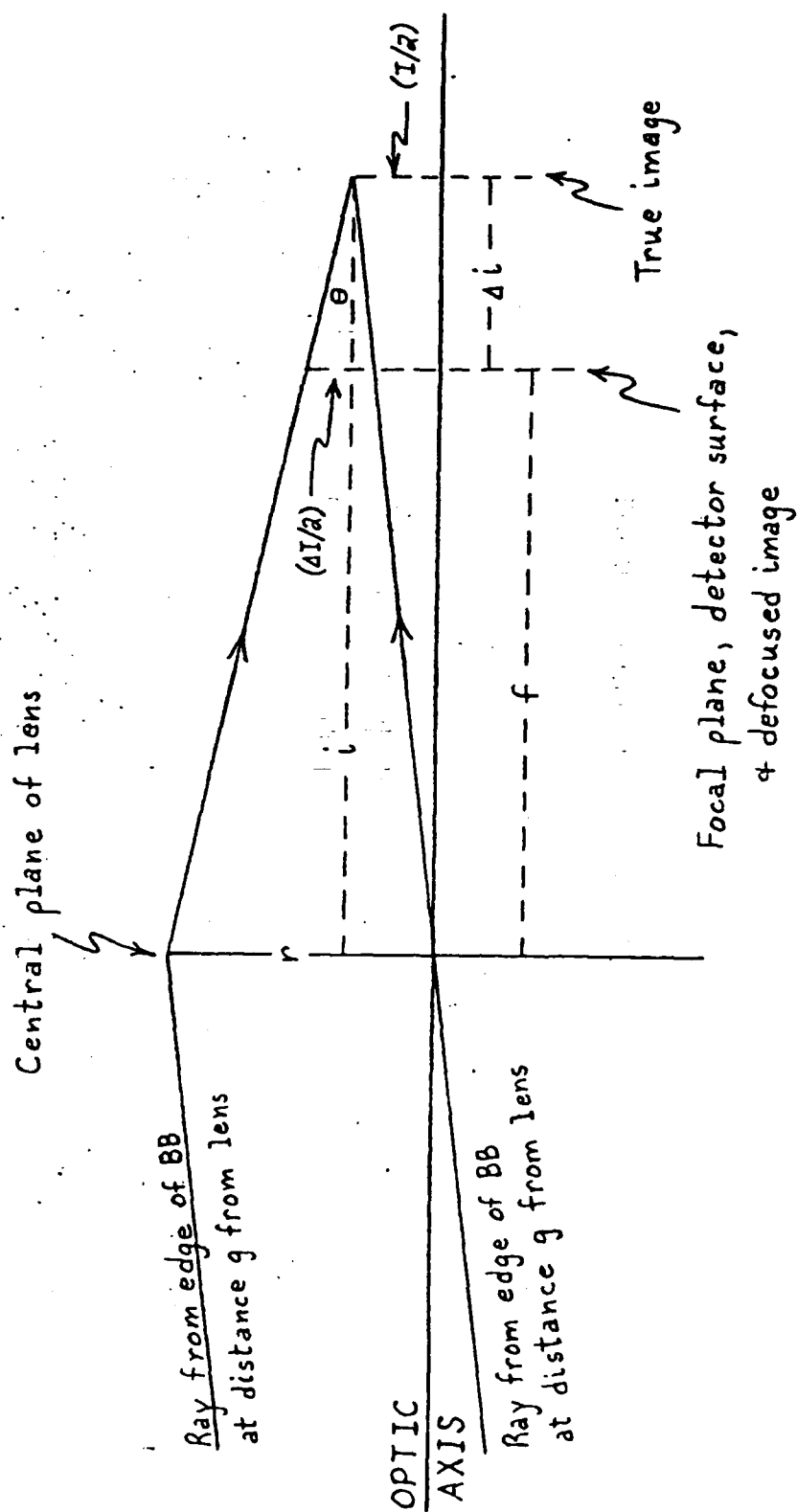


FIGURE 1: SCHEMATIC OPTICAL GEOMETRY

and, if so, whether corrections can be made which allow true pulse heights to be computed.

If true pulse heights can be determined, the next step is to calculate the external BB radiance at the lens using the LOWTRAN atmospheric transmission and emission model. This radiance and the true pulse heights constitute one calibration point. The internal BB radiance and the heights of the internal reference pulses provide another, but not directly because the internal BB radiance is relayed to the detector by one optical system, the external BB radiance and the scene radiance by another, and the two optical systems transmit and emit differently. Thus, the internal BB radiance must be corrected once to obtain radiance on the detector, and a second time to obtain the equivalent radiance at the sensor aperture. The sensor response to scene radiance can then be derived from the calibration points.

Note that this procedure gives two values for responsivity but none for reference radiation. Perhaps the latter can be estimated from the closed cover scans; this remains to be seen.

and centers of the pulses had different but regularly varying widths. Unfortunately, the pulses on some channels at other elevations look very different, e.g., compare Figure 3 with Figure 4, and Figure 5 with Figure 6. If the amplifier for MW channel 1 was working properly, the pulse shape in Figure 5 must have resulted from some combination of non-uniform flux distribution and maladjustment of factors (2) - (4) above. At this time only one set of LW calibration pulses and two of MW pulses have been plotted. This is not enough to determine more precisely the cause of the deformed pulses in Figures (4) and (5).

For calibration one needs to know the heights of the pulses that would be produced by the true image crossing the detector elements. Assuming conditions (1) - (3) and (6) are ideal, the true heights can be computed from

- (a) the heights and areas of the actual pulses,
- (b) the pixel size,
- (c) the optical parameters,
- (d) the vertical position of the defocused image on the detector array, and
- (e) the flux distribution in the defocused image.

The flux distribution can be calculated if the radiance is uniform over the true image area and isotropic over the range of solid angle within the illuminated volume of the optical system. In that case the calculation amounts to computing the projected true-image area which receives radiation from a point of the defocused image. If other conditions are ideal as assumed, the vertical position of the defocused image can be inferred from the flux distribution and the actual pulse shapes. At Montauk Point, however, one or more of the other conditions may not have been ideal. Plots of all calibration scans at Montauk must be inspected to determine whether any conditions were in fact non-ideal

- (5) the flux distribution in the defocused image, and
- (6) the response of the electronics.

The first factor can be ignored for present purposes; the blackbody temperature is known to be uniform in comparison to the effects of other factors. The amplifiers for the LW array are ac coupled with a 0.5 Hz, 3 dB cut-on frequency; those for the MW array are dc coupled. The 3 dB cut-off frequency for both sets of amplifiers is 1 kHz (1 ms time constant). The spinning mirrors for the internal reference source are shaped so that full response to its radiation is achieved, but only momentarily. Before each scan the amplifier outputs are clamped with the detectors viewing themselves.

Assume conditions (1) - (3) above are ideal and the true image is focused on and vertically centered on the detector array. Then in principle the BB pulse from the dc coupled amplifiers appears as in Figure 2. The pulse from the ac coupled amplifiers is the same except that its top droops slightly, and there is a slight undershoot after the pulse. Some of the actual pulses (Figures 3 and 6) resemble the ideal pulses, but they have wider bases, wider shoulders, and narrower tops. The wider bases result from the increased width of the defocused image as explained. The wider shoulders and narrower tops can be explained by a non-uniform flux distribution across the width of the defocused image. The droop of the pulse top in Figure 3 is only 4 per cent greater than that expected from the cut-on frequency of the ac coupled amplifiers, but the droop in Figure 4 is more than twice as great, and the top has an unexpected upward bow.

If the pulses on all channels had the same base widths and appearance as those in Figures 3 and 6, the results could be explained by the size and non-uniform flux distribution of the defocused image, even if the shoulders

at which distance $(\Delta I/I) = 0.3369$. At the actual distance of 70 ft. $(\Delta I/I) = 0.3381$, so at Montauk Point the BB was about as far from the radiometer as it profitably could have been from the standpoint of image size. (From the standpoint of flux uniformity in the image, moving the BB farther away might or might not have improved matters. The equations for image size say nothing about this; it must be studied separately.) With respect to image size, there are only three ways to improve upon the Montauk Point conditions: use a "collimator," use a larger blackbody, or reduce the sensor aperture with a removable stop for calibration.

(However, it might be possible to cure the radiometer's far-sightedness with spectacles, a related technique.)
The disadvantage of a collimator has already been noted. [^] With a larger BB, temperature uniformity is harder to achieve. In addition a larger BB may not be commercially available and is probably expensive if it is available. Cost is all the more critical because at least two sources are needed. If the aperture is reduced for field calibrations, it will be different from that for laboratory calibrations and field measurements. (Recall the similar disadvantage of the Jones method.) On the other hand, the purpose of the field calibration is to link the radiometer's field response to the laboratory calibration. An aperture stop should be used if, by reducing defocusing effects, it strengthens the link. This would have to be determined experimentally. The stop could be a small hole in the aperture cover.

Discussion of BB Pulse Shape and Calibration Analysis

The shapes of the BB pulses are affected by

- (1) the BB temperature distribution,
- (2) orientation of the BB relative to the scan direction,
- (3) alignment of the optics and detectors,
- (4) vertical positioning of the BB image on the detector array,

This is positive for $G < 2r$, zero for $G = 2r$, and negative for $G > 2r$. Thus, as the BB is moved away from the radiometer, the ratio $(\Delta I/I)$

increases to $(2r/G)$ if $G < 2r$.

remains equal to $(2r/G)$ if $G = 2r$.

decreases to $(2r/G)$ if $G > 2r$.

Obviously there are conditions for which $(\Delta I/I) = 0$. In this case

$$g = f \left(1 - \frac{G}{2r} \right).$$

If $G < 2r$ the object must be inside the focus and the image virtual for $(\Delta I/I) = 0$. This result is related to both the close extended source and Jones calibration methods. Its implications will not be considered here.

If $G > 2r$ a virtual object is required for $(\Delta I/I) = 0$. This is achieved with a collimator. (Here "collimator" is a misnomer since the device forms an image, not a parallel beam.)

With a distant extended source $G > 2r$, so moving the BB away from the sensor reduces the fractional enlargement of the defocused image, but very slowly at large object distances and not below $(2r/G)$. In any case the object distance is limited by the object size since the true image must fill or overfill the field of view, preferably by two or more times to make positioning of the image on the detector less critical. In order to satisfy this overfill requirement, the distance to the BB at Montauk Point could not have exceeded

$$g = \frac{G_v}{2(TFOV_v)} + f = 1311 \text{ in.} = 94 \text{ ft.},$$

BLACKBODY CALIBRATION OPTIONS

+ : Advantage 0 : Neutral - : Disadvantage ? : Uncertain

Source Location and Size Selection Criteria	Distant		Near	
	Small	Large	Small	Large
Focus not required	-	-	+	+
Atmospheric attenuation	-	-	+	+
Stray background radiation	-	+	-	+
Aperture filled	+	+	-	+
Direct radiance responsivity	-	+	+	+
Source availability	+	?	?	+
Whole array illuminated	-	?	+	+
Ease of handling & control	-	-	0	+
Positioning not critical	0	0	-	+

STANDARD SOURCE

SPECIFICATIONS

AREA: 10 IN. HORIZONTAL (MINIMUM)
10 IN. VERTICAL (MINIMUM)

TEMPERATURE RANGE: -20 TO 50 °C (253-323 °K)
MODIFIABLE TO -50 °C (223 °K)

UNIFORMITY: 0.1 °C DESIRED (SOME NON-UNIFORMITY
NEAR EDGES ALLOWED)

TEMPERATURE READOUT RESOLUTION: 0.1 °C

ANALOG CONTROLLER ACCEPTABLE

MAKERS

ADVANCED KINETICS

DBA SYSTEMS

BARNES ENGINEERING

ELECTRO-OPTICAL INDS.

BLOCK ENGINEERING

EPPLEY LABORATORY



TYPES OF CALIBRATIONS

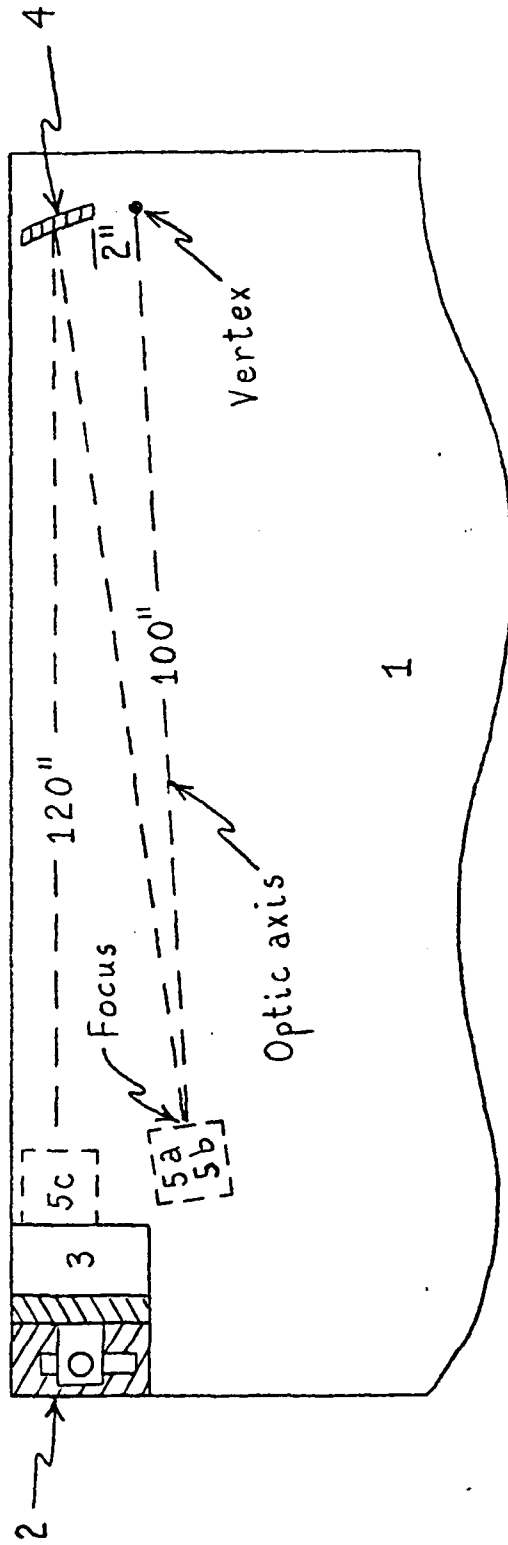
NEI AND SPATIAL RESPONSE
(POINT AND BAR SOURCE SCANS)

RADIOMETRIC RESPONSE
(NEAR EXTENDED SOURCE SCANS)



LABORATORY CALIBRATION SET-UP

Top View (not to scale)



1. Optical bench
2. Movable stage, horizontal & vertical micrometer adjustments
3. Radiometer
4. Off-axis paraboloid, 10" dia., 100" f.l.
5. Blackbody source
 - a. EOI model HS 153, 4.7 mil aperture
 - b. EOI model P1406S1 with 6 bar target
 - c. EOI model P1406S1 w/o 6 bar target

LABORATORY CALIBRATION PROCEDURE

1. POINT SOURCE SCANS
 - A. CENTER POINT-SOURCE IMAGE VERTICALLY ON PIXEL.
 - B. RECORD 4 FRAMES.
 - C. DO A-B FOR ALL CHANNELS OF DETECTOR ARRAY.
 - D. DO A-C FOR BOTH ARRAYS.

2. BAR SOURCE SCANS
 - A. CENTER BAR TARGET VERTICALLY ON DETECTOR ARRAY.
 - B. RECORD 4 FRAMES IN ALTERNATING MODE (2 FRAMES FROM EACH DETECTOR).
 - C. DO A-B WITH BARS AT 10, 20, 30, 40, 50 °C.

3. NEAR EXTENDED SOURCE SCANS
 - A. REMOVE BAR APERTURES FROM SOURCE.
 - B. PLACE SOURCE CLOSE TO TELESCOPE OBJECTIVE LENS.
 - C. RECORD 4 FRAMES.
 - D. DO C WITH SOURCE AT 10, 20, 30, 40, 50 °C.

4. DO 1-4 WITH RADIOMETER AT 20, 25, 30, 35, 40 °C.



MW POINT SOURCE RESULTS

Site & date	Lab, 23/8/84		Field, 12/9/84	
Radiometer temperature (°C)	20.6		26.7	
Channel	2	3 4	7 8	9
Full width half max. (mR)	0.55	0.39 0.76	0.41 0.38	0.40
Amplitude (arbitrary units)	66.7	948 25.2	266 2253	304
Cross-channel coupling (dB) (%)	-23	* -32	-19 *	-17
	7.0	* 2.7	12 *	14

* = image vertically centered on channel

Point source subtense = 0.05 mR

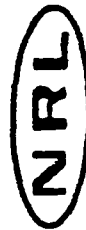


LW POINT SOURCE RESULTS

Site & date	Lab, 23/8/84		Field, 12/9/84	
Radiometer temperature (°C)	20.6		27.3	
Channel	2	3 4	7 8	9
Full width half max. (mR)	0.72	0.35 0.39	0.48 0.34	0.49
Amplitude (arbitrary units)	4	184 12	19 562	31
Cross-channel coupling (dB) (%)	-33	* -24	-29 *	-25
	2.3	* 6.5	3.4 *	5.5

* = image vertically centered on channel

Point source subtense = 0.05 mR



FIELD CALIBRATION PROCEDURE

1. POINT SOURCE SCANS
 - A. CENTER IMAGE FROM PORTABLE COLLIMATOR VERTICALLY ON PIXEL.
 - B. RECORD 4 FRAMES.
 - C. DO A-B FOR CHANNELS 2, 8, 15 OF DETECTOR ARRAY.
 - D. DO A-C FOR BOTH ARRAYS.
2. NO BAR SOURCE SCANS.
3. NEAR EXTENDED SOURCE SCANS
 - A. SAME PROCEDURE AS IN LABORATORY.
 - B. RECORD SCANS AT END OF EACH DATA TAPE.



CALIBRATION ISSUES & PROBLEMS

POINT RESPONSE

NEW MW DETECTOR GEOMETRY

VERTICAL REGISTRATION OF MW & LW DETECTORS

DEPENDENCE OF POINT-IMAGE SIZE & SHAPE ON TEMPERATURE

DEPENDENCE OF CROSS-CHANNEL COUPLING ON TEMPERATURE

MUST 10" PARABOLOID BE CENTERED ON RADIOMETER TELESCOPE FOR
POINT-RESPONSE MEASUREMENTS?

COMPARISONS BETWEEN LAB & FIELD MEASUREMENTS



CALIBRATION ISSUES & PROBLEMS

RADIOMETRIC RESPONSE

CALIBRATION EQUATION: $(V - V_0) / (V_H - V_0) = AR + B$

LW HOT REFERENCE SATURATES AT RADIOMETER TEMPS $> \sim 30^\circ\text{C}$.

DAS PROBLEMS: INTERNAL HOT &/OR COLD REFERENCES MISSING IN
SOME CASES

CAN RADIOMETRIC CALIBRATIONS BE MADE IN THE FIELD? (YES)



CALIBRATION ISSUES & PROBLEMS

MISCELLANEOUS

IS CHANNEL 12 OF LW ARRAY FAILING?

MUST RADIOMETER TEMPERATURE BE LIMITED?

POINT-IMAGE DISTORTION AT HIGH TEMPERATURE?

INCREASED CROSS-CHANNEL COUPLING AT HIGH TEMPERATURE?

LW COLD CLAMP MAY NOT WORK AT HIGH RADIOMETER & CALIBRATION TEMPERATURES.

HOT REFERENCE PULSE MAY NOT BE IDENTIFIABLE AT HIGH RADIOMETER & CALIBRATION TEMPERATURES.



DAS ISSUES AND PROBLEMS

DATA STORAGE ("BLOCK") ERRORS

DATA RETRIEVAL ("BIT") ERRORS

SLIPPAGE OF DATA ACQUISITION WINDOW
OR INTERNAL REFERENCE MIRRORS



PLOTS ILLUSTRATING ISSUES & PROBLEMS

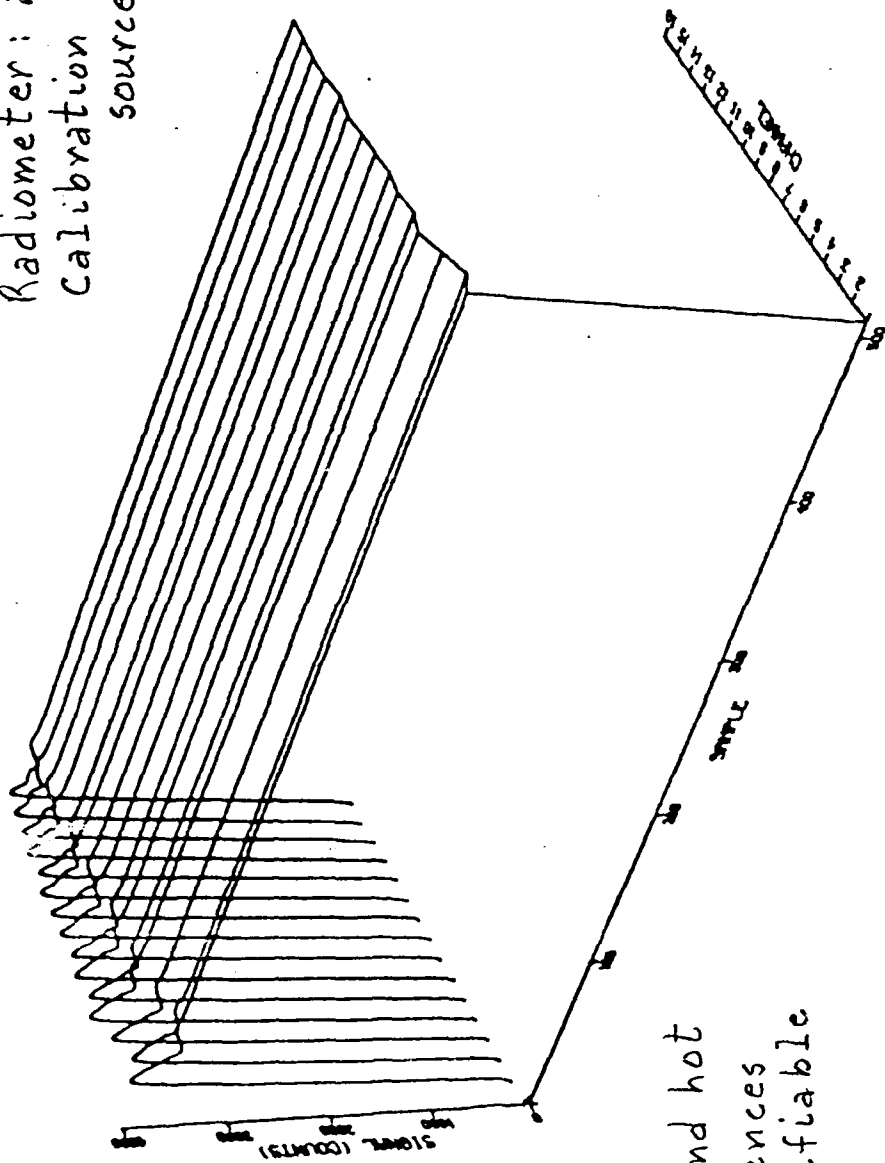


BEDFORD MA., 23 AUG 1984

TAPE : 1 , MODE : LW , FRAME : 216

3 DAYS, 12 HOURS, 25 MIN, 50.8 SEC

Radiometer: 20.6 °C
Calibration source: 50 °C



Cold and hot
references
identifiable

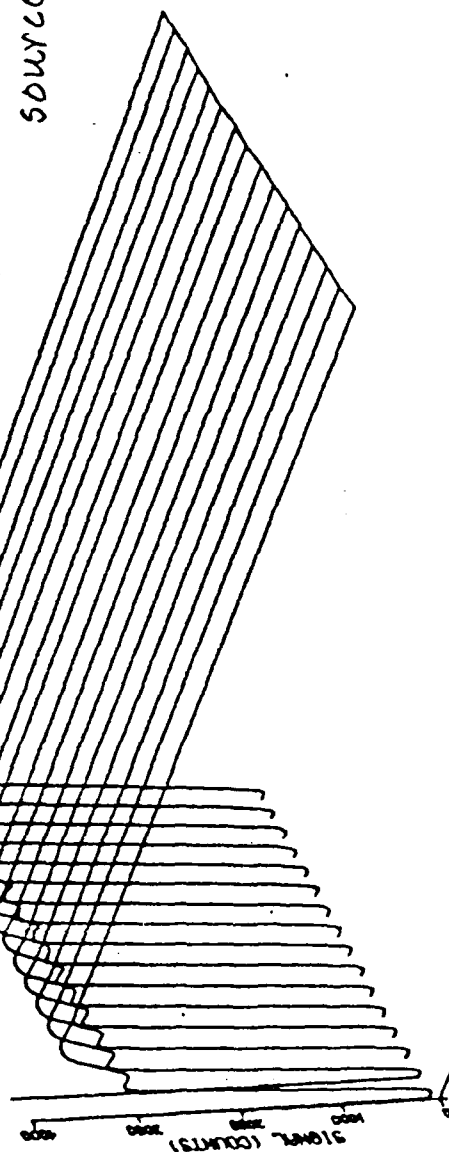
NRL

BEDFORD MA., 23 AUG 1984

TAPE : 5 , MODE : MW , FRAME : 182

3 DAYS, 17 HOURS, 20 MIN, 17.3 SEC

Radiometer: 40.1 °C
Calibration
source: 50 °C

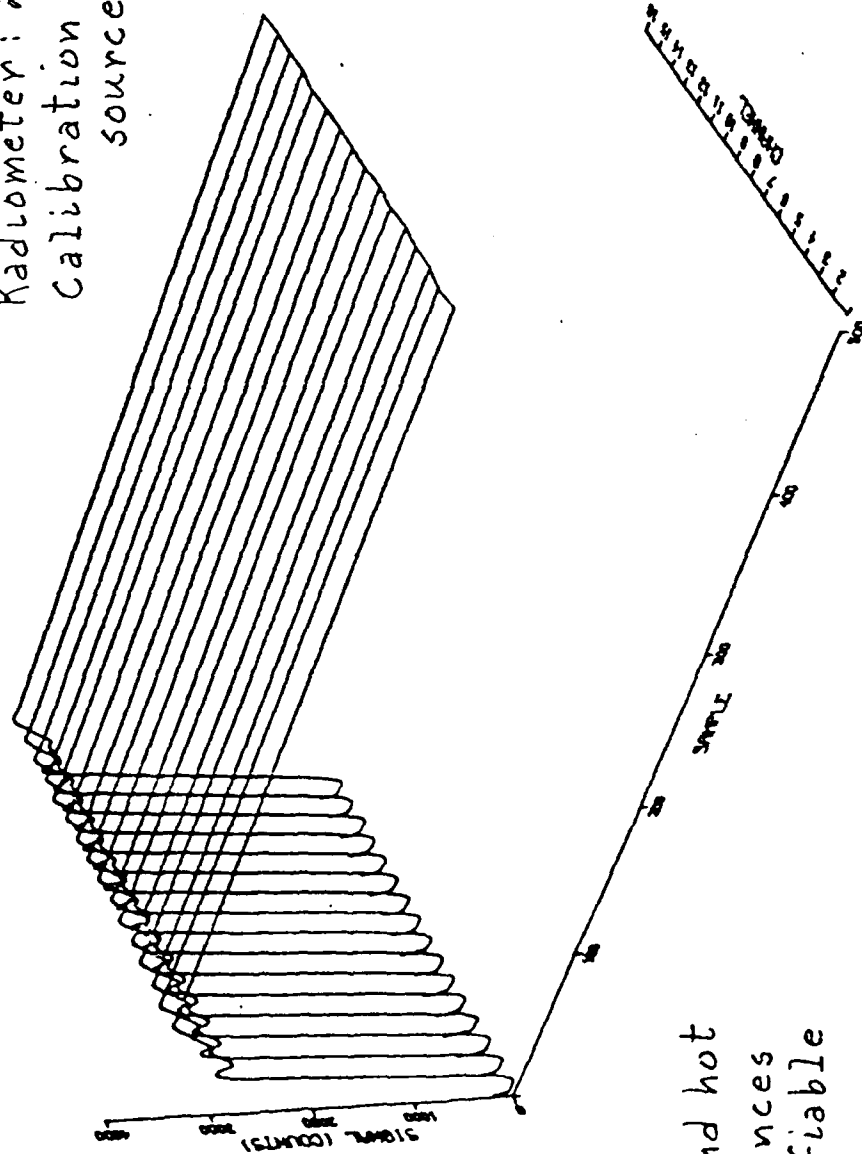


Cold reference
identifiable
Hot reference
obscured?



BEDFORD MA., 23 AUG 1984
TAPE : 1 , MODE : MW , FRAME : 178
3 DAYS, 12 HOURS, 13 MIN, 50.3 SEC

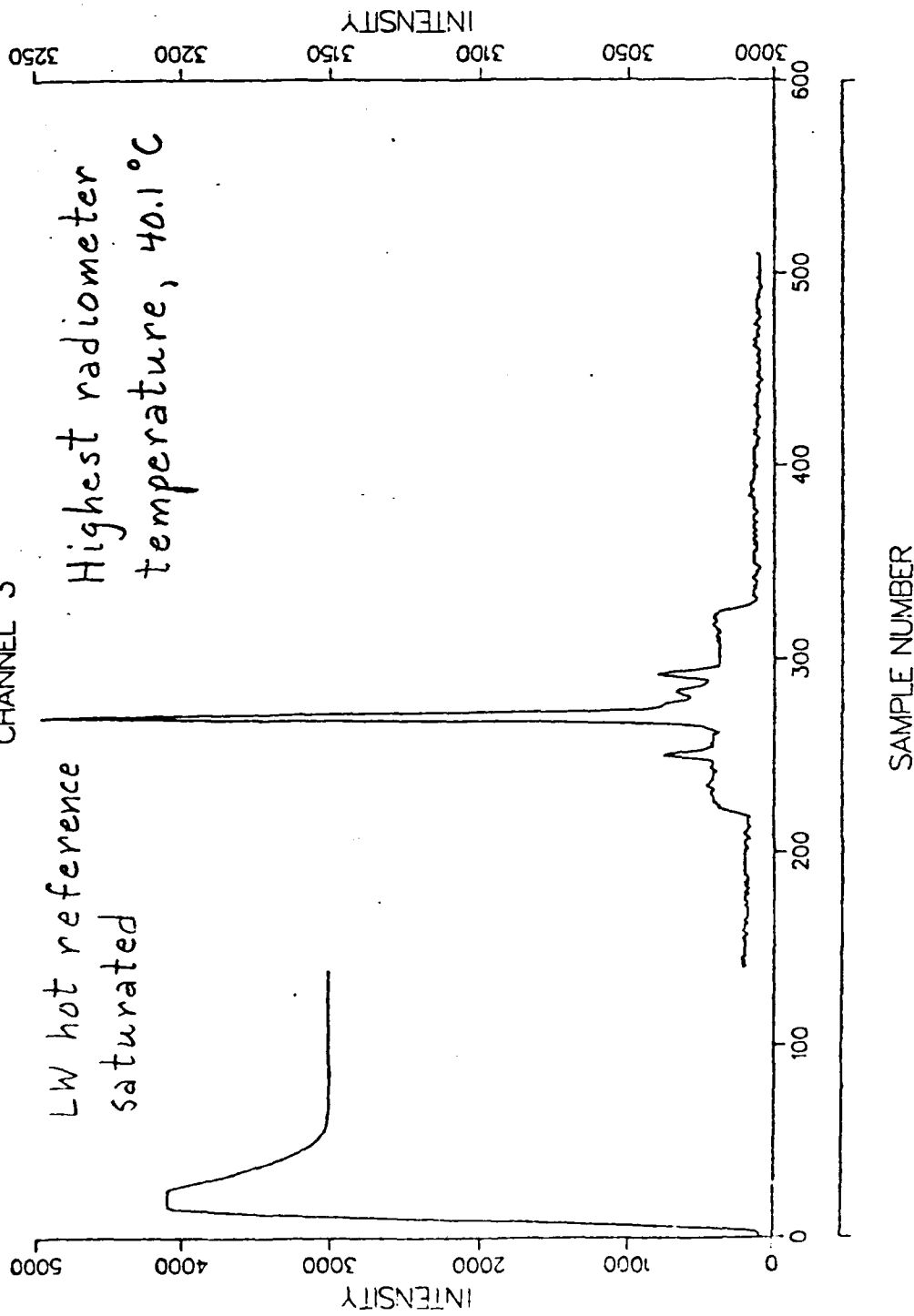
Radiometer: 20.6°C
Calibration
source: 50°C



Cold and hot
references
identifiable

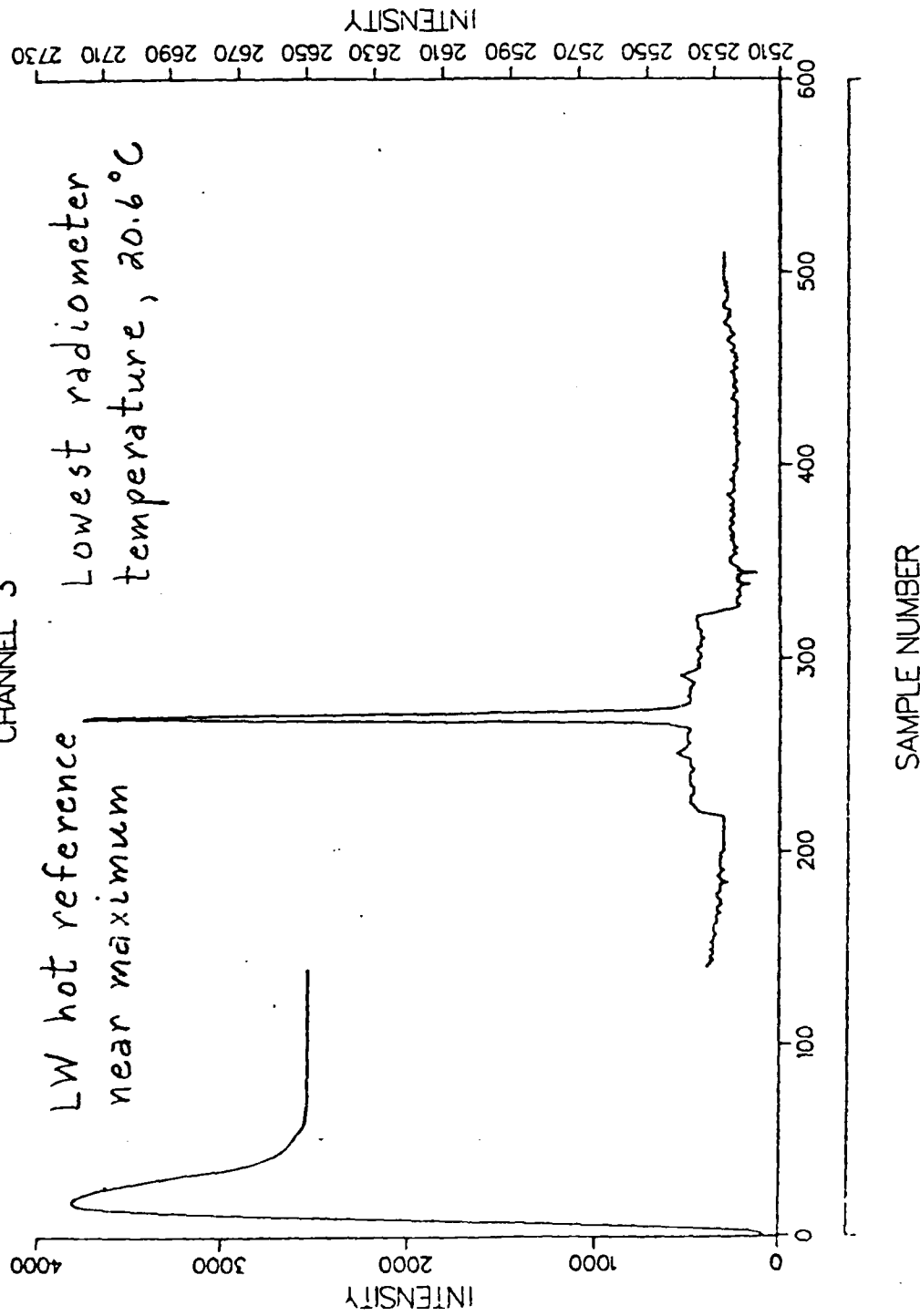
NRL

POINT SOURCE DATA AUG 23, 1984
TARGET TEMPERATURE: 227.0 C OPTICS TEMPERATURE: 104.1 F
3 DAYS 17 HOURS 8 MINUTES 50.3 SECONDS
CHANNEL 3



NRL

POINT DATA AUG 23, 1984
TARGET TEMPERATURE: 227.1 C OPTICS TEMPERATURE: 69.0 F
3 DAYS 11 HOURS 49 MINUTES 55.8 SECONDS
CHANNEL 3



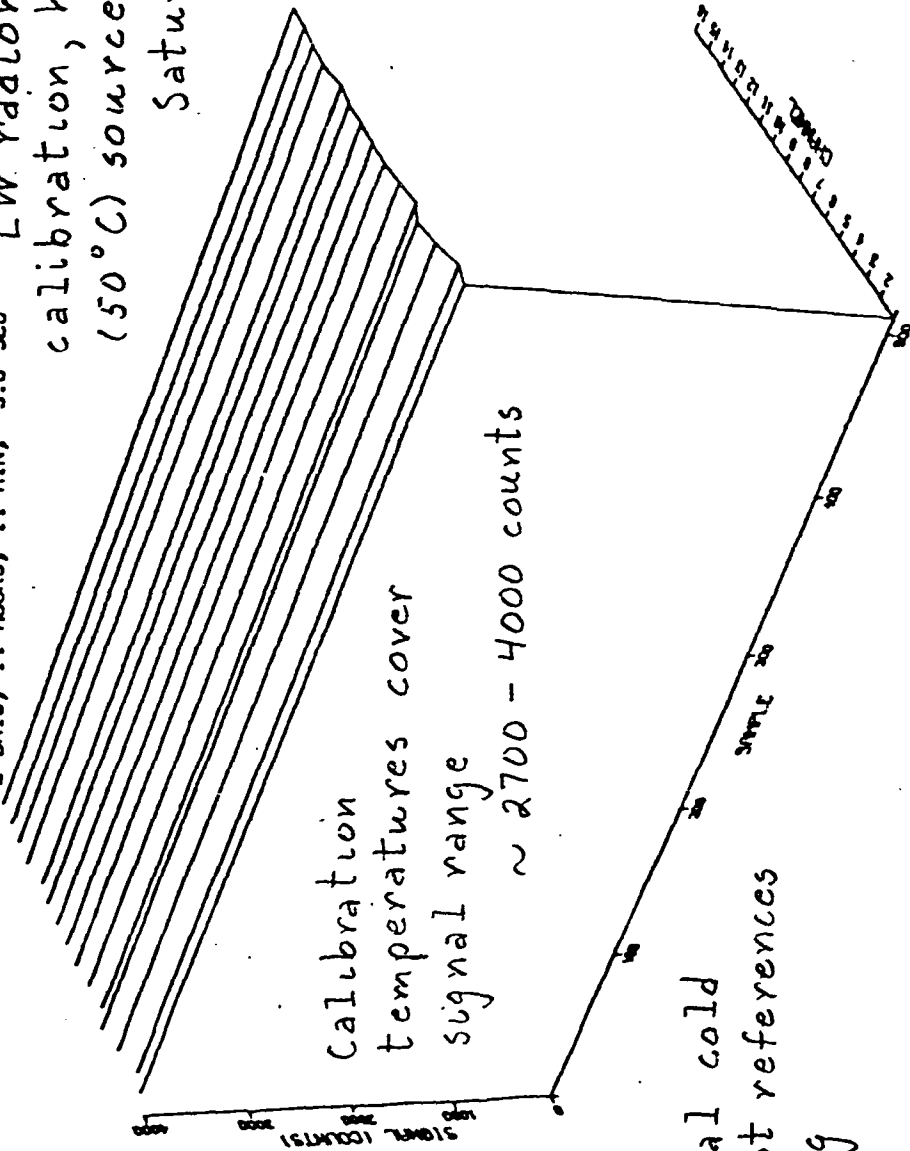


BEDFORD MA., 12 SEPT 1984

TAPE : BF4, MODE : LW , FRAME : 460

2 DAYS, 14 HOURS, 14 MIN, 3.8 SEC LW radiometric
calibration, hottest
(50°C) source.

Saturated?



Internal cold
and hot references
missing

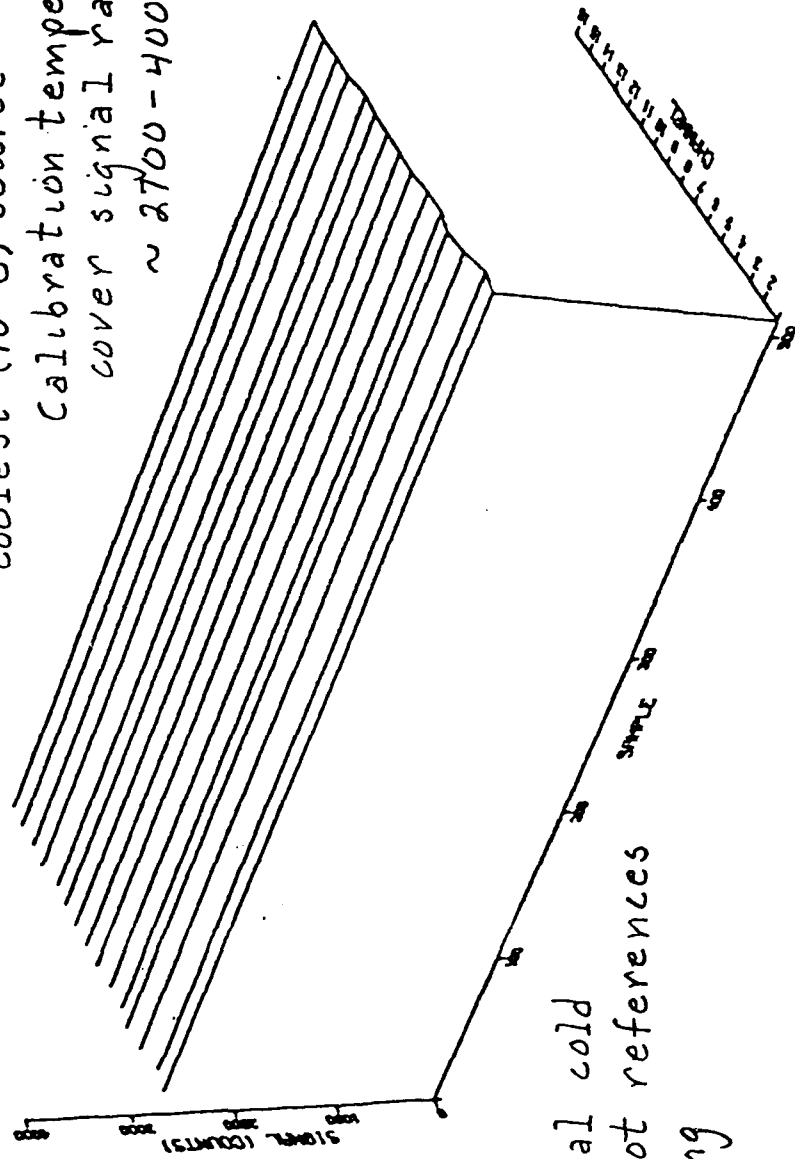


BEDFORD MA., 12 SEPT 1984

TAPE : BF4, MODE : LW , FRAME : 444

2 DAYS, 14 HOURS, 7 MIN, 48.3 SEC

LW radiometric calibration,
coolest (10°C) source
Calibration temperatures
cover signal range
~ 2700-4000 counts



Internal cold
and hot references
missing

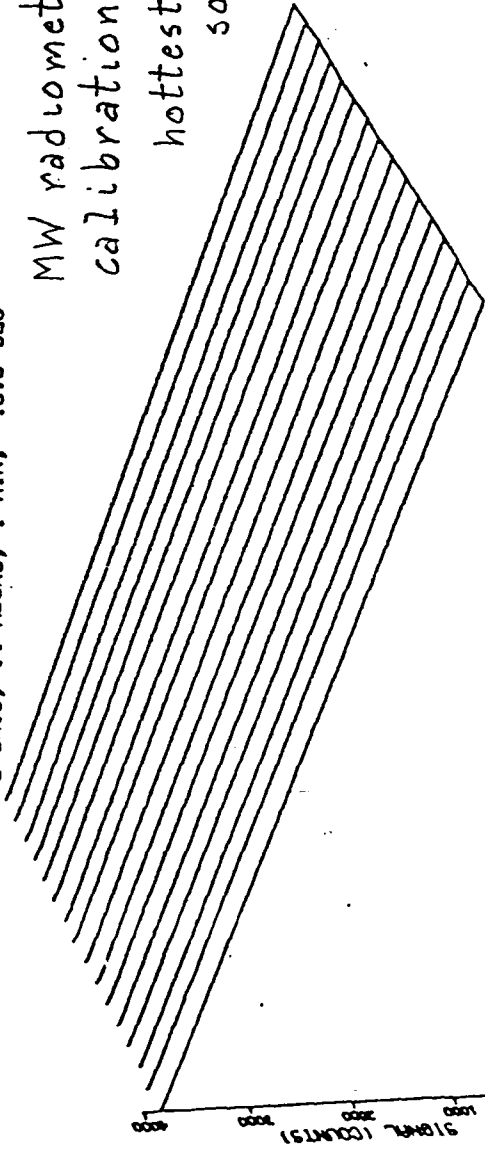
NRL

BEDFORD MA., 12 SEPT 1984

TAPE : BF4, MODE : MW , FRAME : 424

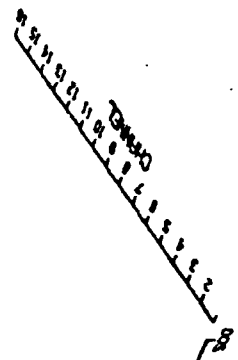
2 DAYS, 14 HOURS, 1 MIN, 16.3 SEC

MW radiometric
calibration,
hottest (50°C)
source



Calibration temperatures cover
signal range ~ 1300 - 3800 counts

Internal cold
and hot references
missing





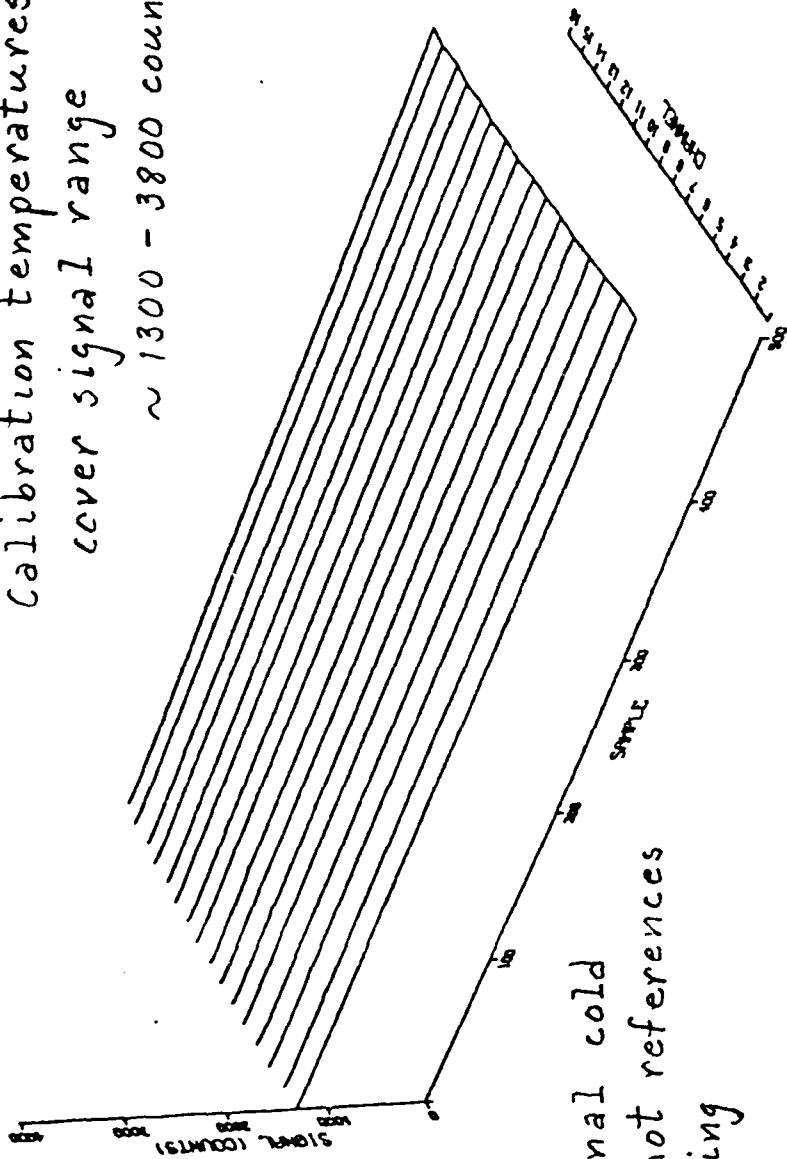
BEDFORD MA., 12 SEPT 1984

TAPE : BF4, MODE : MW , FRAME : 440

2 DAYS, 14 HOURS, 6 MIN, 30.3 SEC

MW radiometric calibration, coolest (10°C) source

Calibration temperatures
cover signal range
~ 1300 - 3800 counts

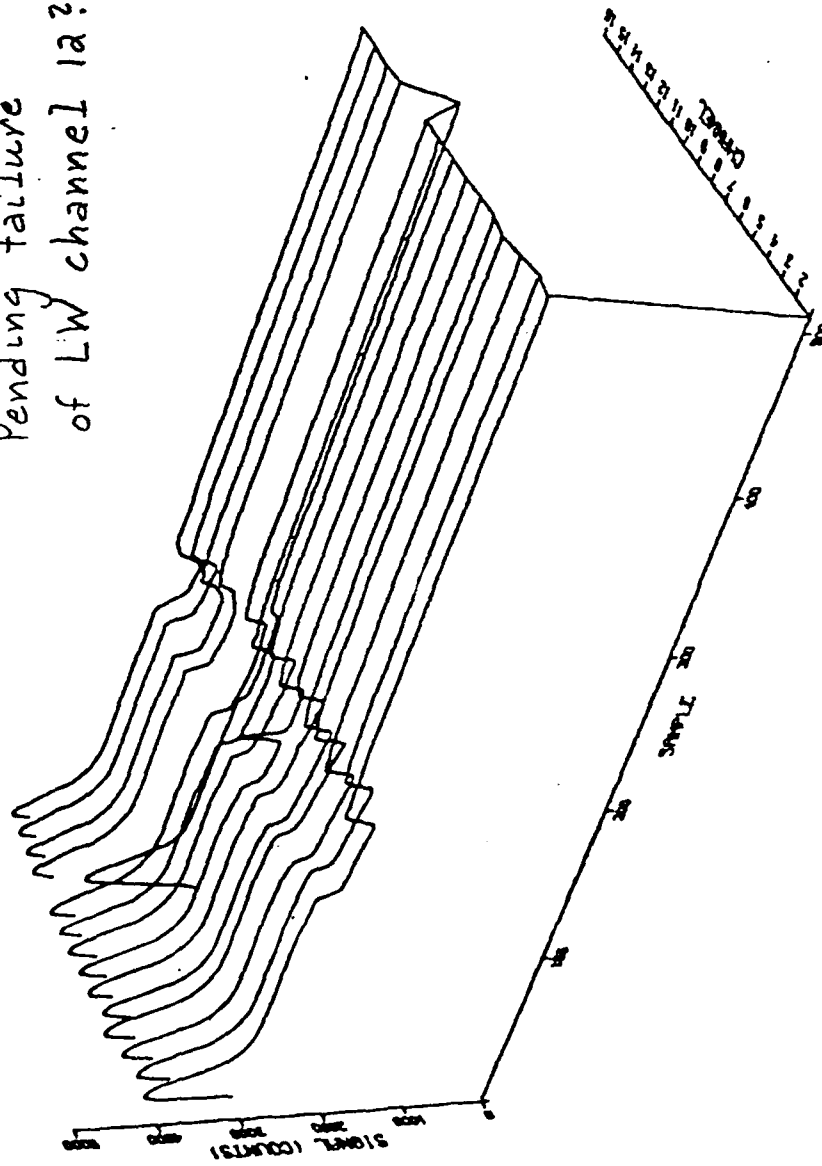


Internal cold
and hot references
missing



BEDFORD MA., 12 SEPT 1984
TAPE : BF4, MODE : LW , FRAME : 8
2 DAYS, 11 HOURS, 3 MIN, 32.8 SEC

Pending failure
of LW channel 1a?



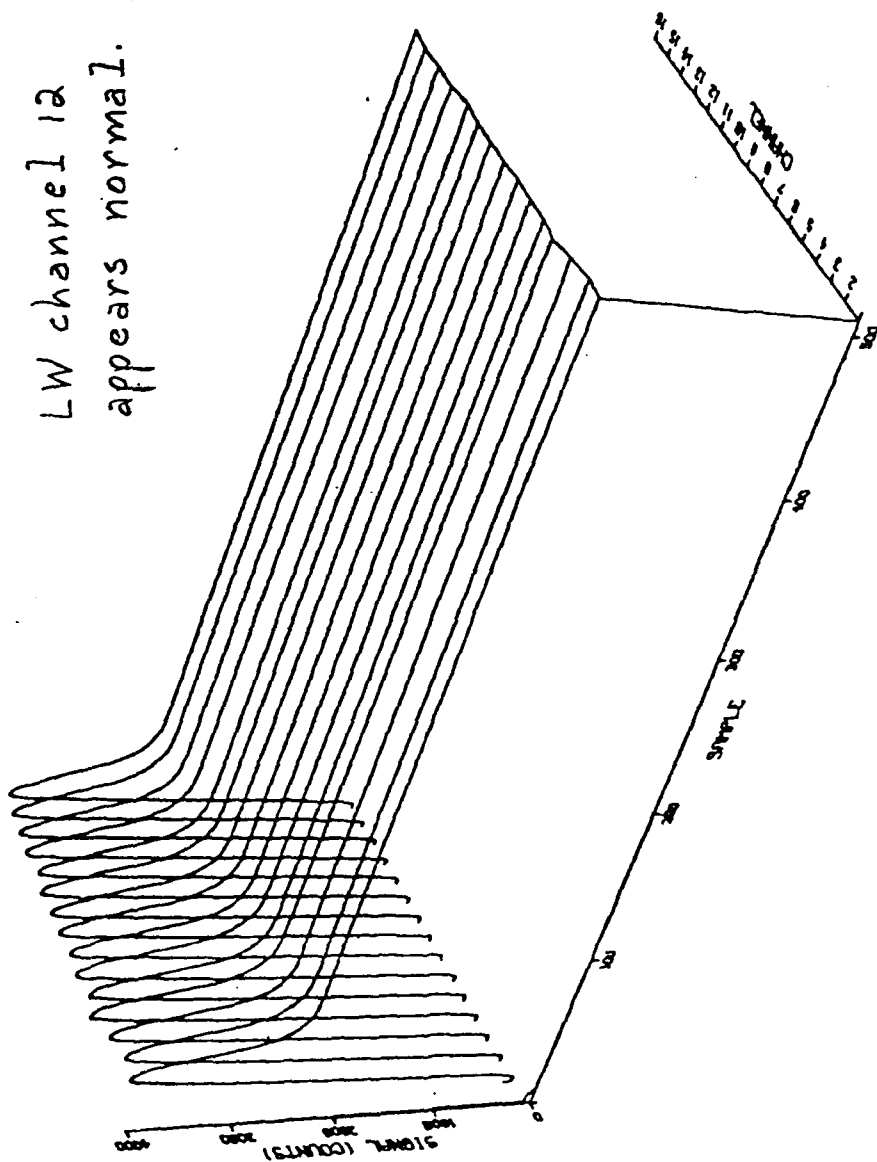


BEDFORD MA., 13 SEPT 1984

TAPE : BF7, MODE : LW, FRAME : 482

3 DAYS, 9 HOURS, 29 MIN, 31.8 SEC

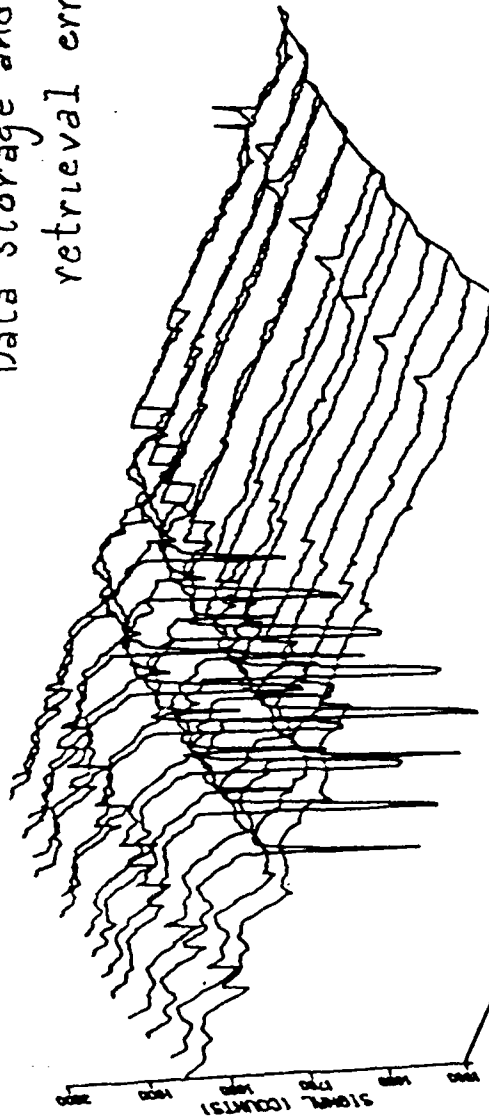
LW channel 12
appears normal.



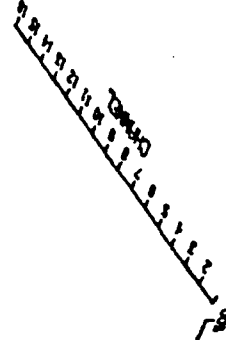


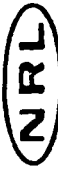
BEDFORD MA., 12 SEPT 1984
TAPE : BF4, MODE : MW , FRAME : 5
2 DAYS, 10 HOURS, 31 MIN, 35.8 SEC

Data storage and
retrieval errors



Slippage of
data acquisition
window or internal
reference mirrors





BEDFORD MA., 12 SEPT 1984

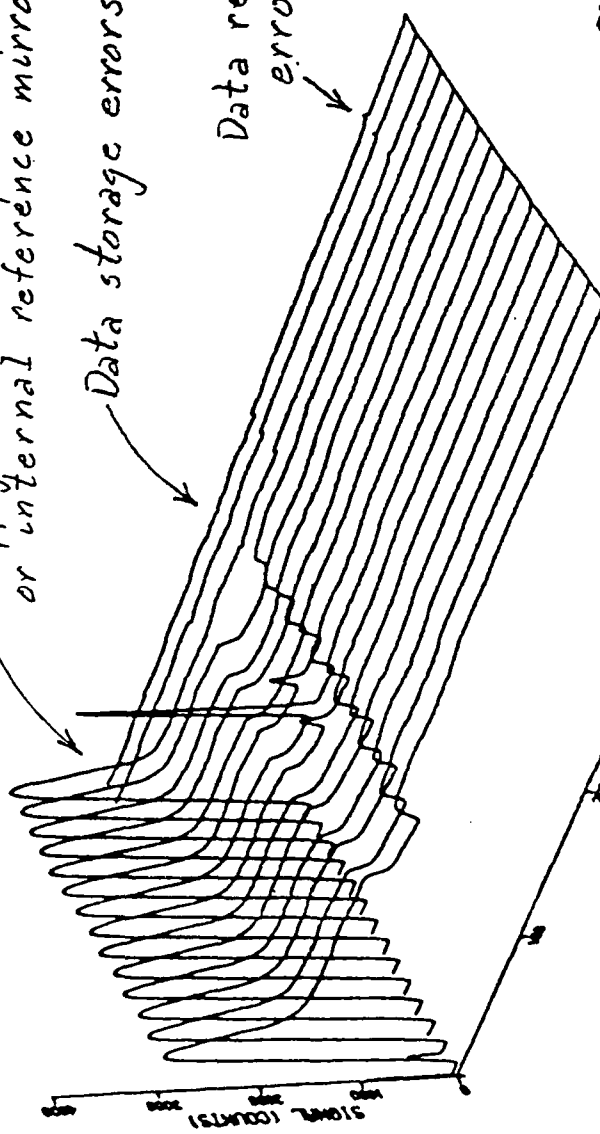
TAPE : BF4, MODE : MW , FRAME : 4

2 DAYS, 10 HOURS, 31 MIN, 35.3 SEC

Slippage of data acquisition window
or internal reference mirrors

Data storage errors

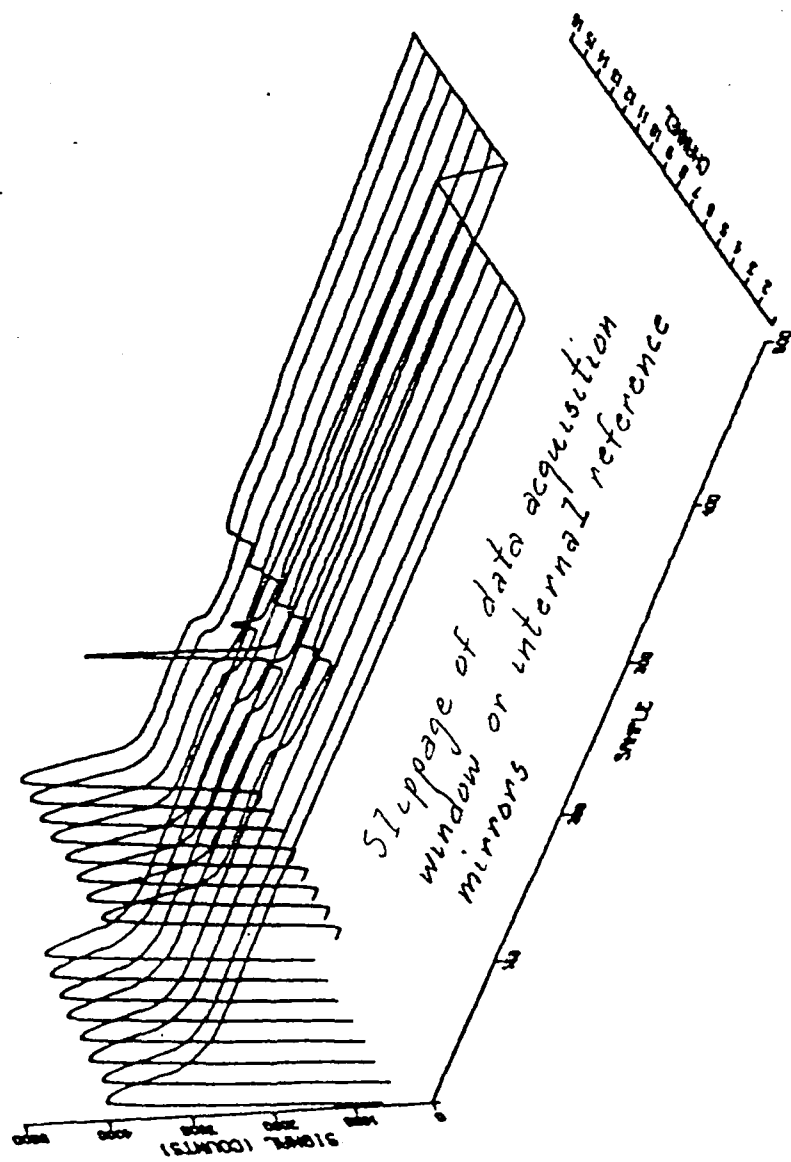
Data retrieval
errors?



Complete DAS
failure between
frames 4 and 5



BEOFORO MA., 12 SEPT 1984
TAPE : BF4, MODE : 8/8 , FRAME : 3
2 DAYS, 10 HOURS, 30 MIN, 42.3 SEC



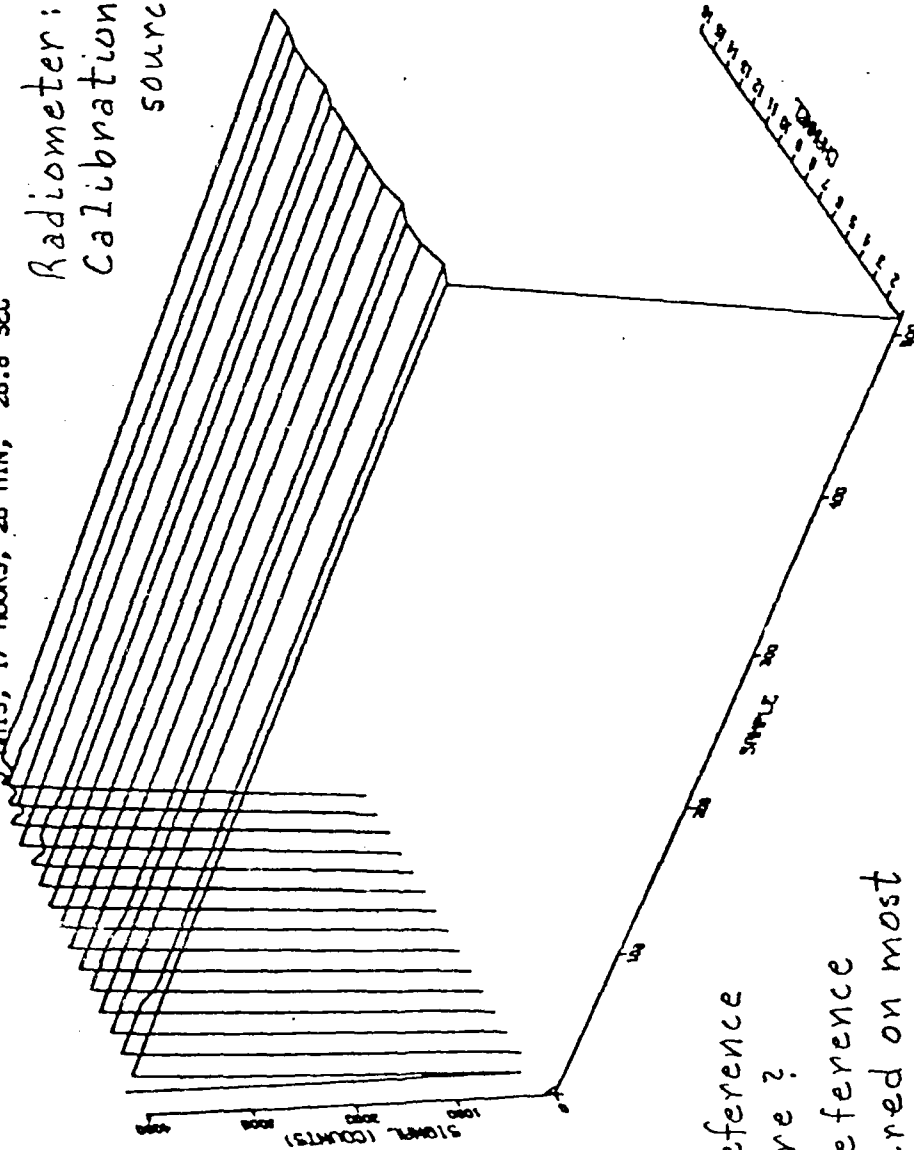


BEDFORD MA., 23 AUG 1984

TAPE : 5 , MODE : LW , FRAME : 218

3 DAYS, 17 HOURS, 28 MIN, 26.8 SEC

Radiometer: 40.1 °C
Calibration
source: 50 °C



Cold reference
failure ?
Hot reference
obscured on most
channels

MIDWAVE RADIOMETER CALIBRATION

The radiometer's response to monochromatic radiation will be derived first, then the analysis will be extended to broadband radiation. This will avoid hiding the essential features of the response in the fog of integration over the spectral band.

A. Monochromatic Response

Assume there is an analytic relation between the detector output voltage v and the electrical (E), optical (O), and thermal (T) parameters of the instrument and environment.

$$v = f(E, O, T) \quad (1)$$

If all parameters except radiance r on the detector are fixed,

$$v = g(r). \quad (2)$$

This relation can be expanded in a Taylor series

$$v = g(0) + g'(0)r + \frac{1}{2}g''(0)r^2 + \dots \quad (3)$$

The coefficients of the series are functions of all the system parameters except r and, therefore, are constants only if all

parameters except radiance on the detector are fixed. It will be assumed that the first two terms of the series adequately represent the voltage-radiance relation

$$v = g(0) + g'(0)r. \quad (4)$$

The detector output is dc coupled to an amplifier which multiplies it by a factor α and adds a voltage β , so that the voltage-radiance relation for the whole radiometer becomes

$$v = [\alpha g'(0)]r + [\alpha g(0) + \beta]. \quad (5)$$

The factors α and β are constant only if the electrical and thermal parameters of the system are fixed. The added voltage is chosen so that the radiometer output is v_0 when the detector is completely covered by a nearby mirror which rotates through the field of view. During the time of complete coverage, the radiance r_0 on the detector comes from emission by the mirror and reflection of the detector's own radiation back to it. Little or no stray radiation from the radiometer's interior reaches the detector at this time. The voltage-radiance relation with the cold reference mirror in place is

$$v_0 = [\alpha g'(0)]r_0 + [\alpha g(0) + \beta]. \quad (6)$$

The cold reference mirror is followed through the field of view by

another mirror mounted on the same motor shaft. This mirror reflects radiation from an internal reference source onto the detector. With the hot reference mirror in place, most of the radiance r_h on the detector comes from the internal source and the optics which transfer its radiation to the detector. However, radiation from the radiometer's interior is also reflected to the detector at this time. The peak hot reference voltage is

$$v_h = [\alpha g'(0)]r_h + [\alpha g(0) + \beta]. \quad (7)$$

The difference between the hot and cold reference voltages yields a relation for the amplification factor $[\alpha g'(0)]$.

$$v_h - v_o = (r_h - r_o)[\alpha g'(0)] \quad (8)$$

The radiometer is calibrated by measuring the voltage output with the total field of view overfilled by an extended source of radiance R placed close to the telescope's objective lens. Under these conditions the radiance on the detector is $(\tau R + r)$, where τ accounts for losses of source radiation in the main optics, and r for stray radiation from these optics and the radiometer's interior. With the standard source in view, the voltage-radiance relation is

$$v = [\alpha g'(0)](\tau R + r) + [\alpha g(0) + \beta] \quad (9a)$$

$$= [\tau \alpha g'(0)]R + [\alpha g'(0)r + \alpha g(0) + \beta]. \quad (9b)$$

Equation (9b) is a potential calibration equation. Another is obtained by subtraction of the cold reference voltage v_o .

$$v - v_o = [\tau \alpha g'(0)]R + (r - r_o) \alpha g'(0). \quad (10)$$

Division of this equation by the amplification factor of equation (8) gives yet a third calibration equation.

$$(v - v_o)/(v_h - v_o) = [\tau/(r_h - r_o)]R + [(r - r_o)/(r_h - r_o)] \quad (11)$$

This equation expresses the output voltage as a fraction of the output with the internal reference mirror in place, all voltages being measured above the cold reference level v_o .

Which of the three potential calibration equations is best? Equation (11), because it does not involve the response factors of the detector and electronics or, more precisely, accounts for them through v_o and v_h which are measured before each scan. Furthermore, the behavior of the slope and intercept in equation (11) can be predicted; this will provide a check of the calibration's success or failure and perhaps an indication of what went wrong in the event of failure. The difference $(r_h - r_o)$ will increase with temperature since r_h includes radiation from the internal reference optics and the radiometer's interior. However, radiation from the internal source accounts for most of r_h , so the increase of $(r_h - r_o)$ with temperature should be slow. This will result in a slow decrease of

the slope $[\tau/(r_h - r_o)]$ with temperature, provided the loss factor τ of the main optics depends weakly on temperature. The difference $(r - r_o)$ will increase with temperature more rapidly than $(r_h - r_o)$, since r comes entirely from the radiometer's interior and main optics. The intercept $[(r - r_o)/(r_h - r_o)]$ should, therefore, be more temperature dependent than the slope and should increase with temperature.

NRL FY85 BMAP ACTIVITIES

DATA CALIBRATION

AUG 84 LAB MEASUREMENTS (BEDFORD)

MUCH LEARNED

MW - LARGE OPTICAL COUPLING

LW - STABLE SINCE DEC 83 EMI MEASUREMENTS

DATA BEING USED TO DEVELOP CAL TECHNIQUE & SOFTWARE

HIGH RADIOMETER TEMP CREATES STRAY RADIATION PROBLEMS

QUESTIONS

POINT RESPONSE & OPTICAL COUPLING VS TEMP

RADIOMETRIC RESPONSE VS TEMP

MUST RADIOMETER TEMP BE $< 30^{\circ}\text{C}$?

SEPT 84 ROOFTOP MEASUREMENTS (BEDFORD)

ACCOMPLISHMENTS

NRL FIELD CAL PROTOCOL LOOKS GOOD

540 CALIBRATED BACKGROUND DATA FRAMES BEING DISSEMINATED

PROBLEMS

INTERMITTENT DAS ERRORS

SLIPPAGE OF INTERNAL REFERENCE OUTPUTS

JAN 85 LAB MEASUREMENTS (BEDFORD)

POINT & EXTENDED BLACKBODY MEASUREMENTS

IN TEMP-CONTROLLED ENVIRONMENT

INVESTIGATORS: LONGMIRE, SCHAU, SWEENEY, MCHUGH, LUCKE,
BEAVER



END

Part 3c

PART 3C

VUGRAPHS AND SUPPLEMENTAL TEXT FOR
OPTICAL SCIENCES DIVISION COLLOQUIUM, 17 JANUARY 1985

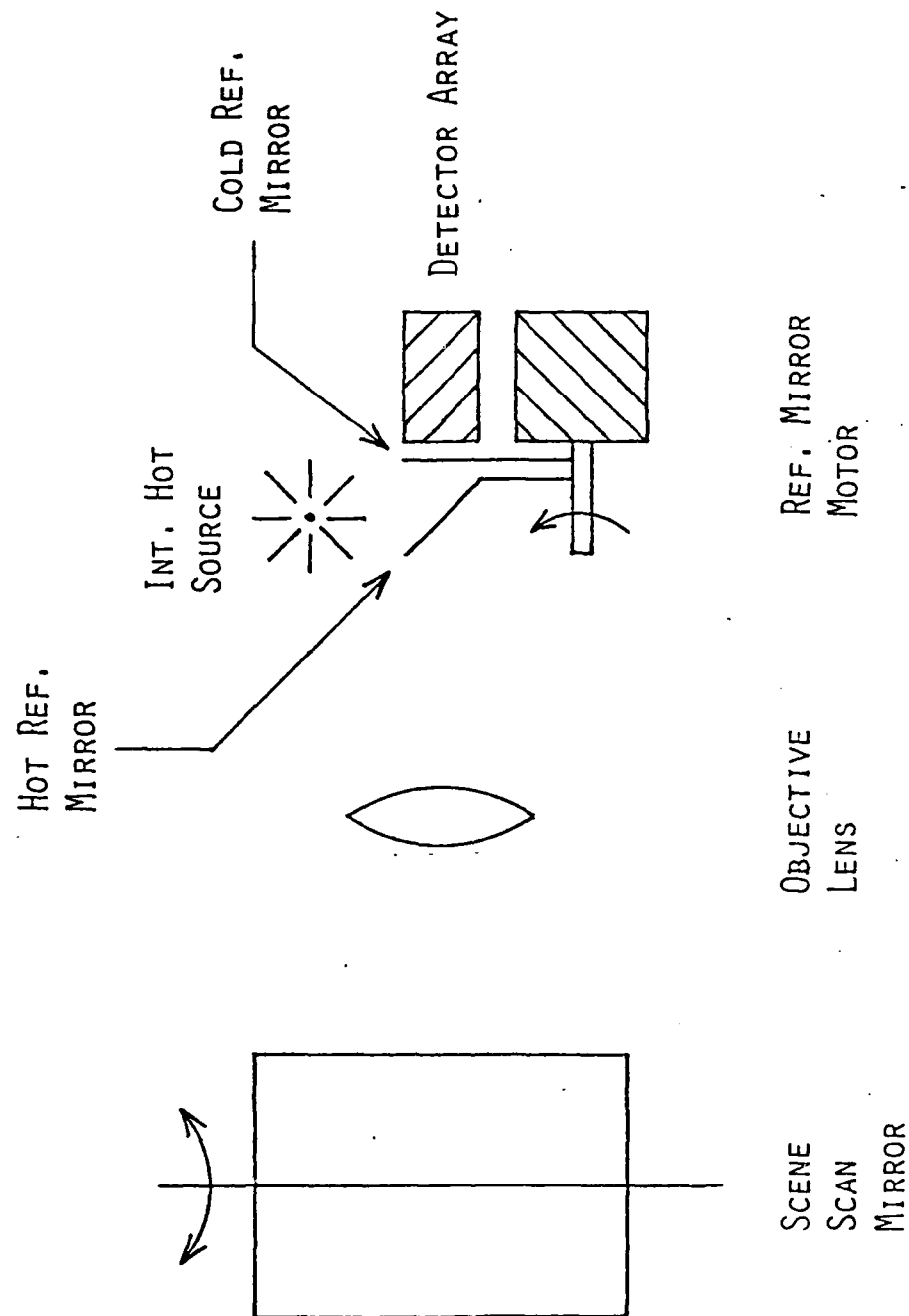
04 30 081

CALIBRATION

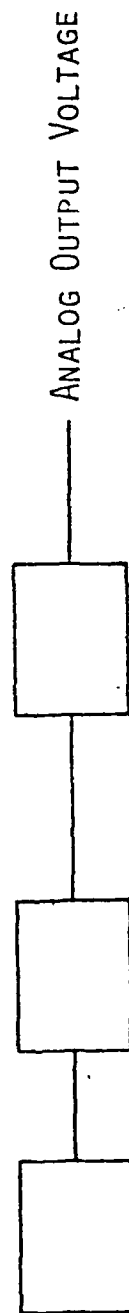
APPARATUS AND PROCEDURE

RESULTS AND DISCUSSION

RADIOMETER DIAGRAM



MIDWAVE ANALOG ELECTRONICS DIAGRAM

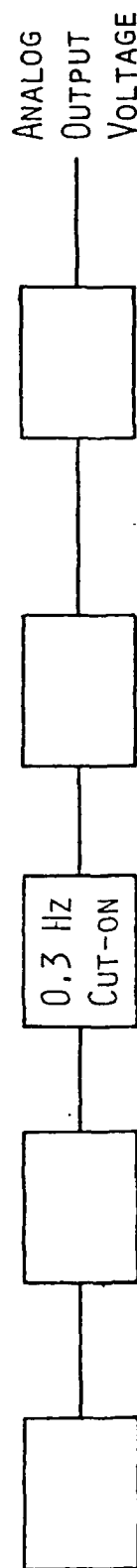


INSB PV
DETECTOR

DC COUPLED
AMPLIFIERS

DC RESTORATION
(COLD REF. CLAMP)

LONGWAVE ANALOG ELECTRONICS DIAGRAM



HgCdTe PC
DETECTOR &
BIAS CIRCUIT

IMPEDANCE
MATCHING
CIRCUIT

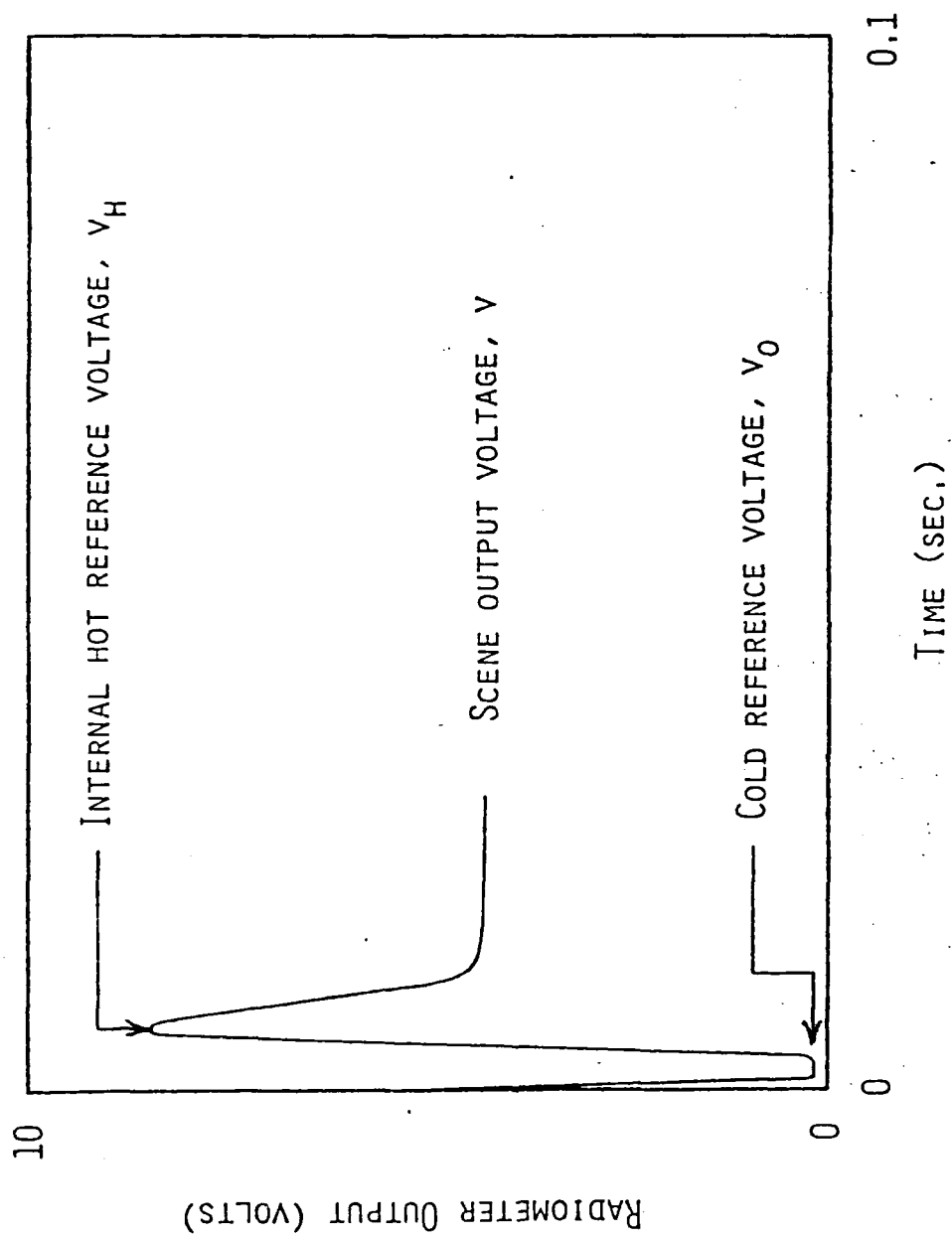
HIGHPASS
ACTIVE
FILTER

DC COUPLED
AMPLIFIERS

DC RESTORATION
(COLD REF, CLAMP)

ANALOG
OUTPUT
VOLTAGE

ANALOG OUTPUT FORMAT



TYPES OF CALIBRATION PERFORMED

POINT SOURCE

(POINT RESPONSE, CROSS-CHANNEL COUPLING, NEI)

BAR SOURCE

(LONGWAVE RESISTIVE COUPLING CORRECTION)

NEAR EXTENDED SOURCE

(RADIOMETRIC RESPONSE)

AD-A154 793 CALIBRATION AND USE OF CLUTTER DATA FOR SIMULATION(U) 3/3
WESTERN KENTUCKY UNIV BOWLING GREEN M S LONGMIRE 1985
N00014-84-C-2034

CALIBRATION AND USE OF CLUTTER DATA FOR SIMULATION(U)
WESTERN KENTUCKY UNIV BOWLING GREEN M S LONGHIRE 1985
N00014-84-C-2034

3/3

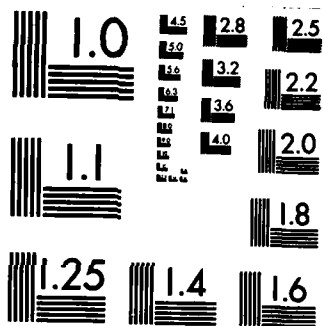
UNCLASSIFIED F/G 17/5 NL

F/G 17/5

NL

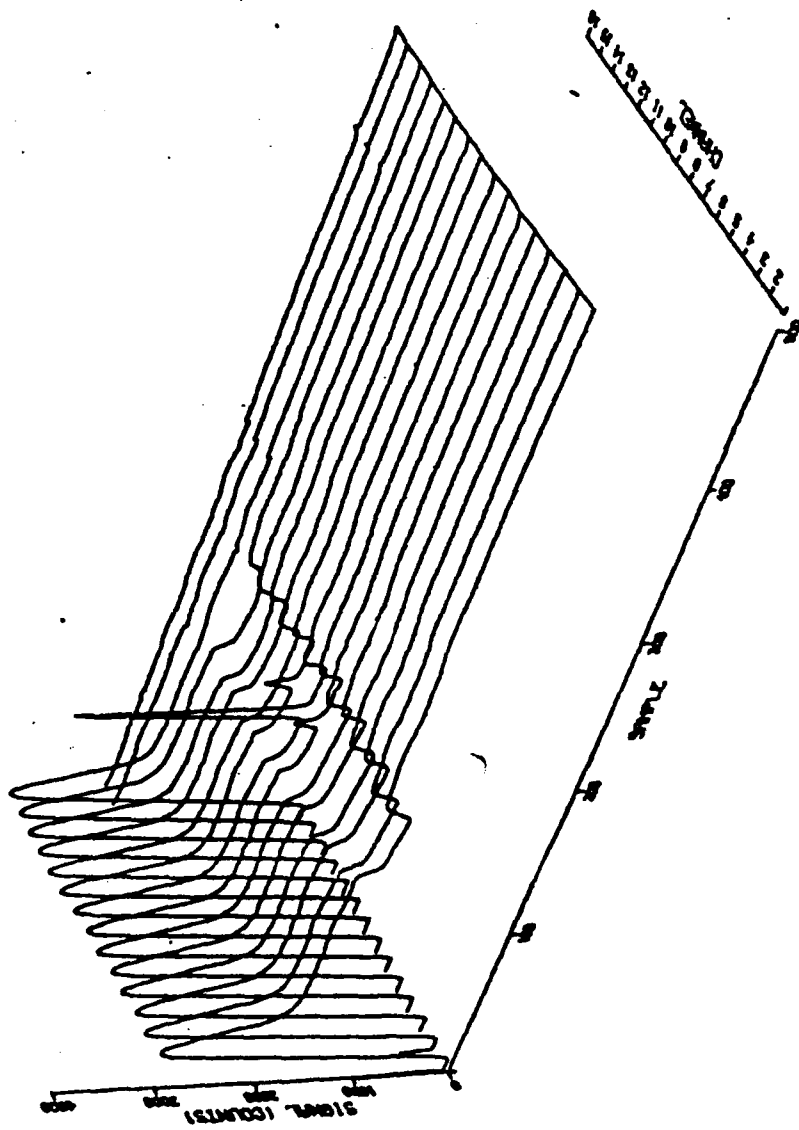
END

FILMED



MICROCOPY RESOLUTION TEST CHART
NATIONAL BUREAU OF STANDARDS-1963-A

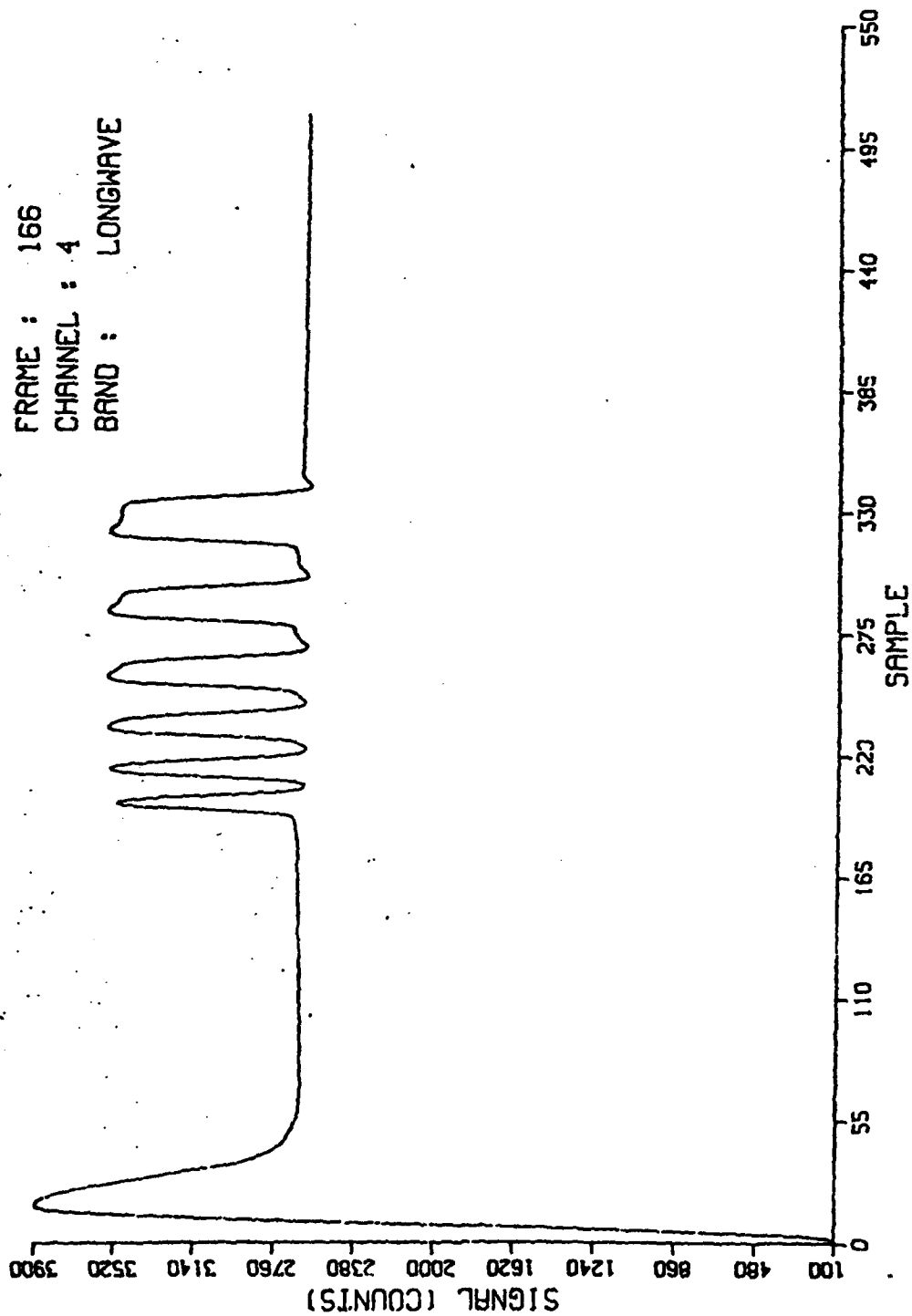
BEDFORD MA., 12 SEPT 1984
TAPE : BF4, MODE : MW , FRAME : 4
2 DAYS, 10 HOURS, 31 MIN, 35.3 SEC



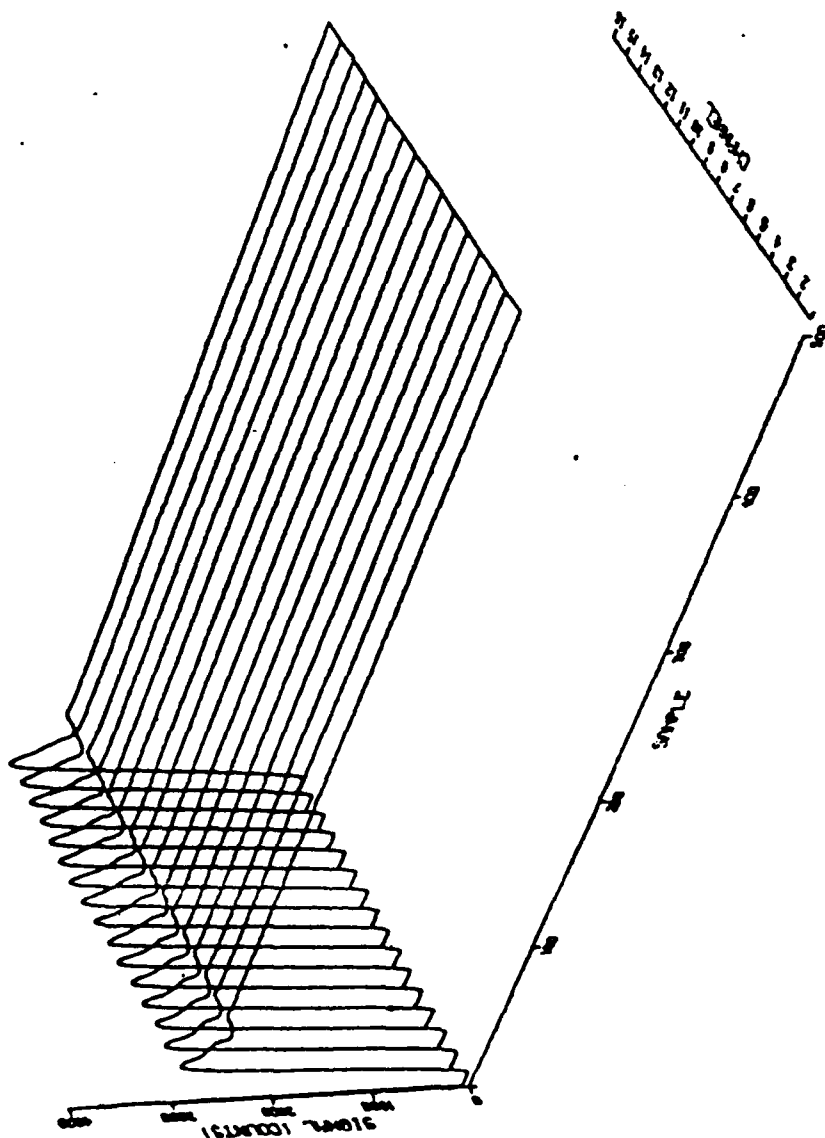
RADIOMETER I - 20.6C, BAR I - 50.0C, RAW DATA

3 DAYS 12 HRS 6 MIN 54.8 SEC

FRAME : 166
CHANNEL : 4
BAND : LONGWAVE

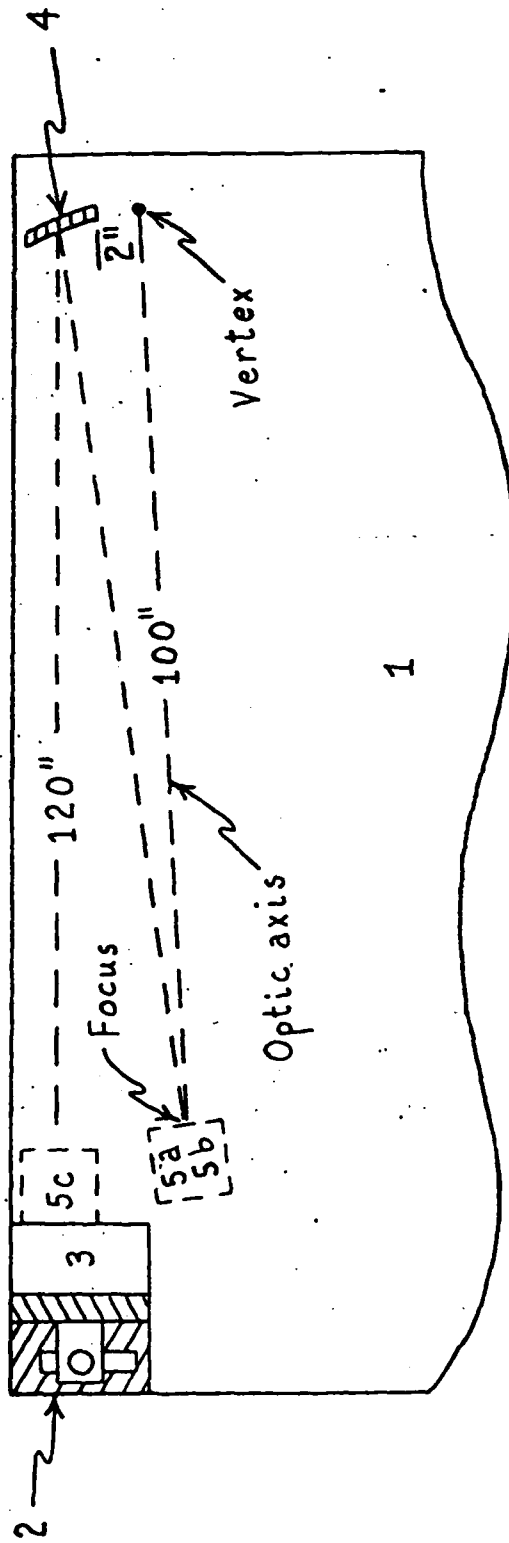


BEDFORD MA., 13 SEPT 1984
TAPE : BF7, MODE : MW , FRAME : 468
3 DAYS, 9 HOURS, 25 MIN, 35.8 SEC



LABORATORY CALIBRATION SET-UP

Top View (not to scale)



1. Optical bench
2. Movable stage, horizontal & vertical micrometer adjustments
3. Radiometer
4. Off-axis paraboloid, 10" dia., 100" f.l.
5. Blackbody source
 - a. EOI model HS 153, 4.7 mil aperture
 - b. EOI model P1406 S1 with 6 bar target
 - c. EOI model P1406 S1 w/o 6 bar target

LABORATORY CALIBRATION PROCEDURE

1. POINT SOURCE SCANS

- A. CENTER POINT-SOURCE IMAGE VERTICALLY ON PIXEL.
- B. RECORD 4 FRAMES.
- C. DO A-B FOR ALL CHANNELS OF DETECTOR ARRAY.
- D. DO A-C FOR BOTH ARRAYS.

2. BAR SOURCE SCANS

- A. CENTER BAR TARGET VERTICALLY ON DETECTOR ARRAY.
- B. RECORD 4 FRAMES IN ALTERNATING MODE (2 FRAMES FROM EACH DETECTOR).
- C. DO A-B WITH BARS AT 10, 20, 30, 40, 50 °C.

3. NEAR EXTENDED SOURCE SCANS

- A. REMOVE BAR APERTURES FROM SOURCE.
- B. PLACE SOURCE CLOSE TO TELESCOPE OBJECTIVE LENS.
- C. RECORD 4 FRAMES.
- D. DO C WITH SOURCE AT 10, 20, 30, 40, 50 °C.

4. DO 1-4 WITH RADIOMETER AT 20, 25, 30, 35, 40 °C.

FIELD CALIBRATION PROCEDURE

1. POINT SOURCE SCANS
 - A. CENTER IMAGE FROM PORTABLE COLLIMATOR VERTICALLY ON PIXEL.
 - B. RECORD 4 FRAMES.
 - C. DO A-B FOR CHANNELS 2, 8, 15 OF DETECTOR ARRAY.
 - D. DO A-C FOR BOTH ARRAYS.
2. NO BAR SOURCE SCANS.
3. NEAR EXTENDED SOURCE SCANS
 - A. SAME PROCEDURE AS IN LABORATORY.
 - B. RECORD SCANS AT END OF EACH DATA TAPE.

CALIBRATION

RESULTS AND DISCUSSION

BAR RESPONSE (LONGWAVE RESISTIVE COUPLING CORRECTION)

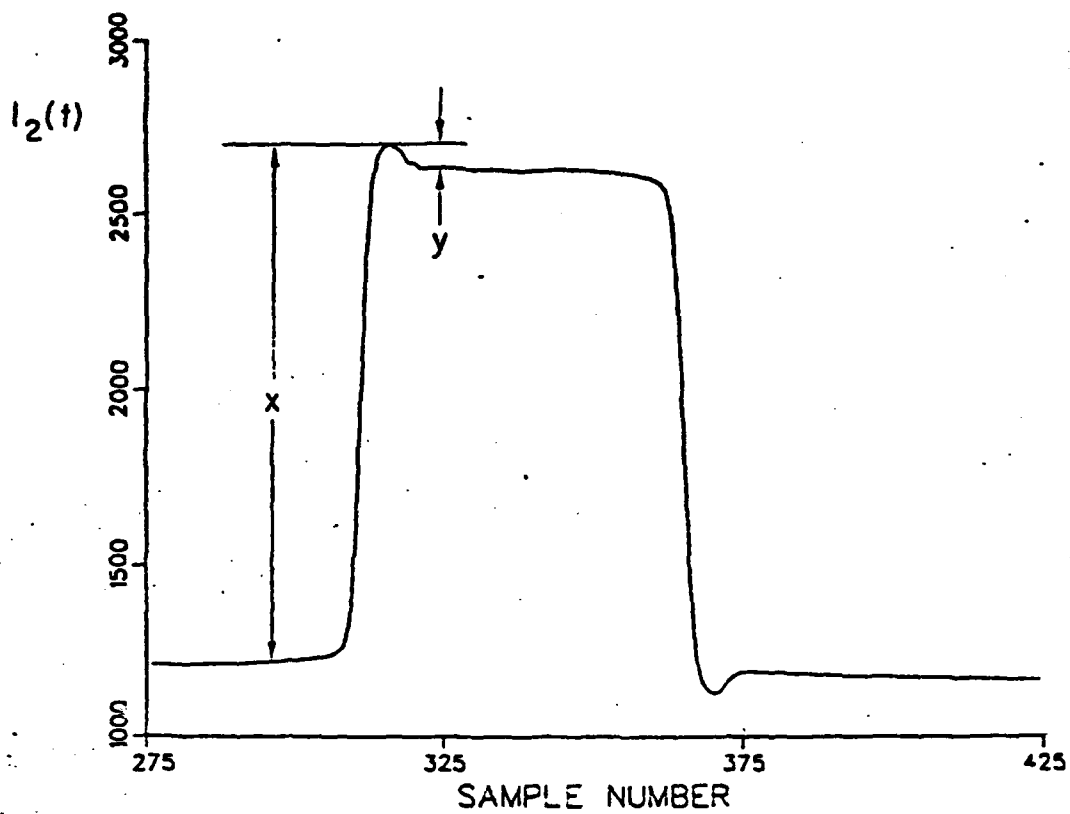


Figure 4 — Postamplifier output waveform for LWIR channel 2

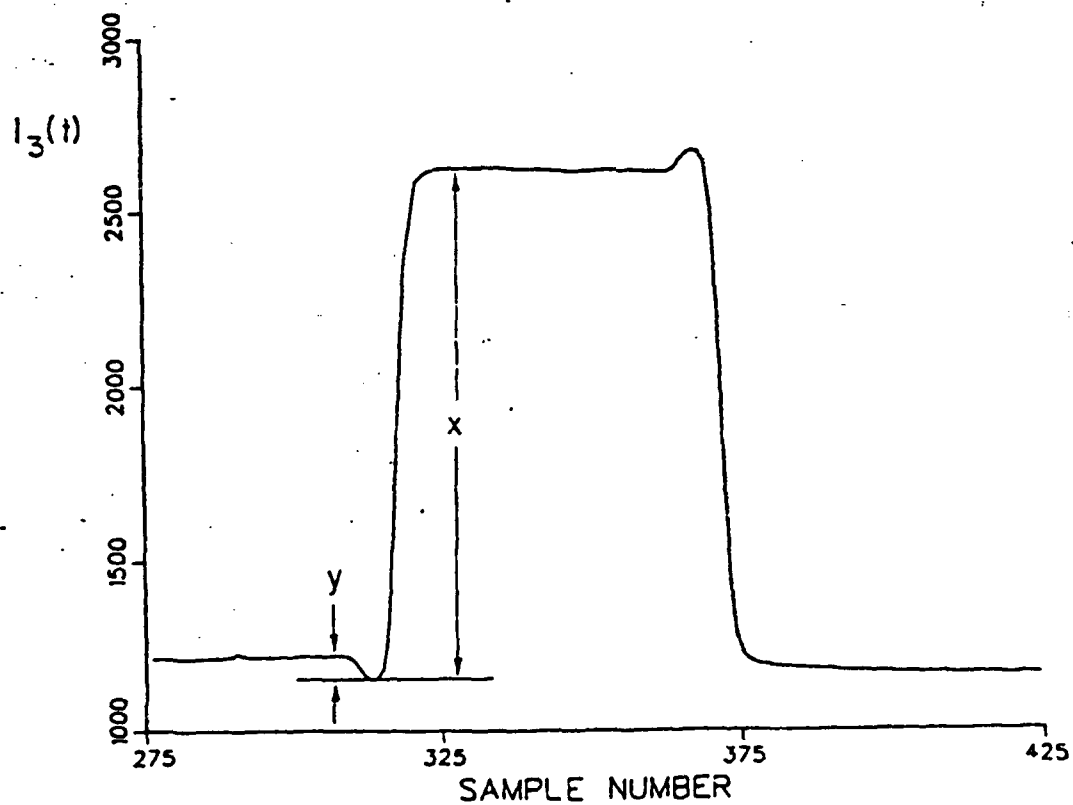
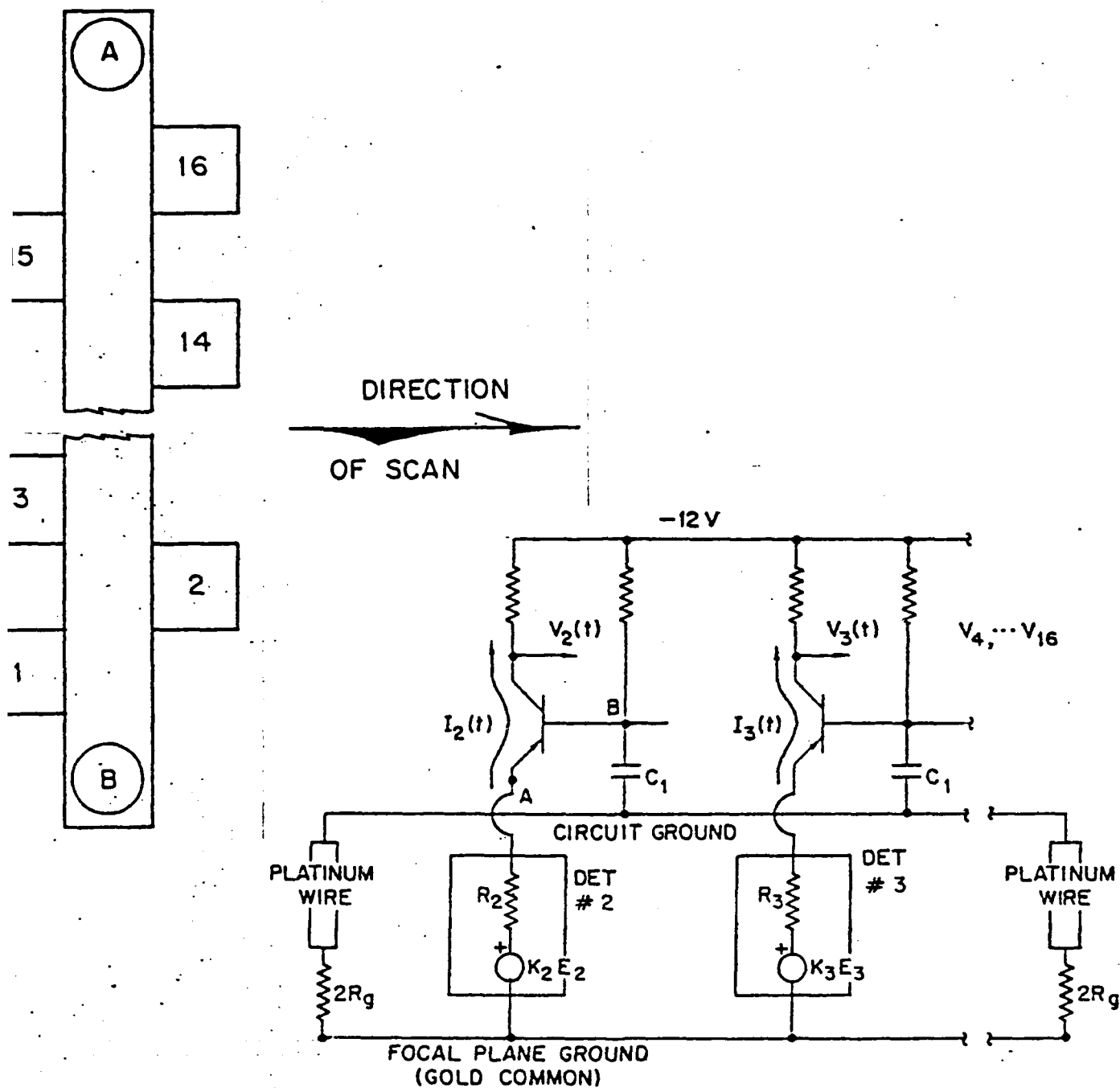


Figure 5 — Postamplifier output waveform for LWIR channel 3



$$E_n(t) = A_n^{-1} \left[I_n(t) + B_n \sum_{m=2}^{16} I_m(t) \right], \quad n = 2, 3, \dots, 16,$$

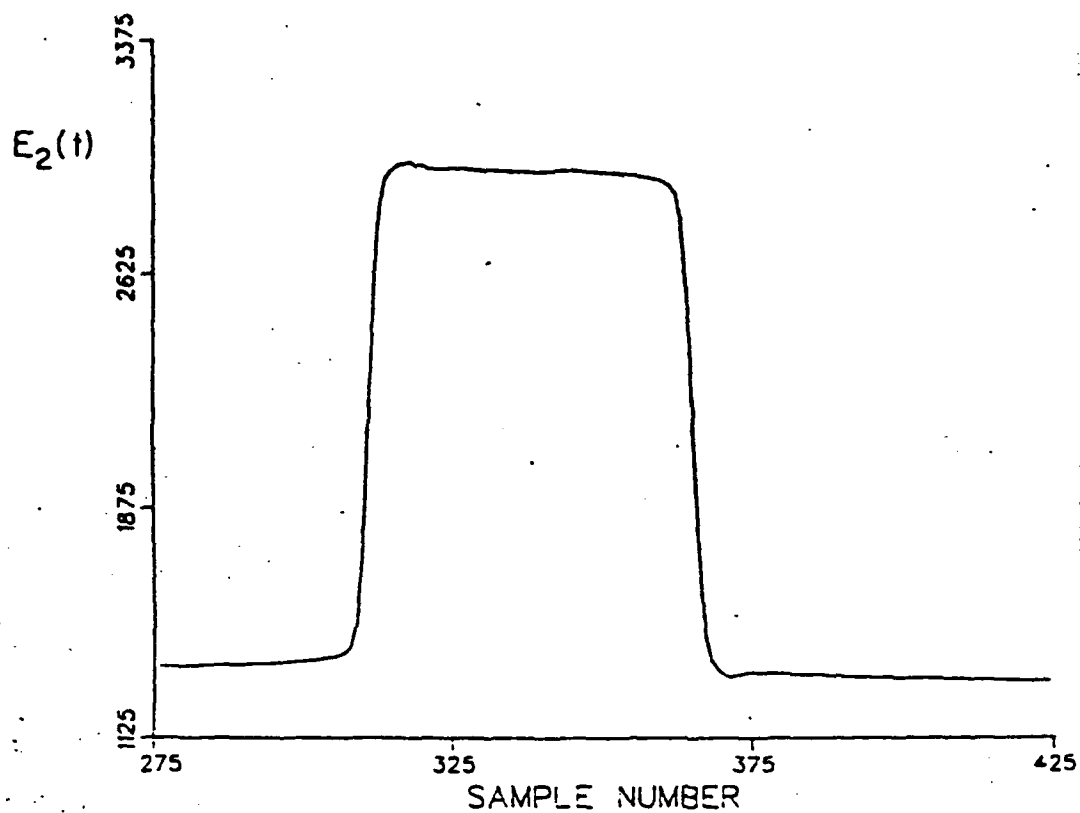


Figure 7 — Channel 2 of corrected data

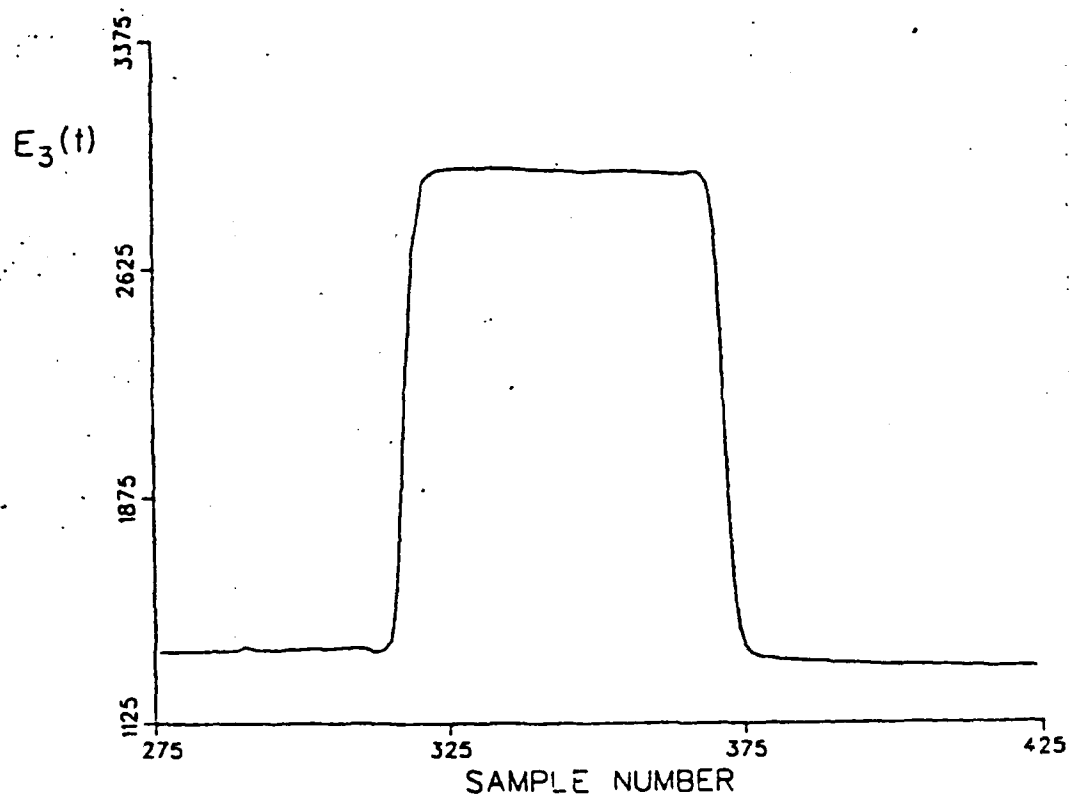


Figure 8 — Channel 3 of corrected data

CALIBRATION

RESULTS AND DISCUSSION

RADIOMETRIC RESPONSE

RADIOMETRIC CALIBRATION

WHAT IS IT?

HOW CAN YOU GET IT?

ANSWERS DEPEND ON

INSTRUMENT

SCENE

FIELD CONDITIONS

DATA USAGE

LUNG WAVE UNIDENTIFICATION
TAPE BF7

CHANNEL 6

STATISTICS FOR $\langle \text{GTL} \rangle = A + Bu$

$A = -12.8$ $B = 55.8$

STANDARD ERROR OF ESTIMATE = 0.062

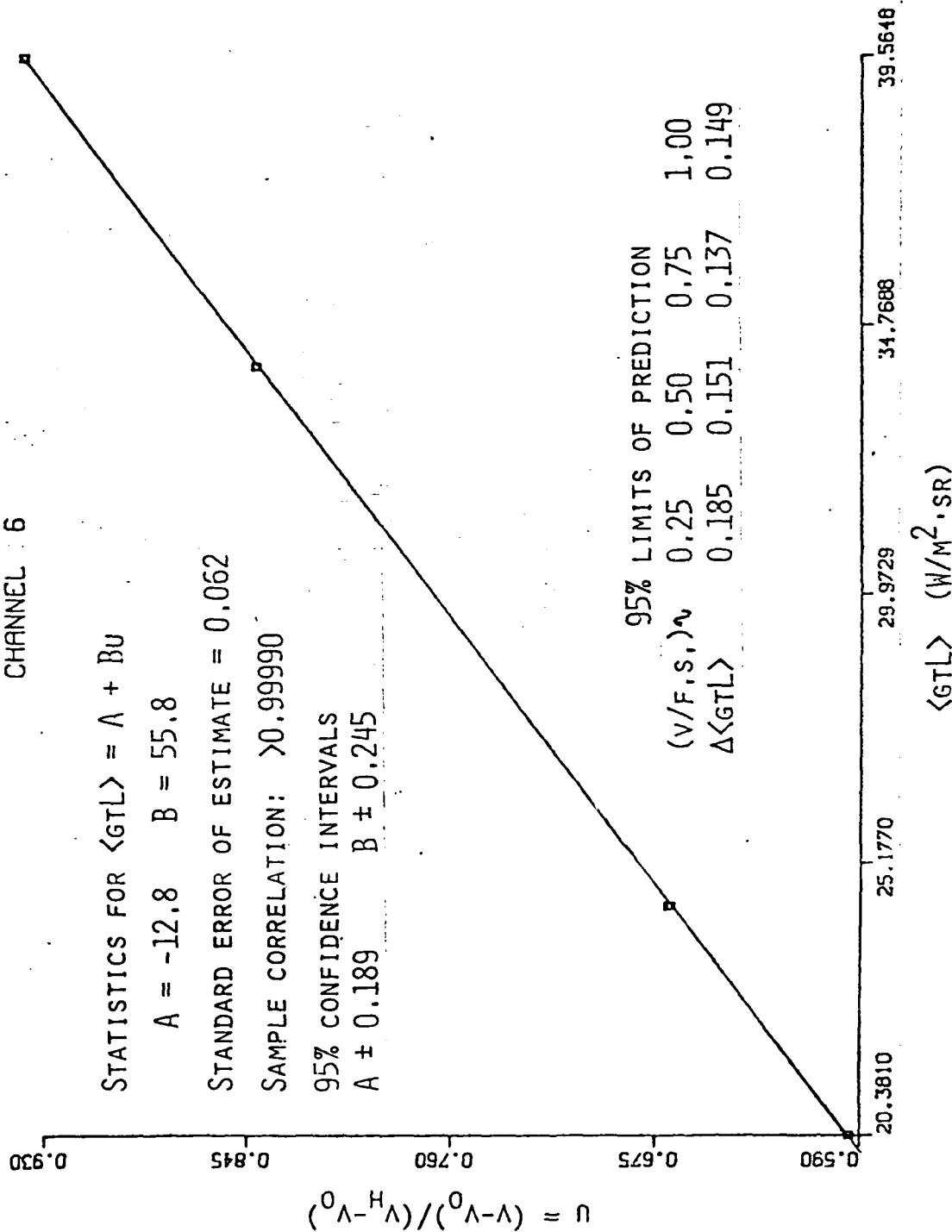
SAMPLE CORRELATION: >0.99990

95% CONFIDENCE INTERVALS

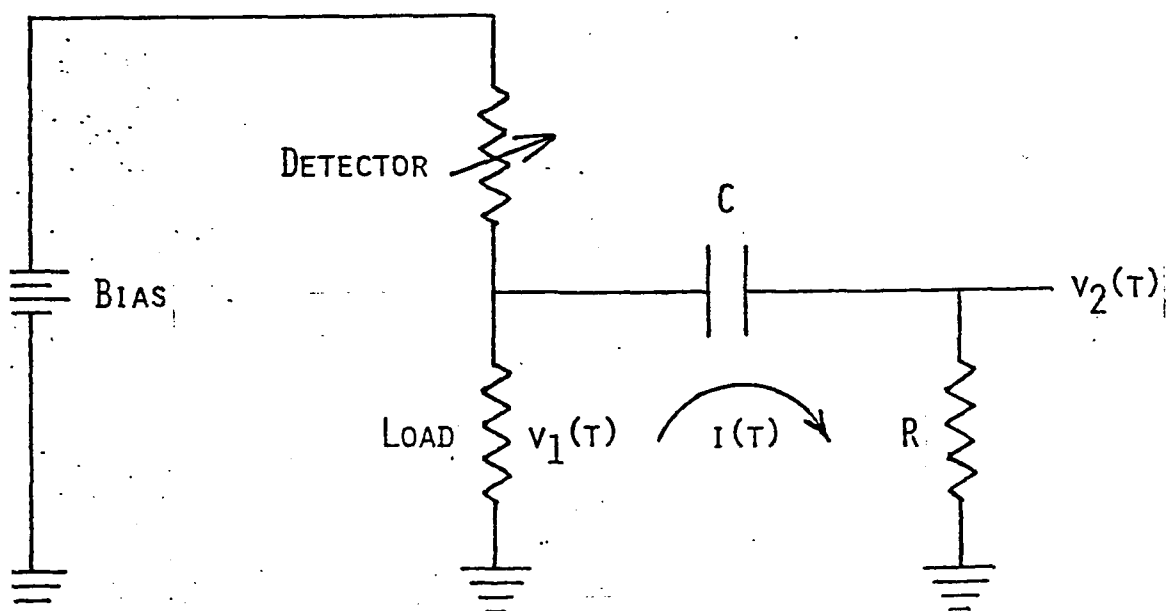
$A \pm 0.189$ $B \pm 0.245$

95% LIMITS OF PREDICTION

$(v/f.s.)^2$	0.25	0.50	0.75	1.00
$\Delta \langle \text{GTL} \rangle$	0.185	0.151	0.137	0.149



BIASED PC DETECTOR & COUPLING CIRCUIT (SIMPLEST CASE)



$$v_1 = v_2 + v_0 + \frac{1}{RC} \int_0^T v_2 \cdot d\tau$$

LONGWAVE RADIOMETER RESPONSE

AC vs. DC COUPLING MAKES LW AND MW RESPONSES DIFFERENT.

ANALYSIS OF LW RESPONSE IS NOT YET COMPLETE.

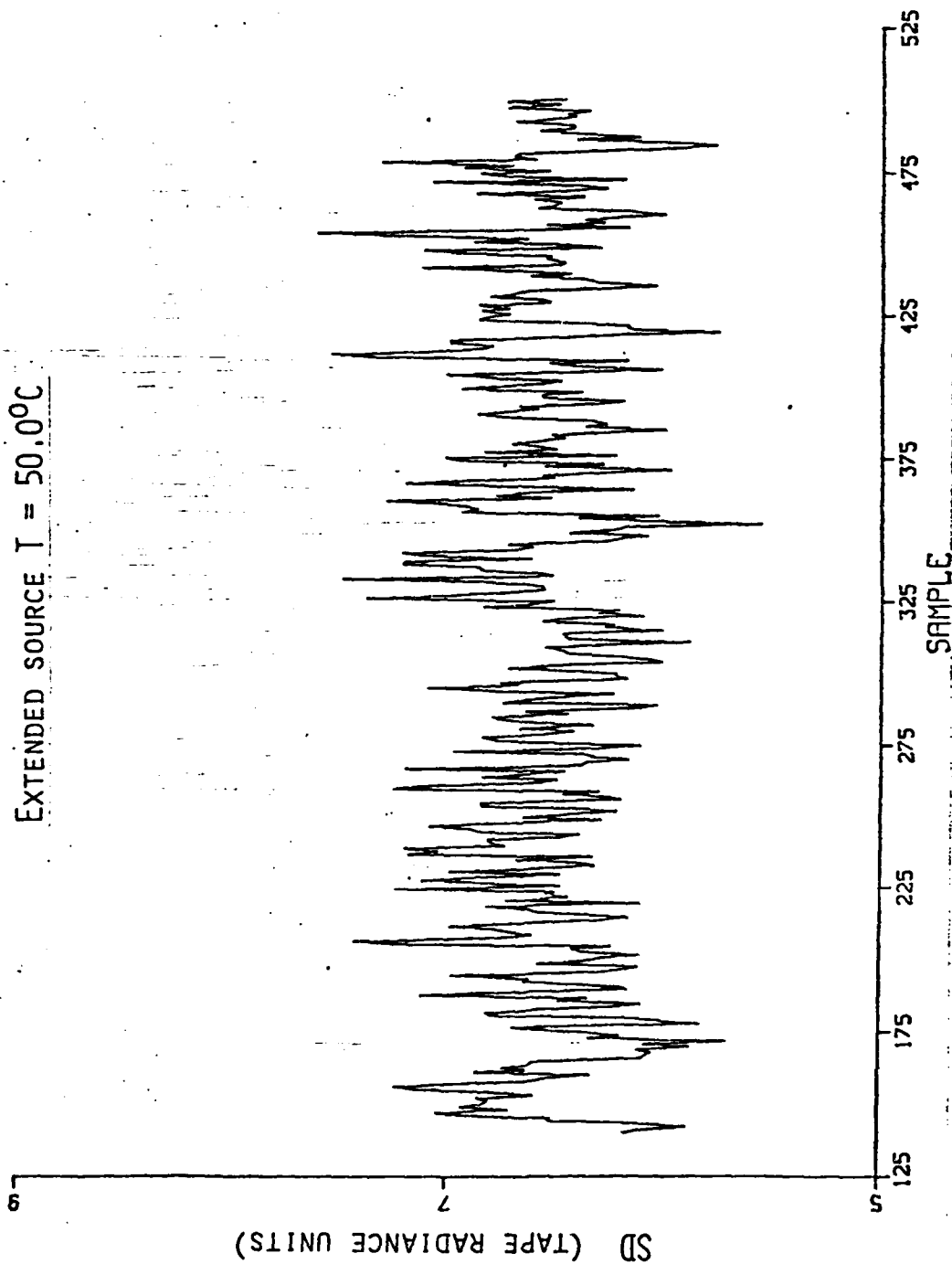
TWO APPROACHES ARE POSSIBLE.

DERIVE LW RESPONSE FUNCTION.

CORRECT LW RESPONSE FOR AC COUPLING, THEN USE MW RESPONSE EQUATION.

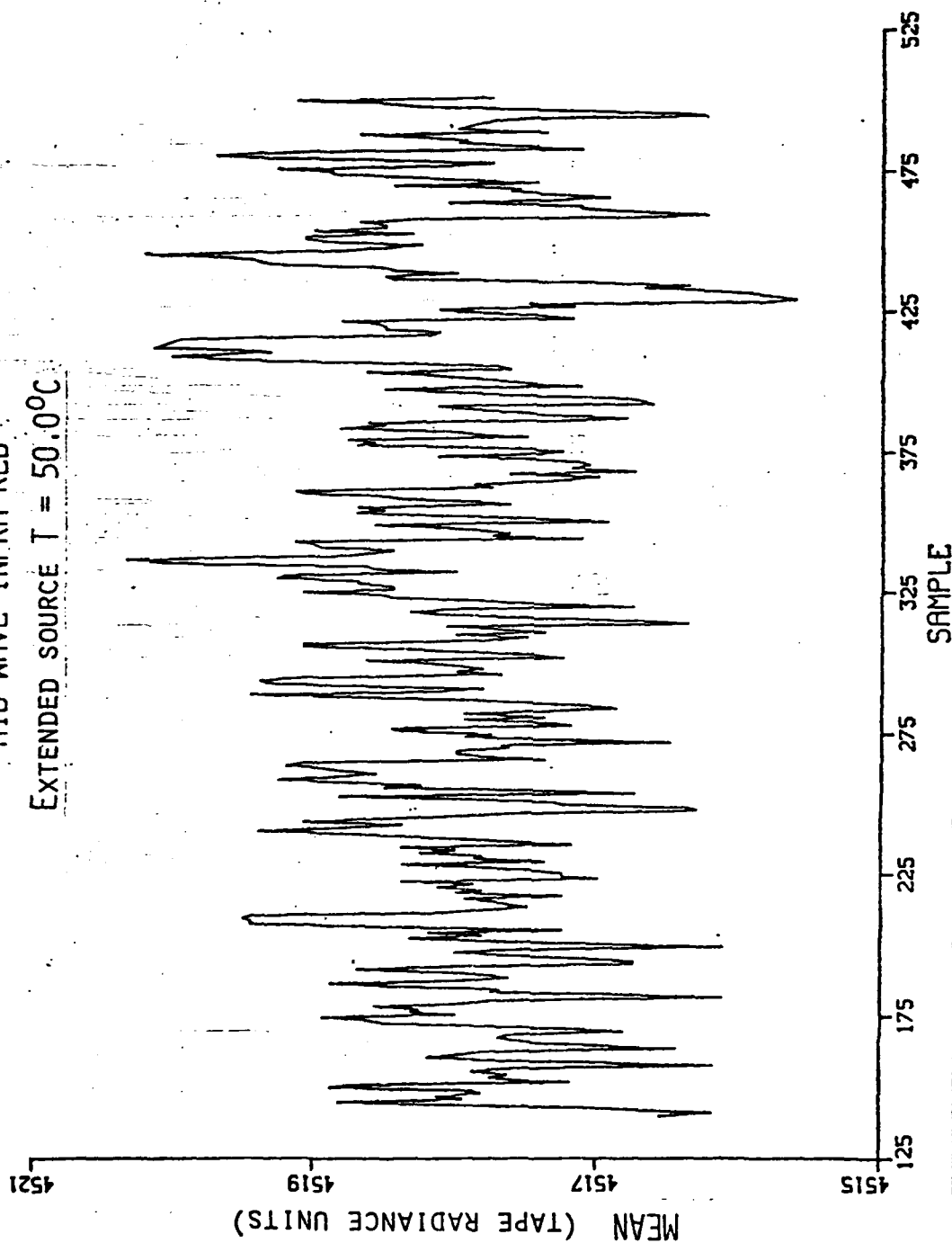
3 DAYS 9 HOURS 24 MINUTES 42.3 SECONDS
MID WAVE INFRA RED

EXTENDED SOURCE $T = 50.0^{\circ}\text{C}$

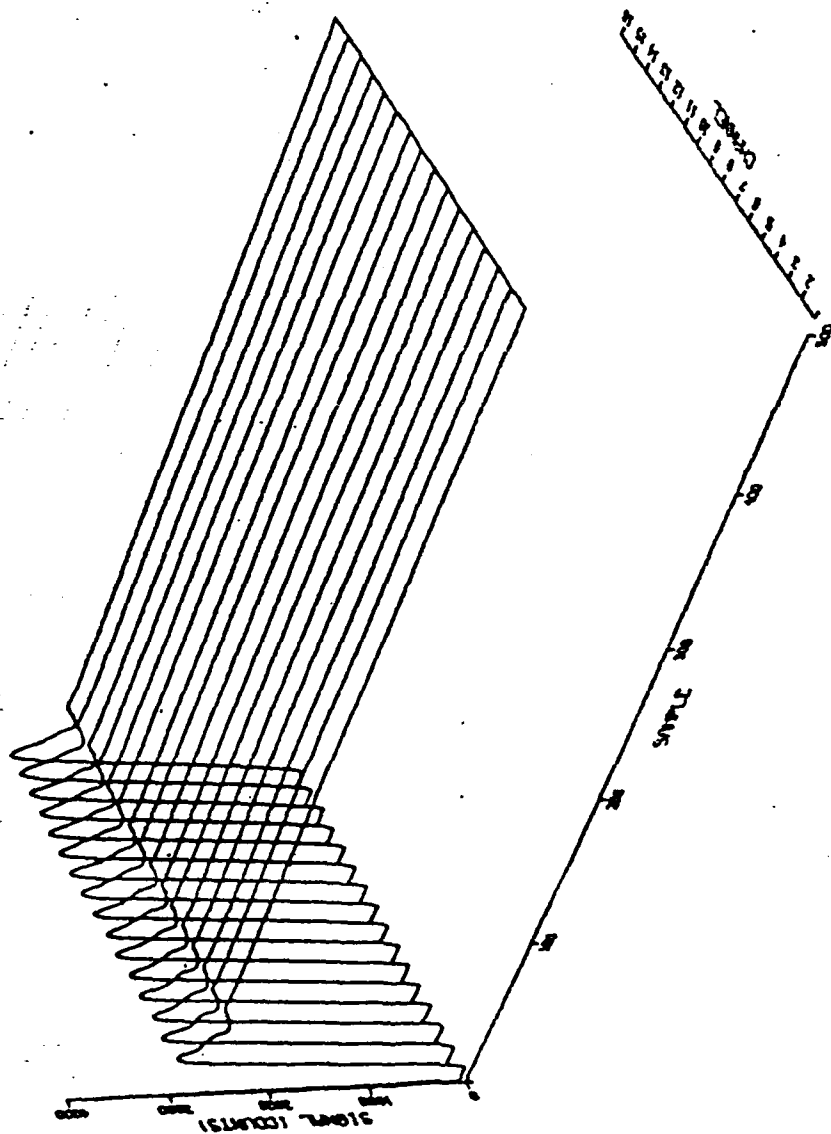


3 DAYS 9 HOURS 24 MINUTES 42.3 SECONDS
MID WAVE INFRARED

EXTENDED SOURCE T = 50.0°C



BEDFORD MA., 13 SEPT 1984
 TAPE : BF7, MODE : MW , FRAME : 468
 3 DAYS, 9 HOURS, 25 MIN, 35.8 SEC



CALIBRATION STATISTICS FOR MID WAVE IR DATA

CHANNEL	COEFFICIENTS		VARIANCE	CONFIDENCE	
	A	B		A	B
1	-0.195	2.23	3.591E-06	2.319E-03	2.927E-03
2	-0.201	2.27	3.812E-06	2.397E-03	3.060E-03
3	-0.232	2.30	5.194E-06	2.843E-03	3.620E-03
4	-0.231	2.32	3.720E-06	2.405E-03	3.095E-03
5	-0.258	2.35	3.237E-06	2.275E-03	2.920E-03
6	-0.251	2.36	7.109E-06	3.359E-03	4.361E-03
7	-0.268	2.38	1.205E-06	1.394E-03	1.805E-03
8	-0.256	2.38	4.916E-06	2.800E-03	3.651E-03
9	-0.276	2.41	5.141E-07	9.148E-04	1.197E-03
10	-0.267	2.43	5.771E-06	3.051E-03	4.037E-03
11	-0.273	2.42	5.943E-06	3.105E-03	4.081E-03
12	-0.250	2.39	4.965E-06	2.805E-03	3.688E-03
13	-0.263	2.40	4.407E-06	2.661E-03	3.487E-03
14	-0.244	2.39	4.624E-06	2.699E-03	3.557E-03
15	-0.251	2.39	4.152E-06	2.567E-03	3.367E-03
16	-0.227	2.37	5.707E-06	2.972E-03	3.920E-03

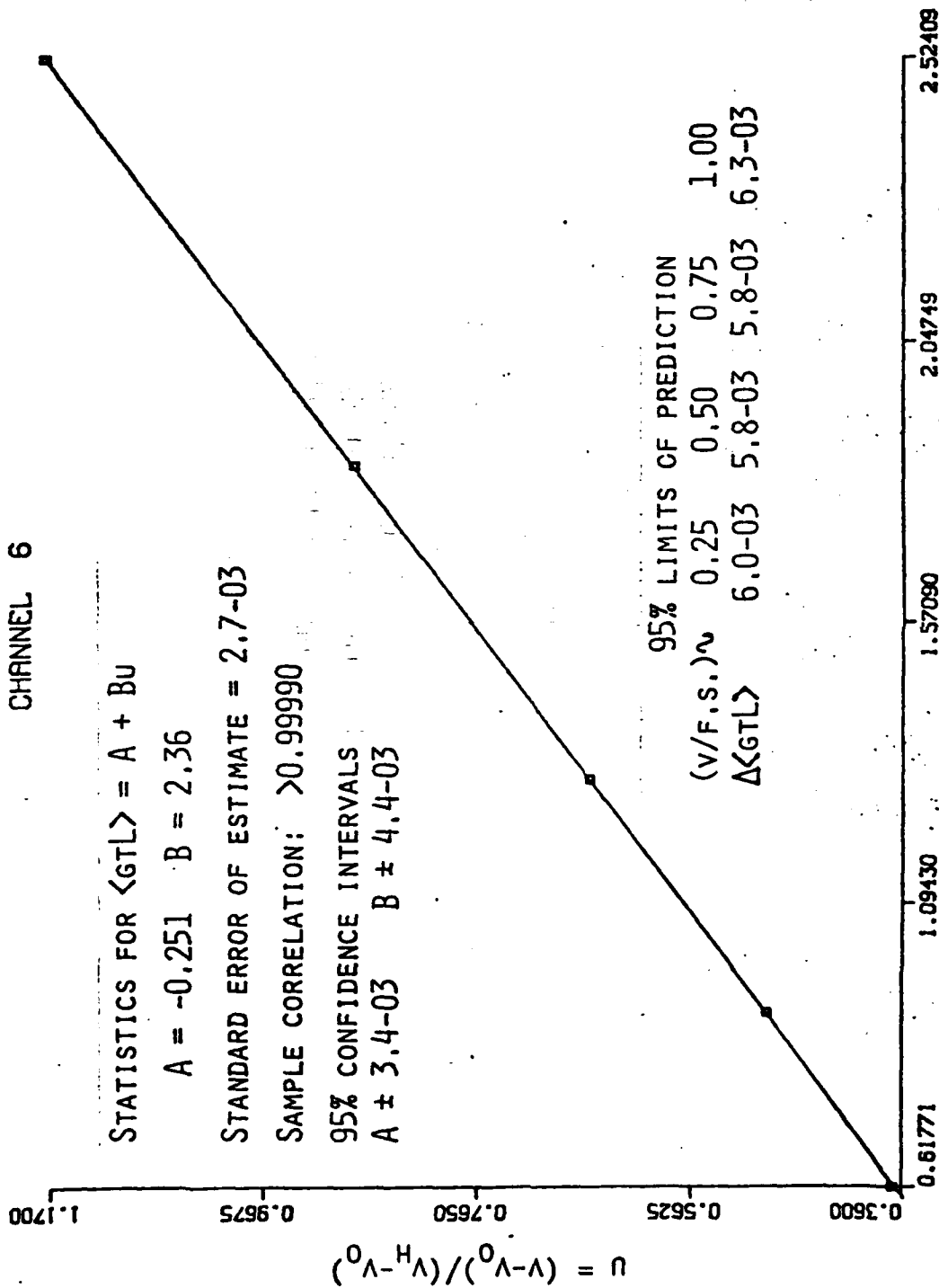
PREDICTION LIMITS FOR MID WAVE IR DATA

CHANNEL	U			
	0.300	0.630	0.960	1.30
1	4.271E-03	4.091E-03	4.134E-03	4.406E-03
2	4.399E-03	4.213E-03	4.265E-03	4.559E-03
3	5.145E-03	4.919E-03	4.978E-03	5.326E-03
4	4.351E-03	4.161E-03	4.218E-03	4.524E-03
5	4.066E-03	3.883E-03	3.934E-03	4.223E-03
6	6.019E-03	5.752E-03	5.839E-03	6.282E-03
7	2.480E-03	2.368E-03	2.403E-03	2.586E-03
8	5.004E-03	4.783E-03	4.859E-03	5.234E-03
9	1.620E-03	1.547E-03	1.572E-03	1.697E-03
10	5.421E-03	5.180E-03	5.275E-03	5.707E-03
11	5.505E-03	5.258E-03	5.349E-03	5.779E-03
12	5.025E-03	4.805E-03	4.888E-03	5.274E-03
13	4.739E-03	4.528E-03	4.604E-03	4.968E-03
14	4.847E-03	4.637E-03	4.718E-03	5.092E-03
15	4.596E-03	4.395E-03	4.469E-03	4.820E-03
16	5.379E-03	5.151E-03	5.241E-03	5.652E-03

CORRELATION: 1.00

MID WAVE CALIBRATION
TAPE BF7

CHANNEL 6



MIDWAVE RADIOMETER RESPONSE

MONOCHROMATIC

$$u = (v - v_0) / (v_H - v_0)$$

$$L = [(L_H - L_0) / T] u - [(L - L_0) / T]$$

BROADBAND

$$\begin{aligned} \langle GTL \rangle &= \langle G(L_H - L_0) \rangle u - \langle G(L - L_0) \rangle \\ &= Bu + A \end{aligned}$$

WHERE

$$\langle Z \rangle = \int Z \cdot d\lambda$$

GT = RADIOMETER'S PEAK NORMALIZED SPECTRAL RESPONSE

BLACKBODY CALIBRATION IS WHAT CIRCUMSTANCES PERMIT.

HOW SHOULD IT BE DONE?

THIRD BEST (BLACKBODY) CALIBRATION*

RELATION BETWEEN RADIOMETER OUTPUT AND
BLACKBODY RADIANCE AT RADIOMETER'S ENTRANCE APERTURE

REQUIRES ONLY

- BLACKBODY STANDARD SOURCE
 - DETERMINATION OF SOURCE RADIANCE AT ENTRANCE APERTURE
 - RADIOMETER'S PEAK NORMALIZED SPECTRAL RESPONSE
-

POSSIBLE, CALIBRATION EQUATION GIVES
PEAK NORMALIZED BLACKBODY RADIANCE
WHICH PRODUCES SAME RESPONSE AS PEAK NORMALIZED SCENE RADIANCE
WITH BOTH RADIANCES MEASURED AT ENTRANCE APERTURE.

*FOR DETAILS SEE
C. L. WYATT, RADIOMETRIC CALIBRATION (ACADEMIC, NY, 1978), ch. 12.

SECOND BEST CALIBRATION

RELATION BETWEEN RADIOMETER OUTPUT AND SCENE RADIANCE
AT RADIOMETER'S ENTRANCE APERTURE

REQUIRES STANDARD SOURCE WITH
SPECTRUM AND RADIANCE RANGE
OF SCENE RADIATION AT ENTRANCE APERTURE

IMPOSSIBLE. SCENE RADIATION AT ENTRANCE APERTURE VARIES WITH
SOLAR ILLUMINATION
METEOROLOGIC CONDITIONS
DISTANCE TO SCENE OBJECTS

BEST CALIBRATION

RELATION BETWEEN RADIOMETER OUTPUT AND SCENE RADIANCE

REQUIRES STANDARD SOURCE
WITH SAME SPECTRUM AS SCENE
RADIANCE RANGE \geq THAT OF SCENE
PLACED BESIDE SCENE

IMPOSSIBLE, SCENES CONTAIN CLOUDS
WITH VARIABLE SPECTRA
VARIABLE RADIANCES
AT DIFFERENT DISTANCES FROM RADIOMETER

DATA USAGE

COMPARISON AND EVALUATION OF IRST DESIGNS
BY SIMULATION OF PERFORMANCE

RADIANCE CALIBRATION MOST VERSATILE FOR THIS USE

CALIBRATION STATISTICS FOR LONG WAVE IR DATA

CHANNEL	COEFFICIENTS		VARIANCE	CONFIDENCE	
	A	B		A	B
2	-12.9	56.2	5.109E-03	0.218	0.284
3	-12.7	56.1	5.241E-03	0.220	0.287
4	-12.7	55.9	4.030E-03	0.193	0.251
5	-12.8	56.2	3.848E-03	0.189	0.246
6	-12.8	55.8	3.849E-03	0.189	0.245
7	-12.5	55.6	4.435E-03	0.201	0.262
8	-12.6	55.4	4.327E-03	0.199	0.257
9	-12.8	55.5	5.699E-03	0.230	0.296
10	-13.0	55.4	4.379E-03	0.202	0.259
11	-12.8	55.0	4.178E-03	0.197	0.251
12	-12.8	54.5	3.277E-03	0.174	0.220
13	-13.3	54.8	5.668E-03	0.232	0.291
14	-13.2	54.0	3.852E-03	0.191	0.237
15	-14.1	54.8	5.705E-03	0.237	0.292
16	-13.7	53.9	4.439E-03	0.207	0.254

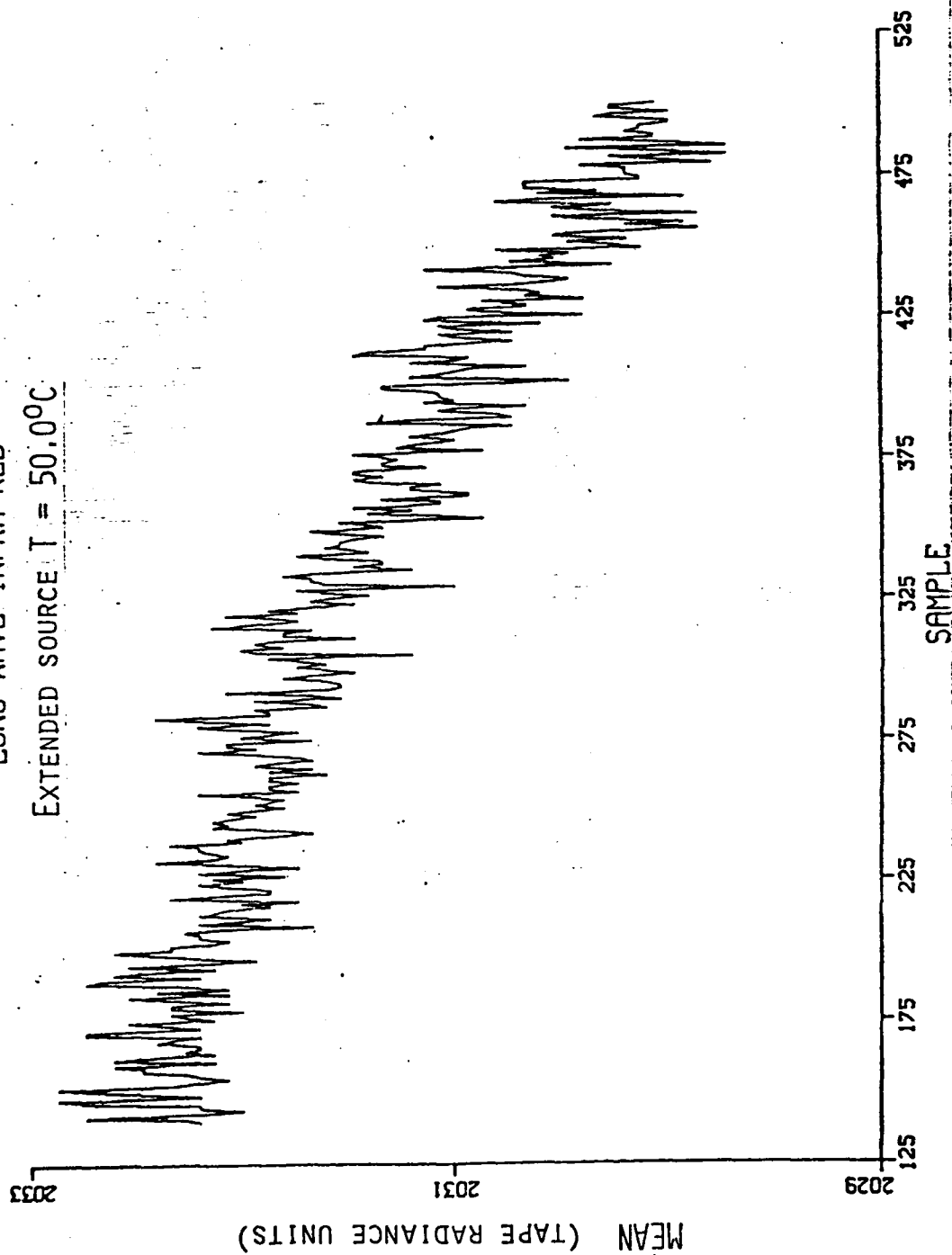
PREDICTION LIMITS FOR LONG WAVE IR DATA

CHANNEL	U			
	0.250	0.500	0.750	1.00
2	0.213	0.174	0.158	0.173
3	0.216	0.176	0.160	0.175
4	0.189	0.154	0.140	0.153
5	0.185	0.151	0.137	0.150
6	0.185	0.151	0.137	0.149
7	0.198	0.162	0.147	0.160
8	0.196	0.160	0.145	0.158
9	0.226	0.184	0.167	0.181
10	0.199	0.162	0.146	0.158
11	0.194	0.158	0.143	0.154
12	0.172	0.141	0.127	0.136
13	0.228	0.186	0.167	0.178
14	0.188	0.154	0.138	0.146
15	0.231	0.188	0.168	0.177
16	0.204	0.166	0.148	0.155

CORRELATION: 1.00

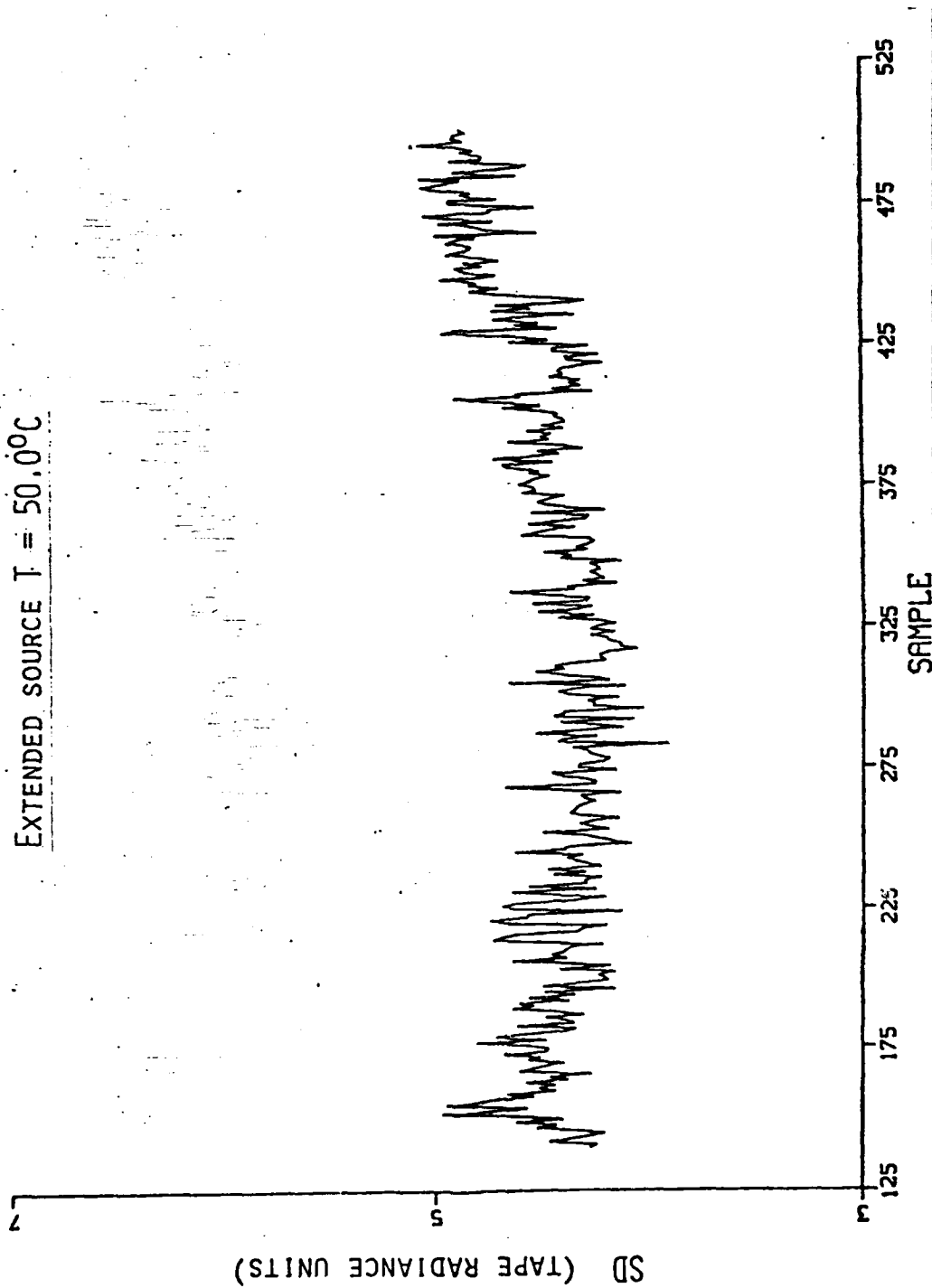
3 DAYS 9 HOURS 29 MINUTES 31.8 SECONDS
LONG WAVE INFRA RED

EXTENDED SOURCE T = 50.0°C



3 DAYS 9 HOURS 29 MINUTES 31.8 SECONDS
LONG WAVE INFRA RED

EXTENDED SOURCE T = 50.0°C



END

END

FILMED

7-85

DTIC